

Geometry of the cumulant series in diffusion MRI

Santiago Coelho,¹ Jenny Chen,¹ Filip Szczepankiewicz,² Els Fieremans,¹ and Dmitry S. Novikov¹

¹Center for Biomedical Imaging and Center for Advanced Imaging Innovation and Research (CAI²R),

Department of Radiology, New York University School of Medicine, New York, USA

²Department of Medical Radiation Physics, Lund University, Lund, Sweden

Water diffusion gives rise to micron-scale sensitivity of diffusion MRI (dMRI) to cellular-level tissue structure. Precision medicine and quantitative imaging depend on uncovering the information content of dMRI and establishing its parsimonious hardware-independent fingerprint. Based on the rotational SO(3) symmetry, we study the geometry of the dMRI signal and the topology of its acquisition, identify irreducible components and a full set of invariants for the cumulant tensors, and relate them to tissue properties. Including all kurtosis invariants improves multiple sclerosis classification in a cohort of 1189 subjects. We design the shortest acquisitions based on icosahedral vertices to determine the most used invariants in only 1–2 minutes for whole brain. Representing dMRI via scalar invariant maps with definite symmetries will underpin machine learning classifiers of pathology, development, and aging, while fast protocols will enable translation of advanced dMRI into clinic.

Diffusion NMR or MRI (dMRI) measures a propagator of micrometer-scale displacements of spin-carrying molecules in an NMR sample or in every imaging voxel^{1,2}. Porous media^{1,3} and biological tissues^{4,5} can be noninvasively probed by quantifying diffusion propagator for water molecules. Mapping its lowest-order cumulant, the voxel-wise diffusion tensor D , via diffusion tensor imaging (DTI)⁶, has become an integral part of most human brain MRI clinical protocols and research studies. The information-rich signal beyond DTI forms the foundation of tissue microstructure imaging^{7–13} — a combination of biophysics, condensed matter physics and bioengineering. This allows MRI to become specific to disease processes at the scale of cells and organelles, and to provide non-invasive markers of development, aging and pathology^{14,15}.

The information content of dMRI signal depends on the degree of coarse-graining^{8,10} over the diffusion length controlled by the diffusion time t . For long t , each *compartment* (a well-defined water population, e.g., intra-axonal, extra-cellular, perivascular, etc) can be considered as fully coarse-grained, such that diffusion within it becomes Gaussian^{8,16,17}. This is typically the case in brain dMRI, with $t \gtrsim 50$ ms in human scans. The signal $S = \exp(-\text{tr } BD)$ (normalized to 1 in the absence of diffusion weighting) from any such “Gaussian compartment” defined by its diffusion tensor D , becomes fully encoded by a 3×3 symmetric B-tensor^{3,18–22}. The signal $\langle S \rangle$ from a distribution of Gaussian compartments within a voxel is then represented by the cumulant expansion^{21,23,24}

$$\ln \langle S \rangle = \ln \langle e^{-B_{ij} D_{ij}} \rangle = -B_{ij} D_{ij} + \frac{1}{2} B_{ij} B_{kl} C_{ijkl} + O(b^3), \quad (1)$$

where $b = \text{tr } B$ is the so-called *b-value*², the summation over repeated Cartesian indices is assumed hereon, and

$$\begin{aligned} D_{ij} &= \langle D_{ij} \rangle, \\ C_{ijkl} &= \langle\langle D_{ij} D_{kl} \rangle\rangle \equiv \langle (D_{ij} - \langle D_{ij} \rangle) (D_{kl} - \langle D_{kl} \rangle) \rangle \end{aligned} \quad (2)$$

are the voxel-wise diffusion and covariance tensors. The averages $\langle \dots \rangle$ are taken over the distribution $\mathcal{P}(D)$ of diffusion tensors (Fig. 1a), while $\langle\langle \dots \rangle\rangle$ denote its cumulants²³.

For shorter t , e.g., relevant for human body dMRI, the coarse-graining is incomplete, and diffusion in individual compartments remains non-Gaussian, characterized by time-dependent tensors $D(t)$ and higher-order cumulants, such as

the kurtosis tensor $S(t)$.⁸ The B-tensor then does not fully specify the measurement. Instead, the time-dependent cumulant tensors of the form (2), $D(t) = \langle D(t) \rangle$ and $C(t) = \langle\langle D(t) \otimes D(t) \rangle\rangle$, as well as the overall microscopic kurtosis tensor $S_\mu(t)$, can be accessed^{25,26} with double diffusion encoding (DDE)²⁰. In any case, understanding the nature of tensors of the form (2) has become indispensable for dMRI.

A fundamental problem is to classify symmetries of the cumulant tensors ubiquitous in representing a dMRI signal, and define their *tensor invariants*, i.e., basis-independent combinations of components (such as the trace D_{ii}). With the advent of precision medicine and quantitative imaging²⁷, the invariants form a basis- and hardware-independent fingerprint of MRI signals^{28–39}; their information content will underpin classifiers of pathology, development and aging⁴⁰. A practical problem is to relate tensors and their invariants to tissue properties^{7,9}, and to design fast unbiased measurements.

Here we study the geometry of the dMRI signal by viewing the cumulant tensors via the addition of “angular momenta” coming from the compartment tensors D . We decompose tensors D and C with respectively 6 and 21 degrees of freedom (DOF) according to irreducible representations of the SO(3) group of rotations. We then construct and classify a complete set of $3 + 18$ rotational invariants of the cumulant expansion (1), or RICE, up to $O(b^2)$. The group-theory approach generalizes to the DDE-estimated $D(t)$, $C(t)$, and $S_\mu(t)$, yielding $3 + 18 + 12$ t -dependent invariants, respectively, reveals the cumulant tensors’ symmetries and geometric meaning, relates the topology of dMRI acquisitions to that of SO(3) group manifold, and connects with tissue biophysics embodied in the distribution of compartment tensors. We express all known dMRI contrasts up to $O(b^2)$ — mean diffusivity (MD), fractional anisotropy (FA), mean, radial and axial kurtosis (MK, RK, AK), microscopic FA (μ FA), isotropic/anisotropic variance, etc — via just 7 RICE invariants. Besides uncovering the 14 unexplored invariants of C , and the 12 invariants of $S_\mu(t)$ for non-Gaussian compartments, constructing RICE according to symmetries makes them maximally independent, and thus potentially more specific to tissue microstructure changes.

Our geometric approach applies to hundreds of thousands publicly available human dMRI brain datasets^{41–46}. Using

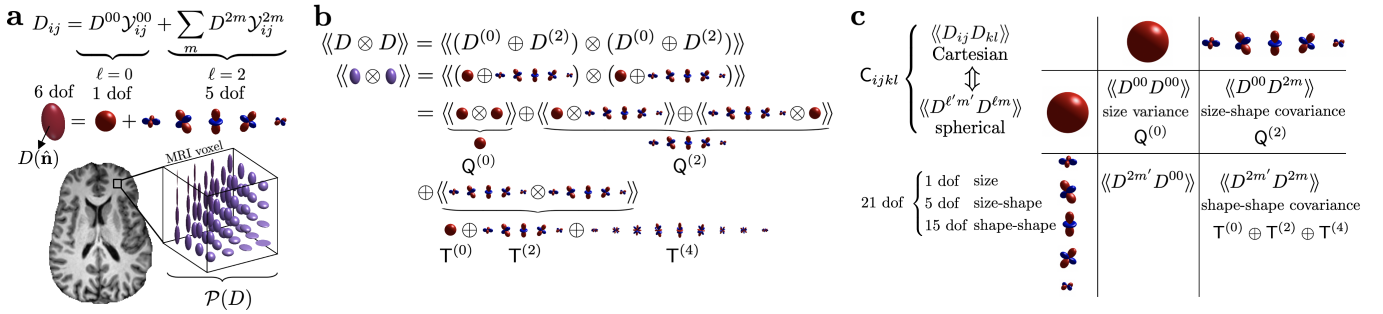


FIG. 1. Outline: (a) An MRI voxel is represented via the distribution $\mathcal{P}(D)$ of compartment diffusion tensors D decomposed in the spherical tensor basis. (b) The QT decomposition of the covariance tensor C arises from the addition of ‘angular momenta’, Eq. (6): Central moments (2) of compartment tensors D correspond to tensor products, subsequently averaged over the voxel-wise distribution $\mathcal{P}(D)$. (c) Irreducible components of the QT decomposition represent 1 size-size, 5 size-shape, and $1 + 5 + 9$ shape-shape covariances in the 21 DOF of C .

clinical dMRI of 1189 patients^{47,48}, we show that the complete set of invariants for the kurtosis tensor outperforms the subset of 6 conventional invariants for classification of multiple sclerosis. We also derive the shortest (“instant”) iRICE protocols for mapping MD, FA, MK in 1 minute, and MD, FA, MK, μ FA in 2 minutes on a clinical scanner, making advanced dMRI clinically feasible. The methodology further applies to higher-order tensors in Eq. (1), as well as to the 4th-order elasticity tensor in materials science and geology^{49–52}.

RESULTS

Our main method of investigation will be theory of the $SO(3)$ group, which we introduce as a warm-up, supply along the way, and systematize in *Methods* and *Supplementary* sections. Our central QT decomposition viewpoint (6)–(8) on C as an addition of ‘angular momenta’ from compartment tensors D applies both for Gaussian and non-Gaussian compartments. For Gaussian compartments, axially symmetric B-tensors yield all C-tensor components and realize the Hopf mapping of the $SO(3)$ group manifold onto conventional spherical shell-based dMRI acquisitions. For non-Gaussian compartments, the B-tensor representation (1) of the cumulant series is inconsistent. The signal depends on the frequency spectrum of the diffusion weighting rather than just its shape B; also, extra $\mathcal{O}(b^2)$ terms arise due to the intrinsic (microscopic) kurtosis $S(t)$ in individual compartments. Estimating these contributions requires a longer DDE acquisition. Therefore, we first develop our formalism assuming Gaussian compartments, Eqs. (1)–(2), where C is the only $\mathcal{O}(b^2)$ contribution, and establish its SA decomposition motivated by the kurtosis imaging. The relations (18) between QT and SA decompositions, their $3 + 18$ invariants, the relation to previous dMRI contrasts, and the fast iRICE protocols, all assume Gaussian compartments. We apply this formalism to the classification of multiple sclerosis from human brain dMRI. Finally, we come back to non-Gaussian compartments, consider the analog (36) of the series (1) for DDE, and in Eq. (38) identify all the irreducible t -dependent components (6)–(8) of $C(t)$, and of the microscopic kurtosis $S_\mu(t)$, Eq. (21), thus fully solving the problem up to $\mathcal{O}(b^2)$.

Warm-up: Irreducible decomposition of the diffusion tensor

To set the stage, recall that a 3×3 symmetric matrix, such as a diffusion tensor D_{ij} , splits into an isotropic component, $D_{ij}^{(0)}$, and a symmetric trace-free (STF) component, $D_{ij}^{(2)}$:

$$D_{ij} = D_{ij}^{(0)} + D_{ij}^{(2)} = D^{00} \mathcal{Y}_{ij}^{00} + \sum_{m=-2}^2 D^{2m} \mathcal{Y}_{ij}^{2m}, \quad (3)$$

where the matrices $\mathcal{Y}^{\ell m}$ form the standard spherical tensor basis, so that $\mathcal{Y}^{\ell m}(\hat{\mathbf{n}}) = \mathcal{Y}_{ij}^{\ell m} n_i n_j$ are the spherical harmonics on a unit sphere $|\hat{\mathbf{n}}| = 1$.⁵³ Here we use the Racah normalization for spherical harmonics (see *Methods*), such that $\mathcal{Y}_{ij}^{00} = \delta_{ij}$ (unit matrix). The $\ell = 0$ component is the mean diffusivity $D^{00} = \frac{1}{3} \text{tr } D$ setting the overall size of the diffusion tensor ellipsoid $D(\hat{\mathbf{n}}) = D_{ij} n_i n_j$, while the five $\ell = 2$ components D^{2m} are responsible for its shape and orientation.

Upon rotations, the spherical tensor components $D^{\ell m}$ with different ℓ do not mix: D^{2m} transform amongst themselves; D^{00} is an invariant. Mathematically, they belong to different irreducible representations of the $SO(3)$ group^{53–55}. Hence, Eq. (3) realizes the *irreducible decomposition*²⁸

$$D = D^{(0)} \oplus D^{(2)}, \quad D^{(\ell)} \equiv \{D^{\ell m}\}, \quad m = -\ell, \dots, \ell, \quad (4)$$

where each irreducible component of degree ℓ has $2\ell + 1$ DOF, such that the 6 DOF of a symmetric 3×3 matrix D splits into $6 = 1 + 5$, cf. Fig. 1a. Spherical tensors will be our workhorse, as they represent high-dimensional objects using the minimal number of DOF. Furthermore, irreducible components with different ℓ point at distinct symmetries and physical origins.

The diffusion tensor in Eq. (3) may describe a microscopic tissue compartment. Consider the invariants of D : the ellipsoid’s shape is defined by 3 semi-axes (the eigenvalues). The remaining 3 DOF define its orientation in space (e.g., 3 Euler’s angles), and depend on the coordinate frame. The irreducible decomposition (4) allows one to construct tensor invariants symmetric with respect to the eigenvalues, and to assign the degree ℓ to them. The simplest, $\ell = 0$ invariant, is the trace $\text{tr } D = 3D^{00}$. The remaining two independent $\ell = 2$ invariants are also given by traces: $\text{tr}(D^{(2)})^2$ is proportional to the

variance of the eigenvalues, and $\text{tr}(D^{(2)})^3 = 3 \det D^{(2)}$ — to their product. The latter relation is readily seen in the eigenbasis, where $D^{(2)} = \text{diag}[\lambda_1, \lambda_2, -(\lambda_1 + \lambda_2)]$. Note we drop parentheses after ‘tr’ for readability, cf. *Methods/Notations*.

The overall diffusion tensor D_{ij} is the mean of the compartment tensors (3) over $\mathcal{P}(D)$, cf. Eq. (2). Invariants of D give rise to common DTI metrics, such as MD from $\ell = 0$,

$$\text{MD} = D_0 \equiv D^{00} = \overline{D(\hat{\mathbf{n}})} = \frac{1}{3} D_{ii}, \quad (5)$$

and FA (from both $\ell = 0$ and $\ell = 2$ sectors, cf. Eq. (27) below). The 00 spherical harmonics component equals the directional average (overbar) by virtue of the Racah normalization avoiding $\sqrt{4\pi}$ factors.

The covariance tensor C involves averages of the direct tensor products $D \otimes D$, Eq. (2). As such, it has a major symmetry (swapping first and second pairs of indices), and a minor symmetry (in each of the index pairs). Below we will formally map C onto the addition of quantum angular momenta with $\ell = 0$ or 2, construct all its irreducible components and invariants.

Size and shape covariances: QT decomposition

Using the irreducible decomposition (4) in Eq. (2) results in

$$\begin{aligned} C &= \langle\langle D \otimes D \rangle\rangle = \langle\langle (D^{(0)} \oplus D^{(2)}) \otimes (D^{(0)} \oplus D^{(2)}) \rangle\rangle \\ &= Q^{(0)} \oplus Q^{(2)} \oplus T^{(0)} \oplus T^{(2)} \oplus T^{(4)}, \end{aligned} \quad (6)$$

where

$$Q^{(0)} \equiv \langle\langle D^{(0)} \otimes D^{(0)} \rangle\rangle, \quad (7a)$$

$$Q^{(2)} \equiv 2 \langle\langle D^{(0)} \otimes D^{(2)} \rangle\rangle, \quad (7b)$$

$$T \equiv \langle\langle D^{(2)} \otimes D^{(2)} \rangle\rangle = T^{(0)} \oplus T^{(2)} \oplus T^{(4)}. \quad (7c)$$

Formally, this corresponds to the addition of two quantum angular momenta with $\ell = 0$ or $\ell = 2$, see graphical representation in Fig. 1b. As it is known from quantum mechanics⁵⁴, addition of angular momenta ℓ_1 and ℓ_2 yields all possible states with momenta between $|\ell_1 - \ell_2|$ and $\ell_1 + \ell_2$. Mathematically speaking⁵⁵, the tensor product of irreducible representations is reducible, and decomposes into a direct sum of irreducible representations. Tensors $Q^{(\ell)}$ and $T^{(\ell)}$ in Eqs. (6)–(7) belong to the $(2\ell + 1)$ -dimensional irreducible representations V_ℓ of $\text{SO}(3)$ with the angular momenta $\ell = 0, 2, 4$, according to $V_0 \otimes V_0 \cong V_0$, $V_0 \otimes V_2 \cong V_2$, and $\text{Sym}(V_2 \otimes V_2) \cong V_0 \oplus V_2 \oplus V_4$. Here $\text{Sym}(\cdot)$ indicates that we consider the symmetric part of the tensor product due to the major symmetry of C , such that the representations with odd $\ell = 1, 3$ in the $V_2 \otimes V_2$ case do not contribute. This irreducible decomposition yields the DOF count for C tensor: $21 = 1 + 5 + 1 + 5 + 9$.

The physical intuition behind this formalism is as follows. In a distribution $\mathcal{P}(D)$ of compartmental diffusion tensors of Fig. 1a, each ellipsoid (4) has an isotropic (“size”) part $D^{(0)}$ and trace-free anisotropic (“shape”) part $D^{(2)}$. Thus, the direct products in Eq. (7) define the size variance $Q^{(0)}$, the size-shape covariance $Q^{(2)}$, and the shape-shape covariance T , Fig. 1b,c.

The latter covariance is reducible and further splits into three irreducible spherical tensors $T^{(0)}$, $T^{(2)}$ and $T^{(4)}$.

Besides the explicit classification based on symmetries, the benefit of using spherical tensors is in having the minimal number of DOF in each of them, as compared to the highly redundant Cartesian objects such as C_{ijkl} . Therefore, one expects that the covariances $\langle\langle D^{\ell_1 m_1} D^{\ell_2 m_2} \rangle\rangle$ of the spherical-tensor components (4) of compartmental diffusivities should be related to the corresponding spherical-tensor components of Q and T , Fig. 1c. We derive these explicit relations based on the spherical tensor algebra in Supplementary Section S2. In brief, the relations for Q ,

$$Q^{00} = \langle\langle (D^{00})^2 \rangle\rangle, \quad Q^{2m} = 2 \langle\langle D^{00} D^{2m} \rangle\rangle, \quad (8a)$$

follow trivially from Eqs. (7a) and (7b). However, Eq. (7c)

$$T^{\ell m} = \langle 2020 | \ell 0 \rangle \sum_{m_1 + m_2 = m} \langle 2m_1 2m_2 | \ell m \rangle \langle\langle D^{2m_1} D^{2m_2} \rangle\rangle \quad (8b)$$

involves the Clebsch-Gordan coefficients⁵⁴ $\langle \ell_1 m_1 \ell_2 m_2 | \ell m \rangle$ which obey the selection rule $m_1 + m_2 = m$ and vanish otherwise. This rule makes the system (8) so sparse that it can be inverted by hand, cf. Supplementary Eq. (S22). This provides an analytical solution for the tissue properties $\langle\langle D^{\ell_1 m_1} D^{\ell_2 m_2} \rangle\rangle$ in terms of the spherical components of T and Q , i.e., the irreducible components of covariance tensor C . We call Eqs. (6)–(8) the *QT decomposition* of covariance tensor.

Equations (6)–(8) straightforwardly extend for time-dependent $D(t)$, with the $Q(t)$ and $T(t)$ tensors picking up the diffusion time dependence via $\langle\langle D^{\ell_1 m_1}(t) D^{\ell_2 m_2}(t) \rangle\rangle$. This general case will be considered in Eqs. (36)–(38). In the meantime, we assume Gaussian compartments, such that the cumulant series is fully determined by the B -tensors, Eqs. (1)–(2).

Q and T tensor components from B-tensor shells

The rank of the B tensor reflects how many dimensions of the diffusion process are being probed simultaneously; rank $B > 1$ means probing the diffusion along more than one dimension. An example is the axially symmetric family^{22,56}

$$B_{ij}(b, \beta, \hat{\mathbf{g}}) = b \left(\beta g_i g_j + \frac{1-\beta}{3} \delta_{ij} \right) \quad (9)$$

parametrized by its trace b setting the overall scale; by the unit vector $\hat{\mathbf{g}}$ along the symmetry axis; and by shape parameter β .

Historically, diffusion weightings in MR have mostly probed a single direction $\hat{\mathbf{g}}$ per measurement, using pulsed gradients⁵⁷, such that $B_{ij} = b g_i g_j$; this so-called linear tensor encoding (LTE, $\beta = 1$) corresponds to rank $B = 1$. Varying β changes the B -tensor shape, e.g., $\beta = 0$ for spherical tensor encoding (STE, isotropic B -tensor), and $\beta = -\frac{1}{2}$ for planar tensor encoding (PTE, two equal nonzero eigenvalues)^{3,18–22}.

Imaging voxels in the brain have vastly different fiber orientation dispersion and, as a result, distinct orientations and degrees of anisotropy of the underlying $\mathcal{P}(D)$. It is therefore

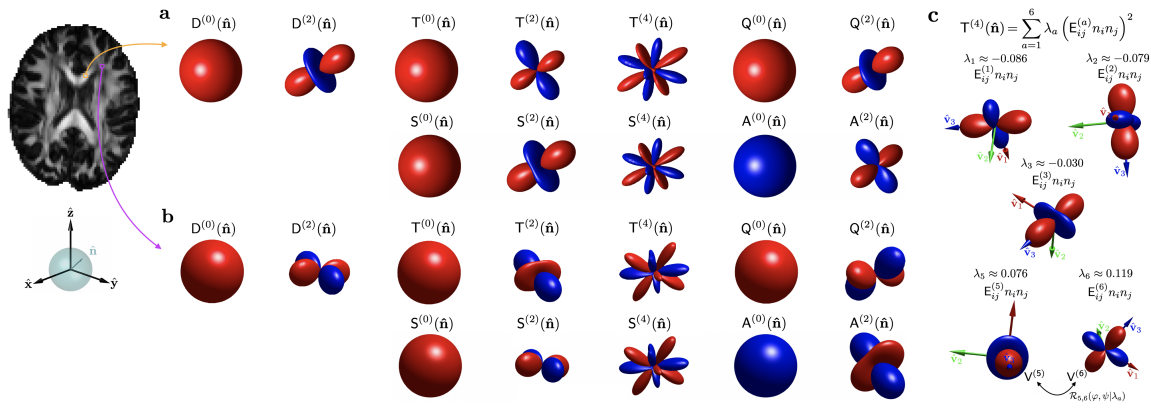


FIG. 2. Irreducible decompositions of D and C tensors, Eqs. (4), (7), and (16), for two white matter voxels: (a) corpus callosum — highly aligned fibers, and (b) longitudinal superior fasciculus — crossing fibers. Glyphs are color-coded by the sign (red = positive) while the radius represents the absolute value (rescaled to similar sizes). (c) Representation of the eigentensor decomposition, Eq. (64) in *Methods*, of $T^{(4)}$ for the crossing fiber voxel shown in (b). The 6 invariants of $T^{(4)} = S^{(4)}$ (cf. Fig. 3) correspond to 4 DOF from λ_a (here $\lambda_4 = 0$, $E_{ij}^{(4)} \propto \delta_{ij}$, and $\sum_{a=1}^6 \lambda_a = 0$), and 2 DOF defining the relative orientations among any pair of eigentensors $E_{ij}^{(a)}$.

natural for a dMRI measurement to probe all directions uniformly. The most general B-tensor is defined by its shape (3 eigenvalues summing up to the diffusion weighting b), and the 3 orientational DOF. Uniformly sampling all the orientations of B amounts to acting on it by all possible elements of the SO(3) group. Thus, a fixed- b “shell” for a generic B-tensor is the group manifold of SO(3), which is the 3-dimensional sphere \mathbb{S}^3 (the group manifold of its universal cover SU(2)) with the antipodal points identified⁵⁵. In other words, a fixed- b shell is a quotient space $\mathbb{S}^3/\mathbb{Z}_2$, where the factorization modulo group $\mathbb{Z}_2 = \{1, -1\}$ corresponds to gluing the antipodal points. Maximally isotropic coverage with B-tensors amounts to a maximally uniform sampling of such a 3-sphere.

Acquisitions with axially symmetric B-tensors (9) are invariant under SO(2) rotations around \hat{g} . Factorization of the group manifold over SO(2) $\cong \mathbb{S}^1$ (a unit circle) results in a familiar 2-dimensional spherical shell $\mathbb{S}^2 \cong \text{SO}(3)/\text{SO}(2)$. Topologically, it is a quotient space $\mathbb{S}^2 \cong \mathbb{S}^3/\mathbb{S}^1$ of a 3-sphere over a circle, known as Hopf fibration⁵⁸. (As \mathbb{Z}_2 is a subgroup of SO(2), the factorization over it is contained in the quotient.)

Hence, the signal (1) for axially symmetric B-tensors (9), as function of the unit $\hat{g} \in \mathbb{S}^2$, can be represented in the canonical spherical harmonics basis on \mathbb{S}^2 . The spherical harmonics components of its logarithm $\mathcal{L} = \ln \langle \mathcal{S} \rangle$ up to $\mathcal{O}(b^2)$ are found by averaging the compartment signal $\mathcal{S} = \exp[-bD(\hat{g})] = \exp[-bD^{00} - \beta b \sum D^{2m} Y^{2m}(\hat{g})]$ over $\mathcal{P}(D)$:

$$\mathcal{L}^{00}(b, \beta) = -bD^{00} + \frac{1}{2} b^2 (Q^{00} + \beta^2 T^{00}), \quad (10a)$$

$$\mathcal{L}^{2m}(b, \beta) = -b\beta D^{2m} + \frac{1}{2} b^2 (\beta Q^{2m} + \beta^2 T^{2m}), \quad (10b)$$

$$\mathcal{L}^{4m}(b, \beta) = \frac{1}{2} b^2 \beta^2 T^{4m}. \quad (10c)$$

While components of D and Q appear naturally using Eqs. (3) and (8a), the components (8b) of T arise via the triple spherical harmonics integration, Supplementary Eq. (S14). The corollaries of Eqs. (10) are as follows:

(i) *Sufficiency*: Axially symmetric family (9) on the quo-

tient space \mathbb{S}^2 is sufficient for estimating all 21 DOF of C; the entire SO(3) manifold (non-axial B) is not necessary.

- (ii) *Necessity*: To estimate all tensor components, one needs 3 distinct combinations (b, β) , with at least 2 nonzero b and at least 2 nonzero β (i.e., 2 non-STE B tensors).
- (iii) *STE* ($\beta = 0$) can be used to isolate Q^{00} , as $\mathcal{L}_{\text{STE}} = -bD^{00} + \frac{1}{2} b^2 Q^{00}$ including $\mathcal{O}(b^2)$ ^{15,21,22,59}.
- (iv) *Conventional LTE* ($\beta = 1$) alone cannot disentangle $Q^{(\ell)}$ and $T^{(\ell)}$, for both $\ell = 0$ and 2, from their sums.

As LTE plays a major role in everyday dMRI and in publicly available datasets⁴¹⁻⁴⁵, we now consider it in detail.

LTE versus other B-tensor shapes: SA decomposition

For LTE, $B_{ij} B_{kl} \rightarrow b^2 g_i g_j g_k g_l$ becomes symmetric in all indices⁶⁰, and Eq. (1) turns into the diffusion kurtosis imaging (DKI) signal representation⁶¹:

$$\ln \langle \mathcal{S} \rangle = -bD(\hat{g}) + \frac{b^2}{2} S(\hat{g}) + \mathcal{O}(b^3), \quad S(\hat{g}) = S_{ijkl} g_i g_j g_k g_l, \quad (11)$$

where S, the *fully symmetric* part of C,

$$S_{ijkl} = C_{ijkl} = \frac{1}{3} (C_{ijkl} + C_{iljk} + C_{iklj}) \equiv \frac{1}{3} D_{00}^2 W_{ijkl}, \quad (12)$$

is proportional to the dimensionless *kurtosis tensor* W — a 3d generalization of the kurtosis excess for the probability distribution of molecular displacements⁶¹. The tensor-algebra notation⁵³ for symmetrization over tensor indices between parentheses is assumed henceforth, e.g., $D_{(ij)} = \frac{1}{2} (D_{ij} + D_{ji})$. Since W and S contain the same information, we will focus on S, and refer to both S and W as kurtosis.

Kurtosis splits into irreducible components with $\ell = 0, 2, 4$:

$$S_{ijkl} = S^{00} \delta_{(ij} \delta_{kl)} + \sum_{m=-2}^2 S^{2m} Y_{(ij}^{2m} \delta_{kl)} + \sum_{m=-4}^4 S^{4m} Y_{ijkl}^{4m} \quad (13)$$

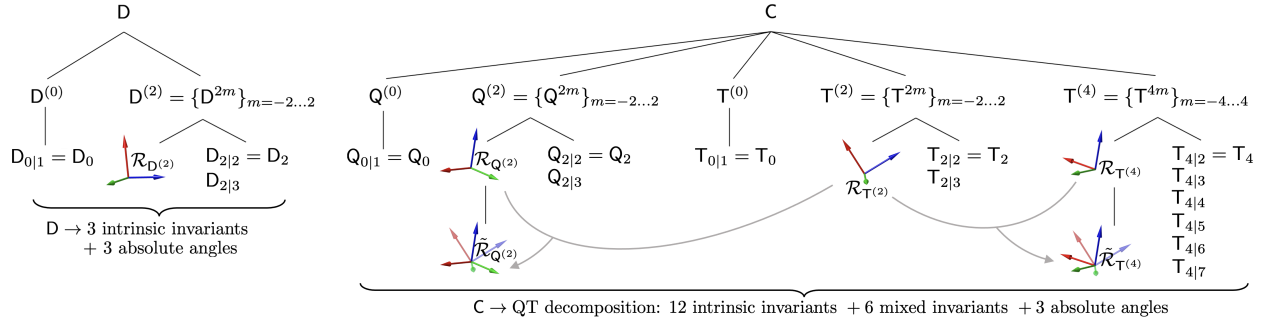


FIG. 3. Irreducible decompositions of tensors D and C (into Q and T), Eqs. (4)–(6). Each irreducible component has its intrinsic invariants (1 for $\ell = 0$; 2 for $\ell = 2$; and 6 for $\ell = 4$). Together with these $1 + 2 + 1 + 2 + 6 = 12$ intrinsic invariants, C has $3 \cdot 3 = 9$ basis-dependent absolute angles defining the orientations of its $T^{(2)}$, $T^{(4)}$, and $Q^{(2)}$ via the rotation matrices $\mathcal{R}_{Q^{(2)}}$, $\mathcal{R}_{T^{(2)}}$, and $\mathcal{R}_{T^{(4)}}$, such that total DOF count of C is $21 = 12 + 9$. Out of these 9 absolute angles, 6 DOF are mixed invariants since they correspond to relative angles between $Q^{(2)}$, $T^{(2)}$ and $T^{(4)}$. As an example, we take $\mathcal{R}_{T^{(2)}}$ as a reference, and compute the relative rotations $\tilde{\mathcal{R}}_{T^{(4)}}$ and $\tilde{\mathcal{R}}_{Q^{(2)}}$. Maps of these invariants are shown in Fig. 4.

such that $S(\hat{\mathbf{g}}) = S^{(0)} + S^{(2)}(\hat{\mathbf{g}}) + S^{(4)}(\hat{\mathbf{g}})$, where spherical tensors $S^{(0)}$, $S^{(2)}$ and $S^{(4)}$ are parametrized by $2\ell + 1 = 1, 5$ and 9 spherical harmonics coefficients, respectively, totaling $1 + 5 + 9 = 15$ DOF, found from S_{ijkl} via Eqs. (55) in *Methods*.

The remaining $21 - 15 = 6$ DOF of C are contained in the *asymmetric* (not antisymmetric!) part A of C :

$$A_{ijkl} = C_{ijkl} - C_{(ijkl)} = \frac{1}{3}(2C_{ijkl} - C_{iljk} - C_{ikjl}). \quad (14)$$

To measure all DOF of C , and thereby to access A , the necessary and sufficient condition is the corollary (ii) after Eq. (10), which makes the requirement²¹ $\text{rank } B > 1$ more precise. Although A is a 4th-order Cartesian tensor, it has only 6 DOF, and thus it is equivalent to a symmetric 3×3 tensor^{62,63}:

$$A_{pq} = \epsilon_{ikp} \epsilon_{jlq} A_{ijkl} \quad (15a)$$

$$= \delta_{pq} (A_{iikk} - A_{ikik}) + 2(A_{pkqk} - A_{pqkk}), \quad (15b)$$

$$A_{ijkl} = \frac{1}{6} (\epsilon_{ikp} \epsilon_{jlq} + \epsilon_{ilp} \epsilon_{jkq}) A_{pq}, \quad (15c)$$

where ϵ_{ijk} is the fully antisymmetric Levi-Civita tensor. Thus, analogously to Eq. (4), tensor A splits into the irreducible components with $\ell = 0$ and 2, cf. Eqs. (55).

We define the above irreducible components as the *SA decomposition* of C (which stands for symmetric-asymmetric):

$$C = S \oplus A, \quad (16)$$

$$S = S^{(0)} \oplus S^{(2)} \oplus S^{(4)}, \quad A = A^{(0)} \oplus A^{(2)},$$

where the DOF count holds: $21_C = (1 + 5 + 9)_S + (1 + 5)_A$. The separation of information accessible through LTE (S) vs beyond-LTE (A) implies that the SA decomposition is *LTE-driven*. Hundreds of thousands datasets acquired with LTE and moderate diffusion weightings are available^{41–45}, and thus are sensitive to the information present in S only.

The contributions of SA decomposition to $O(b^2)$ term of the cumulant expansion (1) for B tensor family (9) are

$$B_{ij} B_{kl} S_{ijkl} = b^2 \left[\frac{5+4\beta^2}{9} S^{(0)} + \frac{7\beta+2\beta^2}{9} S^{(2)}(\hat{\mathbf{g}}) + \beta^2 S^{(4)}(\hat{\mathbf{g}}) \right], \quad (17a)$$

$$B_{ij} B_{kl} A_{ijkl} = \frac{2}{9} b^2 \left[(1 - \beta^2) A^{(0)} - \beta(1 - \beta) A^{(2)}(\hat{\mathbf{g}}) \right]. \quad (17b)$$

To obtain Eqs. (17), we used Eq. (15) and Supplementary Eq. (S1), such that $S^{(0)} \equiv S^{00}$, $A^{(0)} \equiv A^{00} = \frac{1}{3} A_{pp} = \frac{1}{3} (A_{iikk} - A_{ikik})$, and $A^{(2)}(\hat{\mathbf{g}}) = A_{pq} g_p g_q$. As expected, STE is sensitive only to the isotropic parts $S^{(0)}$ and $A^{(0)}$, while LTE couples to $S(\hat{\mathbf{g}})$ and is insensitive to $A(\hat{\mathbf{g}})$ (Eq. (17b) vanishes). PTE couples to the A tensor ellipsoid, Eq. (17b) yielding $+\frac{b^2}{6} A(\hat{\mathbf{g}})$, and to the combination $b^2 (\frac{2}{3} S^{(0)} - \frac{1}{3} S^{(2)}(\hat{\mathbf{g}}) + \frac{1}{4} S^{(4)}(\hat{\mathbf{g}}))$ via Eq. (17a). At fixed b , LTE maximizes the sensitivity to $S^{(0)}$, $S^{(2)}$, $S^{(4)}$; STE — to $A^{(0)}$; and PTE — to $A^{(2)}$.

Comparing $O(b^2)$ terms of Eqs. (10) to the half-sum of Eqs. (17), we relate the irreducible components of QT and SA decompositions:

$$Q^{(0)} = \frac{5}{9} S^{(0)} + \frac{2}{9} A^{(0)}, \quad (18a)$$

$$Q^{(2)} = \frac{7}{9} S^{(2)} - \frac{2}{9} A^{(2)}, \quad (18b)$$

$$T^{(0)} = \frac{4}{9} S^{(0)} - \frac{2}{9} A^{(0)}, \quad (18c)$$

$$T^{(2)} = \frac{2}{9} S^{(2)} + \frac{2}{9} A^{(2)}, \quad (18d)$$

$$T^{(4)} = S^{(4)}. \quad (18e)$$

These relations respect

$$S^{(\ell)} = Q^{(\ell)} + T^{(\ell)}, \quad (19)$$

evident by comparing Eqs. (11) and (10) for $\beta = 1$, and formally setting $Q^{(4)} \equiv 0$. Upon SO(3) rotations, components $S^{(\ell)}$, $A^{(\ell)}$, or $T^{(\ell)}$, $Q^{(\ell)}$, do not mix with each other.

Which decomposition is more “fundamental”? Since each representation with $\ell = 0$ and $\ell = 2$ enters Eq. (6) twice, *any* decomposition of C with two independent linear combinations of representations with $\ell = 0$, and separately for $\ell = 2$, is legitimate. The decompositions (7) and (16) are selected by their distinct physical meaning: The SA decomposition breaks symmetry between the LTE and non-LTE acquisitions, while the QT decomposition is natural to describe tissue properties.

The geometric meaning of the irreducible decompositions such as (4), (7), and (16), comes from the correspondence between spherical tensors and spherical harmonics (cf. Eq. (45)

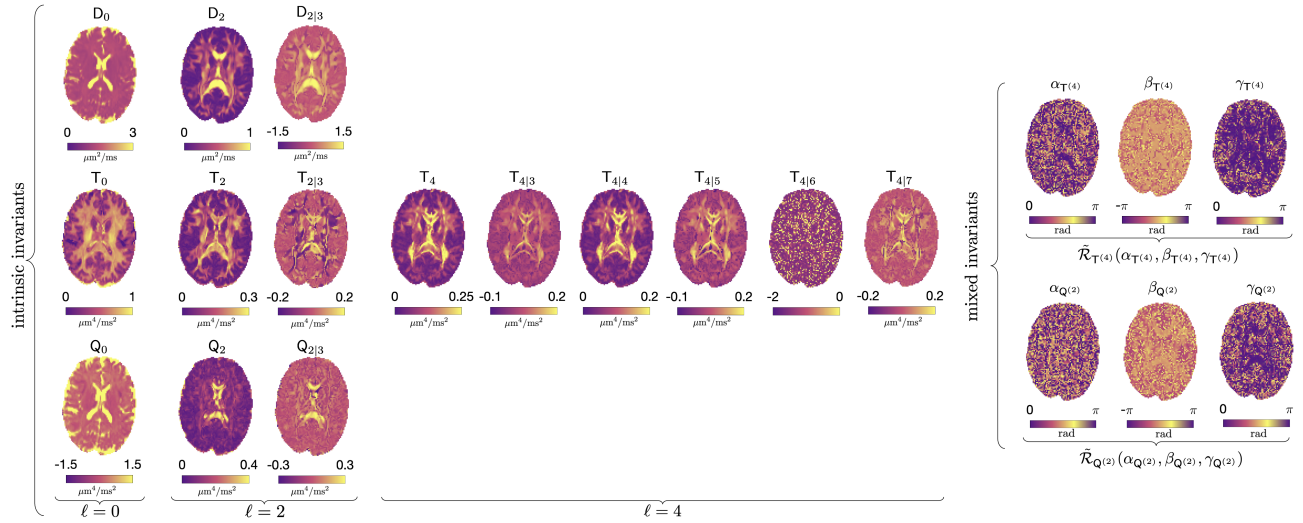


FIG. 4. RICE maps for a normal brain (33 y.o. male). Intrinsic invariants for each irreducible decomposition of D , T and Q are shown as powers of corresponding traces, to match units of D and C . The 6 mixed invariants correspond to Euler angles of eigenframes of $T^{(4)}$ and $Q^{(2)}$ relative to that of $T^{(2)}$ (see text). The underlying tissue microstructure introduces correlations between invariants: e.g. small relative angles β in white matter tracts exemplify the alignment of eigenframes of different representations of $SO(3)$ with the tract.

in *Methods*), Fig. 2. The $\ell = 0$ parts give directional averages; the $\ell = 2$ parts are responsible for glyphs parametrized by five $Y^{2m}(\hat{\mathbf{n}})$, turning the corresponding ball into an ellipsoid, such as $D(\hat{\mathbf{n}}) = D_{ij}n_i n_j$ in DTI². The $\ell = 0$ and $\ell = 2$ parts can capture a single fiber tract (a single pair of opposite lobes on a sphere, both at the $O(b)$ and $O(b^2)$ level), but cannot represent geometries with multiple pairs of lobes, such as in fiber crossings. The unique $T^{(4)} = S^{(4)}$ part, parametrized by nine $Y^{4m}(\hat{\mathbf{n}})$, is the only part of C that captures multiple pairs of lobes coming from fiber crossings, see, e.g., Fig. 2c. Thereby, the beyond-LTE A -tensor part of C can only accommodate an ellipsoidal glyph shape — albeit physically distinct from that of the diffusion tensor.

As for the parameter estimation, one can either directly use Eqs. (10), or go the SA route (12) and (14) to compute the irreducible components $S^{(\ell)}$ and $A^{(\ell)}$ [Eqs. (55) in *Methods*], and then transform to QT via Eqs. (18). Once the irreducible components of Q and T tensors are known, tissue properties (compartmental spherical tensor covariances) can be found by inverting Eqs. (8), see Supplementary Eqs. (S22).

Above, the source of kurtosis in Eq. (11) was solely the heterogeneity of compartment tensors D , also responsible for the covariance (2). For non-Gaussian compartments, each characterized by its own microscopic kurtosis tensor $S(t)$, the narrow-pulse LTE⁵⁷ DKI signal, compared to Eq. (11), reads

$$\begin{aligned} \ln \langle S \rangle &= \ln \left\langle e^{-bD(t, \hat{\mathbf{g}}) + \frac{1}{2}b^2S(t, \hat{\mathbf{g}}) + O(b^3)} \right\rangle \\ &= -bD(t, \hat{\mathbf{g}}) + \frac{b^2}{2} [S(t, \hat{\mathbf{g}}) + S_\mu(t, \hat{\mathbf{g}})] + O(b^3), \end{aligned} \quad (20)$$

where $D(t, \hat{\mathbf{g}}) = D_{ij}(t)g_i g_j$, $S(t)$ is the symmetric part of $C(t)$, cf. Eq. (12), and the overall microscopic kurtosis tensor

$$S_\mu(t) = \langle S(t) \rangle \quad (21)$$

contributes to the overall kurtosis tensor $S(t) + S_\mu(t)$. Hence, LTE cannot separate intrinsic and heterogeneity-based kurtosis contributions. In other words, while one can still “rotate” from $Q(t)$ and $T(t)$ via Eqs. (18) to $S(t)$ and $A(t)$, the resulting S tensor will not yield the measured overall kurtosis via Eq. (20). To determine the $Q(t)$, $T(t)$ and $S_\mu(t)$ tensors one has to go beyond Eq. (1), as discussed in Eqs. (36)–(38).

Invariants: intrinsic and mixed

Tensor invariants are the combinations of parameters that do not change upon rotations of the basis. We now construct all invariants of C within either QT or SA decomposition, by splitting them into the ones intrinsic to a given irreducible representation, and the ones mixing representations. Let us define *intrinsic invariants* as those that belong purely to a single irreducible component, such as $Q^{(\ell)}$ and $T^{(\ell)}$ in Eq. (7), or $S^{(\ell)}$ and $A^{(\ell)}$ in Eq. (16). Conversely, *mixed invariants* determine the relative orientations between different irreducible components with $\ell > 0$, such as between $T^{(2)}$ and $T^{(4)}$. In what follows, we will focus on the invariants of the QT decomposition, Fig. 3, with all maps for a human brain shown in Fig. 4. A completely analogous treatment yields the corresponding S and A invariants, cf. Supplementary Fig. S1.

How many intrinsic and mixed invariants are there? First note that the total number of invariants for any tensor equals its number of DOF minus 3 angles defining its overall orientation⁶⁴, yielding 3 for D (DTI), 12 for S or W (DKI), and 18 for C . Applying this argument to each irreducible representation, the number of intrinsic invariants is 1 for $\ell = 0$, and $(2\ell + 1) - 3 = 2(\ell - 1) = 2, 6, \dots$ for $\ell = 2, 4, \dots$. This yields $(1 + 2 + 6) + (1 + 2) = 12$ intrinsic invariants of C , Fig. 3.

The isotropic, $\ell = 0$ component of a symmetric tensor is an

invariant, normalized here to its angular average as in Eq. (5):

$$\begin{aligned} A_0 &\equiv A^{00} = \overline{A(\hat{n})} = \frac{1}{3}A_{ii}, \\ S_0 &\equiv S^{00} = \overline{S(\hat{n})} = \frac{1}{5}S_{iiji}, \end{aligned} \quad (22)$$

cf. Eq. (55). The respective invariants $Q_0 \equiv Q^{00}$ and $T_0 \equiv T^{00}$ are given in terms of S_0 and A_0 via Eqs. (18a) and (18c).

Consider now the irreducible components with $\ell = 2$. We take $D^{(2)}$ as an example, with the analogous definitions for $T^{(2)}$, $Q^{(2)}$, $S^{(2)}$, and $A^{(2)}$. Among the 5 DOF, 3 angles define the orientation of the glyph $D^{(2)}(\hat{n})$ and are not invariants. The remaining 2 DOF parametrize the 3 eigenvalues that sum up to zero trace. The corresponding 2 invariants can be written as traces of the powers of $D^{(2)}$, where we introduce the index notation $\ell|n$ useful for higher ℓ in what follows:

$$D_{2|n} = \left(\frac{2}{3} \operatorname{tr}(D^{(2)})^n\right)^{1/n}, \quad n = 2, 3. \quad (23)$$

Since $n = 2$ invariants (L_2 -norm) play special role^{28,32,33}, we will henceforth drop the $n = 2$ index for degrees $\ell \geq 2$, Fig. 3.

Based on the definition (23), the square of $D_2 \equiv D_{2|2}$,

$$D_2^2 = 2 \mathbb{V}_\lambda(D), \quad \mathbb{V}_\lambda(D) \equiv \frac{1}{3} \sum_{i=1}^3 (\lambda_i - \bar{\lambda})^2, \quad (24)$$

is related to the variance $\mathbb{V}_\lambda(D)$ of the eigenvalues of D . Geometrically, D_2^2 characterizes the *directional variance*

$$\operatorname{var} D(\hat{n}) = \overline{D^2(\hat{n})} - D_0^2 = \frac{1}{5}D_2^2, \quad D_2^2 \equiv \sum_m D^{2m*} D^{2m}, \quad (25)$$

cf. the expansion (3) and spherical harmonics orthogonality. The equivalence of the directional and eigenvalue variances³⁵ is readily seen in the eigenbasis: for $D^{(2)} = \operatorname{diag}\{\eta_1, \eta_2, -\eta_+\}$, where $\eta_\pm = \eta_1 \pm \eta_2$, using $D^{2m} = \frac{2}{3} \mathcal{Y}_{ij}^{2m*} D_{ij}$, cf. Eq. (55) from *Methods*, we get $D^{2,\pm 2} = \eta_-/\sqrt{6}$, $D^{2,\pm 1} = 0$, and $D^{20} = -\eta_+$, proving $\sum_m |D^{2m}|^2 = 2 \cdot \frac{1}{3} (\eta_1^2 + \eta_2^2 + \eta_+^2)$, cf. Eq. (24).

The invariants D_0 , D_2 , and $D_{2|3}^3 = 2 \det D^{(2)}$ (the volume of the ellipsoid $D(\hat{n})$), provide 3 symmetrized combinations of the eigenvalues of $D^{(0)} \oplus D^{(2)}$ which fully determine its shape.

For the $\ell = 4$ components $T^{(4)} = S^{(4)}$, the picture is more complex. The 3 angles determine the orientation of the glyph $T^{(4)}(\hat{n}) = \sum_{m=-4}^4 T^{4m} Y^{4m}(\hat{n})$, while the remaining 6 DOF determine its shape (Fig. 2a,b). Here we construct the principal invariant $T_4 \equiv T_{4|2}$, the glyph variance analogously to Eq. (25):

$$\operatorname{var} T^{(4)}(\hat{n}) = \frac{1}{9}T_4^2, \quad T_4^2 \equiv \sum_m T^{4m*} T^{4m} = \frac{8}{35} T_{ijkl}^{(4)} T_{ijkl}^{(4)}, \quad (26)$$

where the normalization factor in the last equality follows from Eq. (48) in *Methods*. The remaining 5 intrinsic invariants are constructed in Eq. (68) of *Methods*.

The relative angles between irreducible components of a given tensor do not change upon rotations (the tensor transforms as a whole). Hence, $18 - 12 = 6$ DOF define the two sets of mixed invariants of C that parametrize the relative rotations between the frames of $T^{(4)}$, $Q^{(2)}$, and $T^{(2)}$. Without the loss

of generality, we take them as the Euler angles that define active rotations $\tilde{\mathcal{R}}_T^{(4)}(\alpha_T^{(4)}, \beta_T^{(4)}, \gamma_T^{(4)})$ and $\tilde{\mathcal{R}}_Q^{(2)}(\alpha_Q^{(2)}, \beta_Q^{(2)}, \gamma_Q^{(2)})$ of the $T^{(2)}$ frame along z by α , then along new x' by β , and along new z'' by γ to obtain the $T^{(4)}$ and $Q^{(2)}$ frames (Fig. 3). These are mapped for the human brain in the right panel of Fig. 4 (cf. Supplementary Fig. S1 for S and A).

The major and minor symmetries of C mimic those of the elasticity tensor in continuous media. The proposed construction of tensor invariants via representation theory has the benefit of symmetry and geometric meaning, as compared to approaches within the elasticity theory⁴⁹⁻⁵², and later in dMRI⁶⁵⁻⁶⁷. Previous works used a Cartesian representation of C as a symmetric 6×6 matrix (Kelvin/Voigt notation, Eq. (61) in *Methods*). The invariants (generally, not a complete set) were introduced as coefficients of the characteristic polynomial of two variables in the 6×6 matrix representation of C ^{50,65} or of S ⁶⁶, or via Hilbert's theorem on non-negative ternary quartics⁶⁷ for S .

Previously used dMRI contrasts from RICE

The present unifying group theory approach allows us to express all previously used $O(b^2)$ dMRI contrasts, sometimes related to specific acquisition schemes, via the smallest possible subset of the full system of invariants. Below we express the most popular contrasts in terms of only 4 invariants: 2 from D (D_0 and D_2), and 2 from C (Q_0 and T_0).

The $O(b)$ contrasts, MD (5) and fractional anisotropy

$$FA \equiv \sqrt{\frac{3}{2} \frac{\mathbb{V}_\lambda(D)}{\mathbb{V}_\lambda(D) + D_0^2}} = \sqrt{\frac{3D_2^2}{2D_2^2 + 4D_0^2}} \quad (27)$$

[cf. Eq. (24)], involve only D_0 and D_2 . Although the dimensionless ratio D_2/D_0 is a more natural way to quantify the anisotropy of D tensor given Eq. (25), the function (27) of D_2/D_0 , bounded by $0 \leq FA \leq 1$, has been widely used; the bounding leads to a less transparent noise propagation.

Including Q_0 and T_0 yields a number of $O(b^2)$ contrasts. We begin with mean kurtosis (MK), cf. Eqs. (12) and (19):

$$MK \equiv \overline{W(\hat{n})} = W_0 = \frac{3\overline{S(\hat{n})}}{D_0^2} = \frac{3S_0}{D_0^2}, \quad S_0 = Q_0 + T_0, \quad (28)$$

defined via the directional average of W ^{68,69}. Eq. (28) is sometimes referred to as mean kurtosis tensor (MKT)⁷⁰, as it is equivalent to the tensor trace $W_0 = \frac{1}{5}W_{iiji}$ and, thus, can be computed fast and precisely. The original DKI paper⁶¹ defined mean kurtosis as the directional average of $K(\hat{n}) = 3S(\hat{n})/D^2(\hat{n})$. While perhaps more intuitive, that definition suffers from two drawbacks. First, it cannot be compactly represented as a trace of a tensor [akin to Eqs. (23) and (68)] due to a nontrivial directional dependence of the denominator. Indeed, as $K(\hat{n})$ involves an *infinite series* in the powers of \hat{n} due to the expansion of $1/D^2(\hat{n})$ in the powers of $D^{(2)}(\hat{n})$, it cannot be written as a convolution of a product $n_i n_j \dots$ with a tensor or even a few tensors⁷¹. Second, $\overline{K(\hat{n})}$ has lower

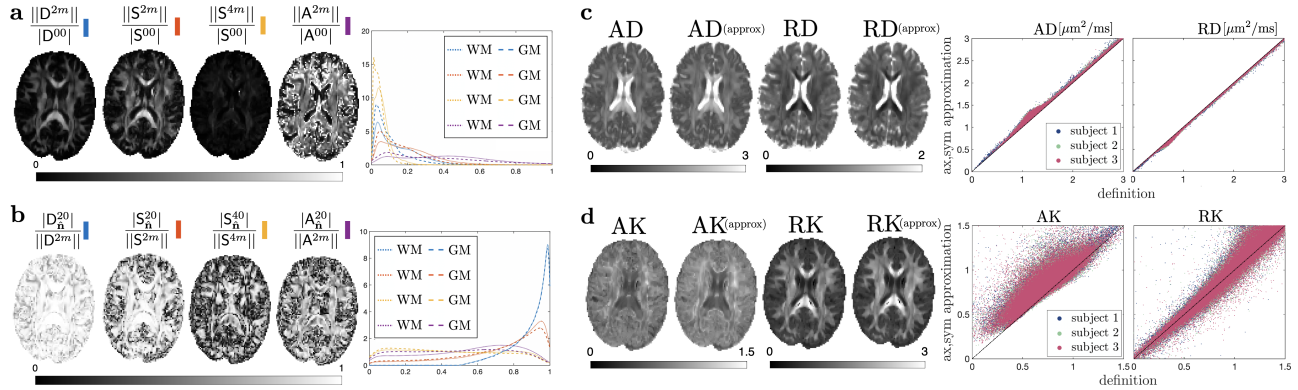


FIG. 5. Significance of $\ell > 0$ and axial symmetry in healthy brains. (a) Normalized maps of the L_2 -norms for degree- ℓ components of D , $S \propto W$, and A , and their histograms for white and gray matter (WM, GM) voxels. S^{4m} elements are 5–10× smaller than S^{00} . (b) Relative contribution of the $m = 0$ components in the principal fiber coordinate frame, such ratio = 1 for perfect axial symmetry. (c,d): Axial and radial projections of the diffusion (c) and kurtosis (d) tensors, calculated both exactly and via Eqs. (32) relying on the axial symmetry approximation.

precision than Eq. (28), and is strongly affected by outliers coming from low-diffusivity directions, for which $D(\hat{n}) \ll D_0$.

The curvature $\mathbb{V}_I = Q_0$ of the STE cumulant series \mathcal{L}_{STE} [item (iii) below Eqs. (10)] is known as the *isotropic variance*^{21,22}. Speaking precisely, it is the variance of isotropic components of compartment tensors. The directional average of the LTE signal, represented in the cumulant form $\ln\langle\tilde{S}_{\text{LTE}}\rangle = -bD_0 + \frac{1}{2}b^2\mathbb{V}_A + O(b^3)$, defines the so-called *anisotropic variance*^{59,72}

$$\mathbb{V}_A \equiv \left\langle \overline{D^2(\hat{n})} \right\rangle - D_0^2 = \frac{2}{5} \langle \mathbb{V}_A(D) \rangle = \frac{1}{5} \langle D_2^2 \rangle = T_0 + \frac{1}{5}D_2^2, \quad (29)$$

proportional to the variance (24) of the eigenvalues of compartmental D averaged over $\mathcal{P}(D)$. Note that taking spherical mean of LTE signal before the logarithm makes \mathbb{V}_A a moment, rather than a cumulant: $\langle D_2^2 \rangle = \sum_m \langle D^{2m*} D^{2m} \rangle = 5T_0 + \sum_m D^{2m*} D^{2m}$, cf. Eq. (60). The above variances define the isotropic and anisotropic kurtoses $K_{I,A} = 3\mathbb{V}_{I,A}/D_0^2$, cf. Eq. (28)^{21,22,26,59,72}. Note that this somewhat misleading nomenclature refers to iso/anisotropic components of compartmental diffusion tensors, while all the above quantities correspond to the *fully isotropic* ($\ell = 0$) parts of C , Eq. (6).

Finally, the analogy with Eq. (27) has motivated the definition of *microscopic fractional anisotropy*^{21,25,59,72}

$$\mu\text{FA} \equiv \sqrt{\frac{3}{2} \frac{\langle \mathbb{V}_A(D) \rangle}{\langle \mathbb{V}_A(D) \rangle + D_0^2}} = \sqrt{\frac{15T_0 + 3D_2^2}{10T_0 + 2D_2^2 + 4D_0^2}}. \quad (30)$$

Writing μFA using RICE invariants enables its evaluation without the need to assume axial symmetry for D and/or a specific functional form for $\mathcal{P}(D)$, as in Refs.^{22,59}. Note that the definition of μFA is inconsistent, in a sense that the averages over $\mathcal{P}(D)$ are taken in the numerator and denominator separately, i.e., μFA is *not* the compartmental FA(D) averaged over $\mathcal{P}(D)$ ⁷³. Unfortunately, information for calculating voxel-averaged $\langle \text{FA}(D) \rangle$ is not contained in the $O(b^2)$ signal, as it involves all higher-order cumulants.

All the above 6 popular contrasts — W_0 , $\mathbb{V}_{I,A}$, $K_{I,A}$, μFA —

rely just on two $\ell = 0$ invariants of C , and are thereby redundant. Contrasts involving higher-degree invariants have been largely unexplored. Empirically, one can rationalize this as the invariants decrease with ℓ , shown in Fig. 5a for the $\ell = 2$ and $\ell = 4$ principal invariants relative to their $\ell = 0$ counterparts. For example, the 9 elements of $S^{(4)}$ are ~ 5 –10 times smaller than S_0 . Such decrease with ℓ is more pronounced in gray matter, and less so in crossing fibers or highly aligned white matter regions, e.g., the corpus callosum.

Invariants with $\ell > 0$ quantify the anisotropies of the irreducible components of C (while μFA does not characterize the anisotropy of any specific tensor). Is there a natural definition for an overall anisotropy measure of a higher-order tensor, analogous to FA for the 2nd-order tensor? Our approach suggests that each anisotropic irreducible component is characterized by its own independent invariants, such as S_2 and S_4 for the S tensor. Combining such invariants into a single metric seems arbitrary and mixes different symmetry sources. An example is the *kurtosis fractional anisotropy* (KFA)^{69,74}:

$$\text{KFA} \equiv \frac{\|S - S^{(0)}\|_F}{\|S\|_F} = \sqrt{\frac{14S_2^2 + 35S_4^2}{40S_0^2 + 14S_2^2 + 35S_4^2}}, \quad (31)$$

where we express the Frobenius norm $\|S\|_F^2 \equiv S_{ijkl}S_{ijkl} = \sum_\ell \zeta(4, \ell) S_\ell^2$ in terms of the principal invariants S_ℓ using Eq. (53). Akin to FA, KFA is bounded between 0 and 1. However, it seems equally reasonable to replace the Frobenius norm with the directional average $\overline{S^2(\hat{n})} = \sum_\ell S_\ell^2 / (2\ell + 1)$, yielding different relative weights with which the invariants S_ℓ would enter. As there is no “best” combination of invariants with different ℓ , it is generally logical to consider them separately.

There is a case where combining invariants with different ℓ is natural. The *axial and radial kurtoses*^{75,76} W_{\parallel} and W_{\perp} are projections of the kurtosis tensor $W = 3S/D_0^2$ [Eq. (12)] onto the principal fiber axis \hat{v} (the eigenvector for the largest eigenvalue of D), and transverse to it. In general, they are not rotational invariants inherent to W , as $W \propto S$ does not “know” about the tensor D and its eigenvectors. However, in voxels with a dominant fiber direction \hat{v} , microstructure aligns the S

and D tensors, Fig. 4, and axial/radial nomenclature becomes meaningful. Under an extra assumption of axial symmetry of S around \hat{v} , we express its projections via the principal invariants for $\ell = 0, 2, 4$:

$$D_{\parallel}^{\text{ax,sym}} = D_0 + D_2, \quad (32a)$$

$$D_{\perp}^{\text{ax,sym}} = D_0 - \frac{1}{2}D_2, \quad (32b)$$

$$W_{\parallel}^{\text{ax,sym}} = \frac{3}{D_0^2} (S_0 + S_2 + S_4), \quad (32c)$$

$$W_{\perp}^{\text{ax,sym}} = \frac{3}{D_0^2} \left(S_0 - \frac{1}{2}S_2 + \frac{3}{8}S_4 \right), \quad (32d)$$

without the need to transform to the eigenbasis of D. Indeed, in the basis with z-axis along \hat{v} , only $m = 0$ components are nonzero for each ℓ . This implies that $D_\ell = |D^{\ell 0}|$ and $S_\ell = |S^{\ell 0}|$. In this basis, $Y^{\ell 0}(\hat{z}) = 1$ for \parallel invariants; the average of $Y^{\ell 0}(\hat{n}) = P_\ell(\hat{n} \cdot \hat{z})$ around the equator for \perp invariants is given by Legendre polynomial values $P_2(0) = -\frac{1}{2}$ and $P_4(0) = \frac{3}{8}$.

How valid is the axial symmetry assumption? In Fig. 5b, we rotate all voxels' principal fiber axes \hat{n} to \hat{z} , and quantify the axial symmetry in each irreducible component $F^{(\ell)}$ via the ratios $|F_{\hat{n}}^{\ell 0}|/F_\ell$ of the $m = 0$ component to its principal invariant, the 2-norm $F_\ell = \|F^{\ell m}\|$ over all m . For the D tensor, the ratio $|D_{\hat{n}}^{20}|/D_2 = (1 + \eta_-^2/3\eta_+^2)^{-1/2}$ in the notations after Eq. (25). Perfect axial symmetry would correspond to the unit ratios. Fig. 5b shows that $D^{(2)}$ and $S^{(2)}$ have a high axial symmetry, while the opposite holds for $S^{(4)}$ and $A^{(2)}$.

Figures 5c and 5d show axial and radial projections for D and S: the exact ones calculated by projecting onto principal fiber direction \hat{v} and transverse to it, and the ones via assuming axial symmetry, Eqs. (32). Although $S^{(4)}$ is generally not axially symmetric, a good agreement between exact and approximate expressions is found in the whole brain because $S^{(4)}$ are much smaller than $S^{(0)}$ and $S^{(2)}$.

New invariants

The QT decomposition is motivated by the separation of different sources of covariances of compartmental diffusivities. While the $\ell = 0$ parts of T and Q have been studied in the dMRI literature under different names, their anisotropic complements (with $\ell > 0$) have remained largely unexplored. They provide access to novel rotationally invariant dMRI contrasts.

Overall, just 6 independent invariants: D_0 and D_2 ; S_0 and A_0 (equivalently, Q_0 and T_0); and S_2 and S_4 , are enough to synthesize all previously used model-independent dMRI contrasts up to $O(b^2)$. Since individual DTI eigenvalues may be used as contrasts, the total number of previously studied $O(b^2)$ invariants (explicitly or implicitly) is at most 3 from D ($D_0, D_2, D_{2|3}$), and at most 4 from C (A_0, S_0, S_2, S_4).

The remaining 14 invariants of the C tensor contain essentially unexplored information. Their definition, symmetries, and geometric meaning constitute the main results of the present comprehensive group theory-based approach. Just as an example, one can think of a novel physically motivated

contrast — the size-shape correlation coefficient

$$\text{SSC} \equiv \frac{\|\langle\langle D^{00} D^{2m} \rangle\rangle\|}{\sqrt{\langle\langle (D^{00})^2 \rangle\rangle \cdot \sum_m \langle\langle D^{2m} D^{2m*} \rangle\rangle}} = \frac{1}{2} \frac{Q_2}{\sqrt{5} Q_0 T_0} \quad (33)$$

that involves Q_2 and is normalized between 0 and 1, where $\text{SSC}=0$ for independent shapes and sizes and $\text{SSC}=1$ for a linear relationship. The $\ell = 2$ and $\ell = 4$ sectors of T have not been looked upon at all. The six mixed invariants relate to the underlying fiber tract geometry, quantifying correlations between eigenframes of different irreducible components. In particular, small relative angles $\tilde{\beta}$ in Fig. 4 within major white matter tracts are set by the underlying aligned fiber geometry.

Such a large set of complementary tissue contrasts is well suited for machine learning algorithms to study human development, aging and disease. Much like RGB pictures contain $N = 3$ colors, $N = 21$ invariant contrasts can be viewed as a large- N generalization of computer vision data, prompting the development of large- N classifiers.

A comprehensive B-tensor encoding human dataset has been recently made public⁷⁷, from which all SA and QT invariants can be determined and studied. For invariants not involving the A tensor, one can explore hundreds of thousands human data sets from imaging consortia such as the Alzheimer's Disease Neuroimaging Initiative (ADNI)⁴¹, Human Connectome Project⁴², UK Biobank⁴⁴, Adolescent Brain Cognitive Development (ABCD)⁴⁵, and Cambridge Centre for Ageing and Neuroscience data repository⁴⁶, which are all compatible with the DKI representation (11). Below we demonstrate the clinical relevance of the added information content from novel invariants in detecting neurodegeneration.

Multiple sclerosis classification based on clinical dMRI

We evaluated the clinical relevance of RICE invariants in a cohort of 1189 subjects that received a clinically dedicated brain MRI. This included 627 multiple sclerosis patients and 562 age- and sex-matched healthy controls. Two-shell LTE dMRI was acquired^{47,48}, see *Methods* for details. All clinical scans were retrospectively analyzed, and invariants were computed using DTI, DKI, and RICE_{LTE}. Logistic regression models were trained using all DTI–DKI–RICE_{LTE} invariants as predictors, where RICE_{LTE} contains all invariants of the kurtosis tensor $W \propto S$ in the SA decomposition of C. Due to LTE-only data, the A-tensor invariants were inaccesible.

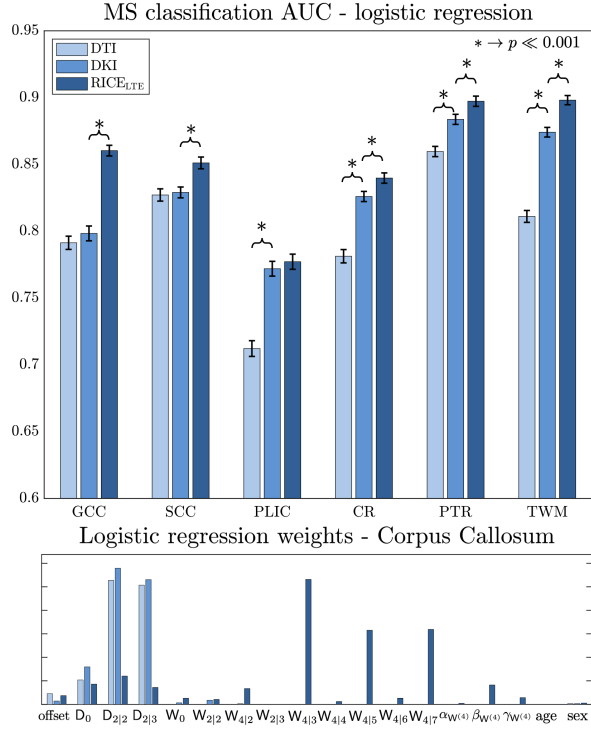


FIG. 6. Regression performance for classifying multiple sclerosis from controls based on median values across white matter regions (genu of corpus callosum, GCC; splenium of corpus callosum, SCC; Posterior limb of internal capsule, PLIC; Corona Radiata, CR; Posterior thalamic radiation, PTR; Total white matter, TWM). AUCs were averaged over 100 stratified bootstrap iterations for logistic regressions based on DTI, DKI, and RICE_{LTE} invariants on 238 test subjects ($p \ll 0.001$, denoted by *, error bars denote 95% confidence interval of the means). Regression weights averaged for the corpus callosum are displayed in the bottom plot.

Classification was evaluated with stratified bootstrap resampling (80% training, 20% testing), preserving group proportions and sex balance. This yielded a distribution of area under the ROC curve (AUC) values across iterations, providing a robust measure of model performance.

Figure 6 shows AUC values in six different white matter regions involved in multiple sclerosis, extracted from the Johns Hopkins University white matter atlas⁷⁸. DKI outperforms DTI, as expected due to a more informative dMRI acquisition (an extra LTE b -shell). Remarkably, up to a 30% reduction in pairwise ranking error (ranking loss, $1 - \text{AUC}$) is achieved via RICE_{LTE} invariants based on the same DKI acquisition, essentially for free, underscoring the nontrivial information content of the present approach. Regression weights highlight the importance of incorporating invariants beyond the conventional six, see *Previously used dMRI contrasts from RICE*.

This analysis demonstrates RICE invariants are not only mathematically independent but also biologically and clinically informative. Since these invariants were extracted retrospectively from standard 2-shell LTE acquisitions, with no extra data involved, the classification improvement represents pure gain in performance based on our symmetry-based approach. As our analysis was intentionally restricted to individ-

ual anatomical regions and summary statistics (median values within a small number of large ROIs), and employed simple logistic regression, the reported gains should be interpreted as a lower bound on potential information gain. Incorporating non-LTE data, yielding the asymmetric part A of the covariance tensor, is likely to further enhance RICE's classification performance.

Minimal protocols: iRICE

Clinical dMRI is constrained by scan time. A compromise could be to use a small number of measurements (much fewer than 1+6+21) to estimate just a few $\ell = 0$ invariants, given that they are most pronounced, Fig. 5a. The orthogonality of spherical harmonics ensures an unbiased estimation of any sector ℓ of spherical tensor components without having to estimate the entire set. Furthermore, arranging B-tensors into *spherical designs* provides the minimum number of directions that guarantee such orthogonality. These ideas result in the minimal iRICE (“instant RICE”) protocols, as described below.

We first note that since the axially symmetric family (9) couples to all components of C , without the loss of generality we can consider spherical designs on \mathbb{S}^2 rather than on the SO(3) manifold $\mathbb{S}^3/\mathbb{Z}_2$ of generic B-tensors. Next, we remind that a spherical L -design on \mathbb{S}^2 is a set of N_L points $\{\hat{\mathbf{g}}^\alpha \in \mathbb{S}^2\}_{\alpha=1}^{N_L}$ on a unit sphere, that satisfies⁸¹

$$\frac{1}{N_L} \sum_{\alpha=1}^{N_L} f^{(L)}(\hat{\mathbf{g}}^\alpha) \equiv \int_{\mathbb{S}^2} f^{(L)}(\hat{\mathbf{g}}) \frac{d\Omega_{\hat{\mathbf{g}}}}{4\pi} = f^{00} \quad (34)$$

for any degree- L function $f^{(L)}(\hat{\mathbf{g}})$, i.e., expressible as a spherical harmonics series up to degree L . In other words, any integration over \mathbb{S}^2 is exactly represented by a finite sum (34) for any rotation of the set $\{\hat{\mathbf{g}}^\alpha\}$, provided that the integrand is degree- L , and yields its angular average f^{00} . In particular, taking $f^{(L)}(\hat{\mathbf{g}}) = Y^{\ell m}(\hat{\mathbf{g}}) Y^{\ell' m'}(\hat{\mathbf{g}})$, the orthogonality of $Y^{\ell m}(\hat{\mathbf{g}})$ and $Y^{\ell' m'}(\hat{\mathbf{g}})$ is ensured exactly in the finite- N_L sums (34) for all $\ell + \ell' \leq L$. The smallest 2- and 4-designs are provided by tetrahedron and icosahedron vertices, $N_2 = 4$ and $N_4 = 12$, respectively. However, for antipodal-symmetric $f^{(L)}(\hat{\mathbf{n}}) = f^{(L)}(-\hat{\mathbf{n}})$ relevant for dMRI, $N_2 = 3$ reduces to half of the octahedron vertices, and $N_4 = 6$ to half of the icosahedron vertices, cf. Supplementary Section S5.

Constructing fixed- b shells (9) from 4-designs $\{\hat{\mathbf{g}}^\alpha\}$ allows us to become insensitive to $\ell = 4$ terms in Eq. (10) and fit

$$\begin{aligned} \ln \frac{\mathcal{S}(b, \hat{\mathbf{g}}^\alpha)}{\mathcal{S}|_{b=0}} = & -b \left(D_0 + \beta \sum_{m=-2}^2 D^{2m} Y^{2m}(\hat{\mathbf{g}}^\alpha) \right) \\ & + \frac{b^2}{2} \left(Q_0 + \beta^2 T_0 + \sum_{m=-2}^2 (\beta Q^{2m} + \beta^2 T^{2m}) Y^{2m}(\hat{\mathbf{g}}^\alpha) \right). \end{aligned} \quad (35)$$

We kept the $\ell = 2$ terms in Eq. (35), not just $\ell = 0$, because $N_4 = 6$ directions are enough to obtain unbiased D^{2m} estimates (and hence, DTI) at no extra cost. Unfortunately, the $O(b^2)$

TABLE I. Theoretically minimal protocols contain the minimum unique number of directions and distinct b -values (specific b -values can be altered). For STE, more than 1 direction implies rotation of the waveform for accuracy. All protocols include a $b = 0$ image to estimate $S|_{b=0}$.

Fast protocols comparison, b -values are in $\text{ms}/\mu\text{m}^2$		
Output maps	MD+MK	MD+FA+MK
Theoretical minimum	$6 \times \text{LTE}_{b=2}$ $1 \times \text{STE}_{b=1}$	$6 \times \text{LTE}_{b=1}; 6 \times \text{LTE}_{b=2}$
iRICE (MD+FA+MK)		$6 \times \text{LTE}_{b=1}; 6 \times \text{LTE}_{b=2}$
Ref. ^{69,79}	$3 \times \text{LTE}_{b=1}; 9 \times \text{LTE}_{b=2}$	$9 \times \text{LTE}_{b=1}; 9 \times \text{LTE}_{b=2}$
Output maps	MD+MK+ μ FA	MD+FA+MK+ μ FA
Theoretical minimum	$6 \times \text{LTE}_{b=2}$ $1 \times \text{STE}_{b=1}; 1 \times \text{STE}_{b=1.5}$	$6 \times \text{LTE}_{b=1}; 6 \times \text{LTE}_{b=2}$ $1 \times \text{STE}_{b=1.5}$
iRICE (MD+FA+MK+ μ FA)		$6 \times \text{LTE}_{b=1}; 6 \times \text{LTE}_{b=2}$ $3 \times \text{STE}_{b=1.5}$
Ref. ⁸⁰	$3 \times \text{LTE}_{b=0.1}; 3 \times \text{LTE}_{b=0.7}; 6 \times \text{LTE}_{b=1.4}; 6 \times \text{LTE}_{b=2}$ $6 \times \text{STE}_{b=0.1}; 6 \times \text{STE}_{b=0.7}; 10 \times \text{STE}_{b=1.4}; 16 \times \text{STE}_{b=2}$	

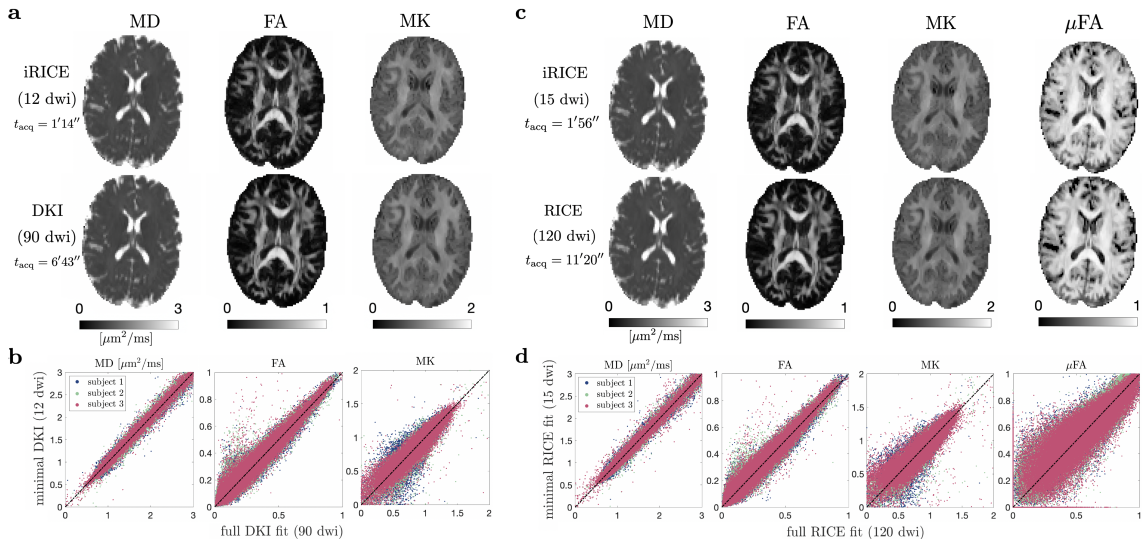


FIG. 7. Comparison of iRICE (1-2 minutes) with fully sampled acquisitions (6-11 minutes). (a,c): iRICE maps (top) vs fully sampled DKI maps (bottom) for a healthy volunteer. Panels (b) and (d) show scatter plots for all brain voxels in 3 normal volunteers (3 colors).

estimates of $\beta Q^{2m} + \beta^2 T^{2m}$ terms will be biased by the presence of T^{4m} , as the 4-design cannot detect these two as orthogonal.

Minimal 4-designs combined with required b and β contain fewer measurements than the total DOF in D and C. Thus, Eq. (35) provides a method for the fastest unbiased estimation of $D^{(0)}$, $D^{(2)}$, $T^{(0)}$, and $Q^{(0)}$ components, and the invariants (27)–(30). Table I shows the proposed minimal iRICE protocols for MD, FA, MK, based on measurements with 12 B tensors; and MD, FA, MK, μ FA with 15 B tensors. These numbers are notably smaller than $21 = 6 + 15$ or $27 = 6 + 21$ that were thought needed to simultaneously estimate all DOF (besides $S|_{b=0}$). While short acquisitions focused on just a few invariants have been developed^{69,79}, the present formulation allows for shorter and fully optimal protocols. In the 1-3-9 scheme of Ref.⁶⁹, MD is estimated from the lower- b shell assuming no $\sim b^2$ contributions, which may lead to spatially varying biases, while the 1-9-9 scheme of Ref.⁷⁹ uses approximately 50% more measurements than the minimum 1-

6-6 required, Table I. Our comprehensive approach based on spherical designs identifies protocols that require fewer measurements (Table I) while guaranteeing that these are, in fact, the shortest possible for a given cumulant order.

Minimal and extensive acquisitions are compared in Figs. 7a,c. iRICE maps show a near-identical contrast, even in regions with large $S^{(4)}$ such as WM fiber crossings, despite having 8-fold fewer measurements and not estimating full tensors. Scatter plots, Figs. 7b,d, do not show biases.

Generalization to time-dependent cumulants

Consider now the general case of time-dependent non-Gaussian diffusion in at least some of the compartments, characterized by the time-dependent diffusion and kurtosis tensors $D(t)$ and $S(t)$, as discussed around Eq. (20), with a voxel represented by the probability distribution func-

tional $\mathcal{P}[D(t), S(t)]$. To isolate physically distinct time-dependent $O(b^2)$ contributions, one can use double diffusion encoding^{20,25,26}. DDE consists of two diffusion encoding blocks with diffusion times $t_{1,2}$, weightings $b_{1,2}$, and directions $\hat{\mathbf{g}}_{1,2}$, separated by the mixing time t_m . In the limit $t_m \rightarrow \infty$, with $t_1 = t_2 \equiv t$, analogously to Eqs. (10)–(11), the logarithm \mathcal{L}_{DDE} of a voxel-wise DDE signal up to $O(b^2)$ reads²⁵

$$\begin{aligned} \mathcal{L}_{\text{DDE}} &= \ln \left\langle e^{-b_1 D(t, \hat{\mathbf{g}}_1) - b_2 D(t, \hat{\mathbf{g}}_2) + \frac{1}{2} b_1^2 S(t, \hat{\mathbf{g}}_1) + \frac{1}{2} b_2^2 S(t, \hat{\mathbf{g}}_2)} \right\rangle \\ &\simeq -b_1 D(t, \hat{\mathbf{g}}_1) - b_2 D(t, \hat{\mathbf{g}}_2) + \frac{1}{2} b_1^2 S_\mu(t, \hat{\mathbf{g}}_1) \\ &\quad + \frac{1}{2} b_2^2 S_\mu(t, \hat{\mathbf{g}}_2) + \frac{1}{2} b_1^2 \langle\langle D^2(t, \hat{\mathbf{g}}_1) \rangle\rangle \\ &\quad + \frac{1}{2} b_2^2 \langle\langle D^2(t, \hat{\mathbf{g}}_2) \rangle\rangle + b_1 b_2 \langle\langle D(t, \hat{\mathbf{g}}_1) D(t, \hat{\mathbf{g}}_2) \rangle\rangle \end{aligned} \quad (36)$$

where $\langle\langle D(t, \hat{\mathbf{g}}_1) D(t, \hat{\mathbf{g}}_2) \rangle\rangle = C_{ijkl}(t) g_{1i} g_{1j} g_{2k} g_{2l}$, and the overall microscopic kurtosis $S_\mu(t)$, Eq. (21), can now be disentangled^{25,26} from the $C(t)$ -tensor, in contrast to Eq. (20).

To equally probe all orientations, the signal (36) for a given DDE pair $(b_1, \hat{\mathbf{g}}_1; b_2, \hat{\mathbf{g}}_2)$ should be isotropically sampled across all rotations of this pair, keeping the angle ψ between $\hat{\mathbf{g}}_1$ and $\hat{\mathbf{g}}_2$ fixed.⁸² Akin to the discussion before Eq. (10), the corresponding DDE “shell” is the $\text{SO}(3)$ group manifold $\mathbb{S}^3/\mathbb{Z}_2$. The extra dimension relative to the 2-dimensional LTE shell \mathbb{S}^2 enables the estimation of all irreducible t -dependent components of Eq. (36). One way to do so is consider its spherical harmonic expansion with respect to $\hat{\mathbf{g}}_1$ while sampling the DDE shell, equivalent to the integral over $\text{SO}(3) \cong \mathbb{S}^3/\mathbb{Z}_2$

$$\mathcal{L}_{\text{DDE}}^{\ell m} = (2\ell + 1) \int_{\text{SO}(3)} d\mathcal{R} Y^{\ell m*}(\mathcal{R}\hat{\mathbf{g}}_1) \mathcal{L}_{\text{DDE}}(\mathcal{R}\hat{\mathbf{g}}_1, \mathcal{R}\hat{\mathbf{g}}_2) \quad (37)$$

with canonical measure normalized to $\int_{\text{SO}(3)} d\mathcal{R} \equiv 1$. In Supplementary Section S8 we derive $\text{SO}(3)$ Fourier coefficients of $\mathcal{L}_{\text{DDE}}(\mathcal{R}\hat{\mathbf{g}}_1, \mathcal{R}\hat{\mathbf{g}}_2)$, and the spherical harmonics (37):

$$\begin{aligned} \mathcal{L}_{\text{DDE}}^{00} &= -(b_1 + b_2) D^{00}(t) + \frac{1}{2} (b_1^2 + b_2^2) S_\mu^{00}(t) \\ &\quad + \frac{1}{2} (b_1 + b_2)^2 Q^{00}(t) + \frac{1}{2} (b_1^2 + b_2^2 + 2p_2 b_1 b_2) T^{00}(t), \\ \mathcal{L}_{\text{DDE}}^{2m} &= -(b_1 + p_2 b_2) D^{2m}(t) + \frac{1}{2} (b_1^2 + p_2 b_2^2) S_\mu^{2m}(t) \\ &\quad + \frac{1}{2} (b_1^2 + p_2 b_2^2 + (1 + p_2) b_1 b_2) Q^{2m}(t) \\ &\quad + \frac{1}{2} (b_1^2 + p_2 b_2^2 + 2p_2 b_1 b_2) T^{2m}(t), \\ \mathcal{L}_{\text{DDE}}^{4m} &= \frac{1}{2} (b_1^2 + p_4 b_2^2) S_\mu^{4m}(t) \\ &\quad + \frac{1}{2} (b_1^2 + p_4 b_2^2 + 2p_2 b_1 b_2) T^{4m}(t), \end{aligned} \quad (38)$$

where $p_\ell(\psi) \equiv P_\ell(\hat{\mathbf{g}}_1 \cdot \hat{\mathbf{g}}_2)$ are Legendre polynomials. The components $Q^{\ell m}(t)$ and $T^{\ell m}(t)$ of $Q(t)$ and $T(t)$ are defined via the covariances $\langle\langle D^{\ell_1 m_1}(t) D^{\ell_2 m_2}(t) \rangle\rangle$ in Eqs. (8), while $S_\mu(t) = S_\mu^{(0)}(t) \oplus S_\mu^{(2)}(t) \oplus S_\mu^{(4)}(t)$ is the decomposition of the overall microscopic t -dependent kurtosis, akin to Eq. (13).

$\mathcal{L}_{\text{DDE}}^{00}$ is related to the spherical mean of the DDE signal²⁶; it serves as the basis of correlation tensor imaging yielding the mean microscopic kurtosis $S_\mu^{00}(t)$. Remarkably, the

anisotropic components $\mathcal{L}_{\text{DDE}}^{2m}$ and $\mathcal{L}_{\text{DDE}}^{4m}$ enable the estimation of all t -dependent spherical tensor components of the diffusion, covariance and microscopic kurtosis tensors. While the $\cos 2\psi$ DDE modulation coming from $p_2(\psi)$ has been observed⁸³, the unexpected 4-fold $\cos 4\psi$ modulation emerges from the $\ell = 4$ sector via $p_4(\psi)$.⁸⁴

The microscopic kurtosis tensor $S_\mu(t)$ has its own 15 DOF and 12 invariants: $1 + 2 + 6 = 9$ intrinsic and 3 mixed (angles between the $S_\mu^{(2)}$ and $S_\mu^{(4)}$ frames), similar to the invariants of S tensor in *Invariants: intrinsic and mixed* section.

DISCUSSION

It may be only a slight exaggeration to say that modern physics is the study of symmetry. Here we uncovered how the fundamental $\text{SO}(3)$ symmetry of our 3-dimensional world constrains the geometry and the degrees of freedom in the diffusion MRI cumulant series. The representation theory approach is so general that it applies for both Gaussian and non-Gaussian diffusion in the individual compartments. While the coarse-graining by diffusion^{8,10} within each compartment results in a particular time-dependence of its cumulants $D(t)$ and $S(t)$, the $\text{SO}(3)$ symmetry defines the structure of the irreducible components of the voxel-wise cumulant tensors. We can think of the symmetry providing a “non-negotiable” tensor structure within which the plethora of time-dependent diffusion effects occurs based on the coarse-graining over the compartment-specific microstructure. Based only on symmetry considerations, the formalism readily extends onto all 4th-order tensors with minor and major symmetries such as the elasticity tensor in continuous media^{49–52}, yielding applications in mechanics, geology, materials science, and soft condensed matter physics.

Can a non-Gaussian compartment be made of “more elementary” Gaussian ones in the spirit of Eqs. (1)–(2)? If this were true, we could without the loss of generality build our formalism based on $\mathcal{P}(D)$ for the Gaussian compartments. In general, the answer is no: Coarse-graining of the microstructure by diffusion generally leads to *time-dependent* cumulants in a given compartment. $D(t)$ monotonically decreases towards a constant tensor, and $S(t)$ and higher-order cumulants vanish as $t \rightarrow \infty$.⁸⁵ Hence, the picture of Eqs. (1)–(2) is valid at sufficiently long times, when the transient coarse-graining processes become negligible, $C(t) \rightarrow C = \text{const}$, and $S_\mu \rightarrow 0$. Exchanging compartments^{26,61,86} can be viewed as a single non-Gaussian one with time-dependent $S(t)$ that vanishes as $t \rightarrow \infty$, contributing to the overall $S_\mu(t)$ at finite t .

While the present framework is model-independent and general, our main limitation has been working up to $O(b^2)$. However, this is not a limitation of the symmetry-based approach, which can be extended to higher-order cumulant tensors. For example, the next, 6th-order cumulant at $O(b^3)$ maps onto the addition of 3 angular momenta of $\ell = 0$ or 2 (for the Gaussian compartments). The generalization of QT decomposition would yield the covariances $\langle\langle D^{\ell m} D^{\ell' m'} D^{\ell'' m''} \rangle\rangle$, which split into the irreducible decomposition

$$\text{Sym} \left[(V_0 \oplus V_2)^{\otimes 3} \right] \cong V_6 \oplus 2V_4 \oplus 4V_2 \oplus 5V_0 \quad (39)$$

with the multiplicities as indicated, totaling 56 DOF, of which 35 are intrinsic and 18 mixed invariants. The corresponding SA decomposition gives $V_6 \oplus V_4 \oplus V_2 \oplus V_0$ for the fully symmetric part, and $V_4 \oplus 3V_2 \oplus 4V_0$ for the remaining asymmetric part, each carrying 28 DOF. Probing all 56 DOF of $\langle\langle D \otimes D \otimes D \rangle\rangle$ requires non-axially symmetric B tensors⁸⁷. In other words, this and higher-order cumulants involve waveform rotations over the $SO(3)$ manifold $\mathbb{S}^3/\mathbb{Z}_2$ rather than \mathbb{S}^2 , increasing scan time substantially.

The cumulant expansion provides a powerful model-independent description of the dMRI signal within its convergence radius b_* that depends on the microstructure in a given sample (voxel).⁸⁸ When the acquisition range $0 \leq b \leq b_{\max}$ is within the convergence radius, $b_{\max} < b_*$, adding the successive terms increases the accuracy of the cumulant tensors' estimation (at a cost of the loss of precision); the truncation at a given order is justified when the neglected contributions remain below the noise floor. When valid, symmetry-based irreducible representations of the cumulant tensors provide maximally informative and mutually orthogonal decompositions at each order. For $b \geq b_*$, the series diverges; hence, for protocols with $b_{\max} \geq b_*$, adding extra terms can uncontrollably modify the estimates for the lower-order ones^{89,90}. The signal's description in terms of the power series then ceases to be useful since the estimates depend on the range b_{\max} rather than on tissue properties, and a full functional form of $\mathcal{P}(D, \dots)$ should rather be employed. The latter has been performed using a multi-dimensional inverse Laplace transform^{22,91,92} assuming Gaussian compartments, which requires regularization or constraints, and uses extensive, so-far clinically unfeasible acquisitions.

Practically, for diffusion NMR/MRI, we uncovered 14 invariants in addition to 7 previously used in the life sciences context of diagnostic MRI. Publicly available consortia dMRI datasets provide a venue to study the novel contrasts at a population level. Our results show that for conventional multi-shell dMRI (LTE-only), the information added by the RICE invariants for the kurtosis tensor improves multiple sclerosis detection. RICE maps belong to distinct irreducible representations of rotations, and thereby represent “orthogonal” contrasts up to b^2 . Such independence may improve sensitivity and specificity to detect specific tissue microstructure changes in disease, aging and development. Furthermore, the proposed minimal iRICE acquisition protocols for estimating MD, FA, MK, and μ FA will enable clinical translation of beyond-DTI diffusion metrics hampered by long scan times.

METHODS

Notations

Throughout this work, sans serif font refers to voxel-wise tensors, such as D , C , A , S , Q , T , whereas italic font refers to tensors D of the microscopic compartments. These may have either Cartesian components such as D_{ij} and D_{ij} , or spherical tensor components such as $D^{\ell m}$ and $D^{\ell m}$. We refer to irreducible components, such as $S^{(\ell)}$, both as a collection of $S^{\ell m}$ spherical tensor elements, or Cartesian ones $S_{i_1 \dots i_\ell}^{(\ell)}$. Unless specified otherwise, the order ℓ of the latter will coincide with the number of Cartesian subindices since this is the most natural representation. We assume Einstein's convention of summation over repeated Cartesian subindices $ijkl\dots$.

Brackets $\langle \dots \rangle$ denote averages over the compartmental diffusion tensor distribution $\mathcal{P}(D)$, and double brackets $\langle\langle \dots \rangle\rangle$ denote the cumulants of $\mathcal{P}(D)$. Finally, for readability, given the plethora of conventional superscript indices $^{(\ell)}$ for irreducible tensor components, we omit outer parentheses when referring to tensor traces, e.g., $\text{tr } B = \text{tr}(B)$, $\text{tr } BD = \text{tr}(BD)$, $\text{tr}(D^{(2)})^3 = \text{tr}((D^{(2)})^3)$, and $\text{tr}^\nu B = (\text{tr}(B))^\nu$.

Multiple Gaussian compartments

The dMRI signal from a given voxel

$$\mathcal{S} = \langle e^{i\phi} \rangle_{\text{paths+spins}}, \quad \phi = - \int_0^t d\tau \mathbf{g}(\tau) \cdot \mathbf{r}(\tau) \quad (40)$$

is the transverse magnetization $e^{i\phi}$ in the rotating frame, averaged over all spins traveling along all possible Brownian paths $\mathbf{r}(\tau)$ between $\tau = 0$ and measurement time t . Experiments are performed under the condition $\int_0^t \mathbf{g}(\tau) d\tau = 0$ on the applied Larmor frequency gradient $\mathbf{g}(\tau)$ ^{2,8,17}. In general, the dMRI signal is a functional of $\mathbf{g}(t)$, or, equivalently, of the encoding function $\mathbf{q}(t) = \int_0^t \mathbf{g}(\tau) d\tau$: $\mathcal{S} = \mathcal{S}[\mathbf{q}(t)]$. Even for a conventional pulsed-gradient (LTE) diffusion sequence⁵⁷, one obtains a multi-dimensional phase diagram in the space of sequence parameters^{10,93,94}.

However, after coarse-graining the dynamics within a given tissue compartment over sufficiently long t , the microstructure-induced temporal velocity correlations become forgotten, such that the distribution of spin phase $\phi = \int_0^t d\tau \mathbf{q}(\tau) \mathbf{v}(\tau)$ becomes asymptotically Gaussian, defined by its velocity autocorrelation function $\langle\langle v_i(\tau) v_j(\tau') \rangle\rangle \simeq 2D_{ij} \delta(\tau - \tau')$ ^{8,10,17}. The averaging in Eq. (40) over a compartment is then represented in terms of the second cumulant of the phase, $\mathcal{S} = e^{-B_{ij} D_{ij}}$, and the measurement is determined by specifying the B-tensor

$$B_{ij} = \int_0^t d\tau q_i(\tau) q_j(\tau) \quad (41)$$

calculated based on $\mathbf{q}(t)$. The distribution $\mathcal{P}(D)$ of compartment tensors in a voxel gives rise to the overall signal⁹⁵⁻⁹⁷

$$\mathcal{S}(B) = \int dD \mathcal{P}(D) e^{-\text{tr } BD} = \sum_\alpha f_\alpha e^{-\text{tr } BD^\alpha}. \quad (42)$$

Normalization $\int dD \mathcal{P}(D) = 1$ implies $\sum_\alpha f_\alpha = 1$.

Equation (42) is the most general form of a signal from multiple Gaussian compartments. It is valid when the transient processes have played out, such that compartmental diffusion tensors D have all become time-independent, and thereby higher-order cumulants in each compartment are negligible⁸. In this case, the signal (42) is a function of the B-tensor: $\mathcal{S}[\mathbf{q}(t)] \rightarrow \mathcal{S}(B)$, while tissue is fully represented by the voxel-wise distribution $\mathcal{P}(D)$. This long- t picture of multiple Gaussian compartments (anisotropic and non-exchanging) underpins a large number of dMRI modeling approaches, in particular, the Standard Model (SM) of diffusion⁸ and its variants⁹⁸⁻¹⁰³. Furthermore, this picture contains the SM extension onto different fiber populations in a voxel, lifting the key SM assumption of a single-fascicle “kernel” (response).

Given the forward model (42), an inverse problem is to restore $\mathcal{P}(D)$ from measurements with different B. This problem is a matrix version of the inverse Laplace transform and is therefore ill-conditioned. Since in clinical settings, typical encodings are moderate ($\text{tr } BD \sim 1$), the inverse problem can be formulated term-by-term for the cumulant expansion (1) of the signal (42).

The cumulant series for multiple Gaussian compartments

The higher-order signal terms in Eq. (1) couple to successive cumulants of $\mathcal{P}(D)$. The inverse problem maps onto finding the cumulants $\langle\langle D_{i_1 j_1} \dots D_{i_n j_n} \rangle\rangle$ (tensors of even order $2n$) from a set of measurements. This becomes obvious by noting the analogy $B \rightarrow i\lambda$ with the standard cumulant series²³ $\ln p(\lambda) = \sum_{n=1}^{\infty} \frac{(-i\lambda)^n}{n!} \langle\langle x^n \rangle\rangle$ for the characteristic function $p(\lambda) = \int dx e^{-i\lambda x} p(x)$ of a probability distribution $p(x)$, such that the n -th term in Eq. (1) is $\frac{(-1)^n}{n!} B_{i_1 j_1} \dots B_{i_n j_n} \langle\langle D_{i_1 j_1} \dots D_{i_n j_n} \rangle\rangle$.

Hence, the introduction of the B-tensor, enabled by the Gaussian diffusion assumption in every compartment, lowers the order by half: The $2n$ -th cumulant of the phase (40) [i.e., the $2n$ -th order term of expanding $\ln \mathcal{S}[\mathbf{q}(t)]$ in $\mathbf{q}(t)$] maps onto the n -th cumulant $\langle\langle D_{i_1 j_1} \dots D_{i_n j_n} \rangle\rangle$ of $\mathcal{P}(D)$ corresponding to the n -th order of expansion of $\ln \mathcal{S}(B)$ in B. The number of DOF for this cumulant equals to that for a fully symmetric order- n tensor of dimension $d = 6$, which is a number of assignments of n indistinguishable objects into d distinguishable bins: $\binom{n+d-1}{n} = (n+5)!/(n! \cdot 5!) = 6, 21, 56, 126, \dots$ for $n = 1, 2, 3, 4, \dots$

The range of diffusion weightings used in this work ensures the sensitivity to $\mathcal{O}(b^2)$ signal components, necessary for estimating C in the living human brain. While it is not required to replicate our exact diffusion weightings to estimate the cumulants, the maximal b should be high enough to capture $\mathcal{O}(b^2)$ contributions, yet low enough to keep higher-order terms small. Extending b beyond the convergence radius of the cumulant expansion⁸⁸ will diminish the accuracy^{89,90}. For *in vivo* brain dMRI, we recommend $b \lesssim 2 - 3 \text{ ms}/\mu\text{m}^2$.

Irreducible representations of SO(3)

Here we remind key aspects from representation theory of SO(3)^{54,55} used throughout this work. A d -dimensional representation of a group is a mapping of each element (rotation) onto a $d \times d$ matrix that acts on a d -dimensional vector space. Representation theory provides a way to split a complex object (such as tensor D or C) into a set of independent simpler ones with certain symmetries, on which a group acts. In particular, the elements of an *irreducible representation* transform among themselves, and hence can be studied separately.

Every irreducible representation of SO(3) is labeled by an integer *degree* $\ell = 0, 1, 2, \dots$, and acts on a $2\ell + 1$ -dimensional space of STF tensors⁵³ — fully symmetric and trace-free (for $\ell > 0$) tensors of *order* ℓ (i.e., with ℓ indices). Any order- ℓ STF tensor (STF- ℓ tensor) can be represented by its $2\ell + 1$ *spherical tensor* components $F^{\ell m}$, $m = -\ell \dots \ell$:

$$F_{i_1 \dots i_\ell}^{(\ell)} = \sum_{m=-\ell}^{\ell} F^{\ell m} \mathcal{Y}_{i_1 \dots i_\ell}^{\ell m}, \quad (43)$$

where $\mathcal{Y}_{i_1 \dots i_\ell}^{\ell m}$ form the standard complex-valued STF basis⁵³. STF property means that a trace over any pair of indices vanishes for $\ell \geq 2$: $\mathcal{Y}_{i_1 \dots i_\ell}^{\ell m} \delta_{i_n i_{n'}} \equiv 0$, $1 \leq n, n' \leq \ell$. The case $\ell = 0$ corresponds to a (generally nonzero) scalar. For each ℓ , basis STF tensors generate $2\ell + 1$ spherical harmonics on \mathbb{S}^2 :

$$Y^{\ell m}(\hat{\mathbf{n}}) = \mathcal{Y}_{i_1 \dots i_\ell}^{\ell m} n_{i_1} \dots n_{i_\ell}, \quad |\hat{\mathbf{n}}| = 1. \quad (44)$$

As a result, a spherical tensor is uniquely mapped onto a “glyph” (e.g., Fig. 2):

$$F_{i_1 \dots i_\ell}^{(\ell)} = F_{i_1 \dots i_\ell}^{(\ell)} n_{i_1} \dots n_{i_\ell} = \sum_{m=-\ell}^{\ell} F^{\ell m} Y^{\ell m}(\hat{\mathbf{n}}), \quad (45)$$

with its components $F^{\ell m}$ being spherical harmonics coefficients of the glyph.

Throughout this work, we use *Racah normalization*¹⁰⁴ of spherical harmonics and spherical tensors (* denotes complex conjugation):

$$\int_{\mathbb{S}^2} d\Omega_{\hat{\mathbf{n}}} Y^{\ell m *}(\hat{\mathbf{n}}) Y^{\ell' m'}(\hat{\mathbf{n}}) = \frac{4\pi}{2\ell + 1} \delta_{\ell \ell'} \delta_{mm'}. \quad (46)$$

To obtain Racah-normalized spherical harmonics and basis tensors $\mathcal{Y}_{i_1 \dots i_\ell}^{\ell m}$, one needs to multiply the orthonormal $Y^{\ell m}(\hat{\mathbf{n}})$ and $\mathcal{Y}_{i_1 \dots i_\ell}^{\ell m}$ (found, e.g., in Thorne⁵³) by $\sqrt{4\pi/(2\ell + 1)}$. Thus, Racah-normalized spherical tensor coefficients $F^{\ell m}$ do not carry the $\sqrt{(2\ell + 1)/4\pi}$ factors ubiquitous for the orthonormal spherical harmonics. This has a benefit of the $\ell = 0$ component being identically equal to the angular-averaged glyph since $\mathcal{Y}^{00} \equiv 1$ (see, e.g., Eq. (5) for mean diffusivity), as well as of simplifying the relations between the spherical harmonics products and Clebsch-Gordan coefficients, see Supplementary Section S2. We also use Condon-Shortley convention¹⁰⁵

$$\mathcal{Y}_{i_1 \dots i_\ell}^{\ell m *} = (-1)^m \mathcal{Y}_{i_1 \dots i_\ell}^{\ell, -m}(\hat{\mathbf{n}}), \quad Y^{\ell m *}(\hat{\mathbf{n}}) = (-1)^m Y^{\ell, -m}(\hat{\mathbf{n}}), \quad (47)$$

and thus $F^{\ell m *} = (-1)^m F^{\ell, -m}$ for real-valued $F_{i_1 \dots i_\ell}^{(\ell)}$.

To go from Cartesian to spherical tensor components, we invert Eq. (43) via Eq. (2.5) of Ref⁵³, Eqs. (44) and (46):

$$\mathcal{Y}_{i_1 \dots i_\ell}^{\ell m *} \mathcal{Y}_{i_1 \dots i_\ell}^{\ell m'} = \frac{(2\ell - 1)!!}{\ell!} \delta_{mm'}, \quad (48)$$

where $\ell!! \equiv \ell(\ell - 2)(\ell - 4) \dots (2 \text{ or } 1)$, such that

$$F^{\ell m} = \frac{\ell!}{(2\ell - 1)!!} \mathcal{Y}_{i_1 \dots i_\ell}^{\ell m *} F_{i_1 \dots i_\ell}. \quad (49)$$

Decomposition into irreducible representations

Any fully symmetric order- L tensor $F_{i_1 \dots i_L}$ (generally, with nonzero traces), such as the kurtosis tensor (13), can be decomposed into a direct sum of STF tensors $F = F^{(L)} \oplus F^{(L-2)} \oplus \dots$ of degrees $L, L - 2, \dots, (0 \text{ or } 1)$, effectively by subtracting traces⁵³. To convert this direct sum into an ordinary sum in the space of order- L tensor components

$$F_{i_1 \dots i_L} = \sum_{\ell=L, L-2, \dots} F_{i_1 \dots i_L}^{(\ell)}, \quad F_{i_1 \dots i_L}^{(\ell)} = \sum_{m=-\ell}^{\ell} F^{\ell m} \mathcal{Y}_{i_1 \dots i_L}^{\ell m}, \quad (50)$$

we introduce the basis elements that are *non-STF* for $L > \ell$:

$$\mathcal{Y}_{i_1 \dots i_L}^{\ell m} = \mathcal{Y}_{i_1 \dots i_\ell}^{\ell m} \delta_{i_{\ell+1} i_{\ell+2}} \dots \delta_{i_{L-1} i_L}, \quad \ell \leq L, \quad (51)$$

through symmetrization of the STF- ℓ basis elements with the remaining $(L - \ell)/2$ Kronecker symbols, naturally generalizing Eqs. (44)–(45):

$$F^{(\ell)}(\hat{\mathbf{n}}) = F_{i_1 \dots i_L}^{(\ell)} n_{i_1} \dots n_{i_L} = \sum_{m=-\ell}^{\ell} F^{\ell m} Y^{\ell m}(\hat{\mathbf{n}}). \quad (52)$$

The basis (51) of order- L symmetric tensors is orthogonal with respect to taking the trace over all L indices.

To find all spherical tensor components $F^{\ell m}$ for $\ell = L, L - 2, \dots$ of a fully symmetric order- L Cartesian tensor according to Eq. (50), in Supplementary Section S1 we generalize the normalization (48) for $L > \ell$:

$$\mathcal{Y}_{i_1 \dots i_L}^{\ell m *} \mathcal{Y}_{i_1 \dots i_L}^{\ell m'} = \zeta(L, \ell) \delta_{\ell \ell'} \delta_{mm'}, \quad \zeta(L, \ell) = \frac{(L + \ell + 1)!!(L - \ell)!!}{L!(2\ell + 1)}, \quad (53)$$

such that $\zeta(\ell, \ell) = (2\ell - 1)!!/\ell!$ matches Eq. (48), yielding

$$F^{\ell m} = \frac{1}{\zeta(L, \ell)} \mathcal{Y}_{i_1 \dots i_\ell}^{\ell m *} \delta_{i_{\ell+1} i_{\ell+2}} \dots \delta_{i_{L-1} i_L} F_{i_1 \dots i_L}. \quad (54)$$

In other words, the degree- ℓ spherical tensor components $F^{\ell m}$ in the decomposition (50) are obtained by taking the remaining $(L - \ell)/2$ traces and convolving with the standard STF- ℓ basis element $\mathcal{Y}_{i_1 \dots i_\ell}^{\ell m *}$, albeit using the normalization coefficient $1/\zeta(L, \ell)$ that “remembers” the original $L > \ell$.

So far, our discussion of $\text{SO}(3)$ representations has been completely general. In dMRI context, every degree ℓ is even due to time-reversal invariance of the Brownian motion, dictating even parity $Y^{\ell m}(-\hat{\mathbf{n}}) = Y^{\ell m}(\hat{\mathbf{n}})$. Hence, each cumulant or moment tensor, as in Eq. (1), can be split into a direct sum of irreducible representations with even ℓ in Eq. (50), connecting it with the orientation dispersion in the spherical harmonics basis^{35,106}.

Applying the above methodology to the \mathbf{C} tensor, we first split it into \mathbf{S} and \mathbf{A} , Eq. (12)–(14). To decompose \mathbf{A} , we use Eqs. (15), where Eq. (15a) is $\mathbf{A}_{pq} = 4\Delta_{pq}$ from Eqs. (45)–(46) in⁶²; here we use the same symbol \mathbf{A} for 2nd and 4th order tensors, as they are isomorphic (and represent the same geometric object). Eq. (15b) is obtained by using the identity $\epsilon_{ijk}\epsilon_{lmn} = \delta_{il}\delta_{jm}\delta_{kn} + \delta_{im}\delta_{jn}\delta_{kl} + \delta_{in}\delta_{jl}\delta_{km} - \delta_{il}\delta_{jn}\delta_{km} - \delta_{in}\delta_{jm}\delta_{kl} - \delta_{im}\delta_{jl}\delta_{kn}$. Eq. (15c) (the inverse relation) follows from $\epsilon_{ijm}\epsilon_{kln} = \delta_{ik}\delta_{jl} - \delta_{il}\delta_{jk}$ and from the property $\mathbf{A}_{i(jkl)} \equiv 0$ that is a consequence of Eq. (14).

Now that all Cartesian tensors \mathbf{S}_{ijkl} and \mathbf{A}_{pq} derived from \mathbf{C} are fully symmetric, we can represent them as combinations of spherical tensors, cf. Eq. (50). Applying Eq. (54), we get

$$\begin{aligned} \mathbf{D}^{00} &= \frac{1}{3}\mathbf{D}_{ii} & \mathbf{D}^{2m} &= \frac{2}{3}\mathbf{Y}_{ij}^{2m*}\mathbf{D}_{ij}; \\ \mathbf{A}^{00} &= \frac{1}{3}\mathbf{A}_{ii}, & \mathbf{A}^{2m} &= \frac{2}{3}\mathbf{Y}_{ij}^{2m*}\mathbf{A}_{ij}; \\ \mathbf{S}^{00} &= \frac{1}{5}\mathbf{S}_{iijj}, & \mathbf{S}^{2m} &= \frac{4}{7}\mathbf{Y}_{ij}^{2m*}\mathbf{S}_{ijkk}, \\ & & \mathbf{S}^{4m} &= \frac{8}{35}\mathbf{Y}_{ijkl}^{4m*}\mathbf{S}_{ijkl}. \end{aligned} \quad (55)$$

Eqs. (18) then relate the components (55) to those of \mathbf{Q} and \mathbf{T} .

From tissue diffusivities to QT decomposition

We derived Eqs. (18) using a shortcut that happens to work for the \mathbf{C} tensor: the special \mathbf{B} -tensor family (9) allowed us to match the spherical harmonics components (10) with those of Eqs. (17). It turns out that for higher-order tensors (arising at the $O(b^3)$ level and beyond), the axially-symmetric family (9) does not probe all their DOF. Hence, below we provide a more generalizable way to derive Eqs. (18) by explicitly following the components (55) through triple products of spherical harmonics and the corresponding Clebsch-Gordan coefficients. This highlights the connection between the compartmental diffusion tensor covariances and the addition of angular momenta (cf. Supplementary Section S2).

We begin from the irreducible decomposition of compartmental diffusion tensors (3), this can be used to explicitly write \mathbf{D} and \mathbf{C} , Eqs. (2):

$$\begin{aligned} \mathbf{D}_{ij} &= \langle \mathbf{D}^{00} \rangle \delta_{ij} + \sum_m \langle \mathbf{D}^{2m} \rangle \mathbf{Y}_{ij}^{2m}, \\ \mathbf{C}_{ijkl} &= \langle \langle (\mathbf{D}^{00})^2 \rangle \rangle \delta_{ij}\delta_{kl} + \sum_{m,m'} \langle \langle \mathbf{D}^{2m}\mathbf{D}^{2m'} \rangle \rangle \mathbf{Y}_{ij}^{2m}\mathbf{Y}_{kl}^{2m'} \\ &\quad + \sum_m \langle \langle \mathbf{D}^{00}\mathbf{D}^{2m} \rangle \rangle \left(\delta_{ij}\mathbf{Y}_{kl}^{2m} + \mathbf{Y}_{ij}^{2m}\delta_{kl} \right). \end{aligned} \quad (56)$$

The SA decomposition of \mathbf{C} , Eqs. (12)–(14), yields

$$\begin{aligned} \mathbf{S}_{ijkl} &= \langle \langle (\mathbf{D}^{00})^2 \rangle \rangle \delta_{(ij}\delta_{kl)} + 2\sum_m \langle \langle \mathbf{D}^{00}\mathbf{D}^{2m} \rangle \rangle \delta_{(ij}\mathbf{Y}_{kl)}^{2m} \\ &\quad + \sum_{m,m'} \langle \langle \mathbf{D}^{2m}\mathbf{D}^{2m'} \rangle \rangle \mathbf{Y}_{(ij}^{2m}\mathbf{Y}_{kl)}^{2m'}, \\ \mathbf{A}_{ijkl} &= \mathbf{C}_{ijkl} - \mathbf{S}_{ijkl} = \langle \langle (\mathbf{D}^{00})^2 \rangle \rangle \left(\delta_{ij}\delta_{kl} - \delta_{(ij}\delta_{kl)} \right) \\ &\quad + \sum_m \langle \langle \mathbf{D}^{00}\mathbf{D}^{2m} \rangle \rangle \left(\delta_{ij}\mathbf{Y}_{kl}^{2m} + \mathbf{Y}_{ij}^{2m}\delta_{kl} - 2\delta_{(ij}\mathbf{Y}_{kl)}^{2m} \right) \\ &\quad + \sum_{m,m'} \langle \langle \mathbf{D}^{2m}\mathbf{D}^{2m'} \rangle \rangle \left(\mathbf{Y}_{ij}^{2m}\mathbf{Y}_{kl}^{2m'} - \mathbf{Y}_{(ij}^{2m}\mathbf{Y}_{kl)}^{2m'} \right). \end{aligned}$$

Although \mathbf{A}_{ijkl} does not seem to have any particular symmetry at first glance, it can be mapped to a second order symmetric tensor using Eq. (15b):

$$\begin{aligned} \mathbf{A}_{pq} &= \delta_{pq}(\mathbf{A}_{iikk} - \mathbf{A}_{ikik}) + 2(\mathbf{A}_{pkqk} - \mathbf{A}_{pqkk}) \\ &= 2\langle \langle (\mathbf{D}^{00})^2 \rangle \rangle \delta_{pq} - 2\sum_m \langle \langle \mathbf{D}^{00}\mathbf{D}^{2m} \rangle \rangle \mathbf{Y}_{pq}^{2m} \\ &\quad - \sum_{m,m'} \langle \langle \mathbf{D}^{2m}\mathbf{D}^{2m'} \rangle \rangle \left(\mathbf{Y}_{ij}^{2m}\mathbf{Y}_{ij}^{2m'}\delta_{pq} - 2\mathbf{Y}_{pk}^{2m}\mathbf{Y}_{qk}^{2m'} \right). \end{aligned}$$

This leaves us with symmetric tensors \mathbf{D}_{ij} , \mathbf{S}_{ijkl} , and \mathbf{A}_{pq} written as a function of compartmental diffusion tensor covariances, for which we can compute irreducible decompositions following Eqs. (55). Below we group their spherical tensor elements according to their degree ℓ :

$$\begin{aligned} \mathbf{D}^{00} &= \langle \langle \mathbf{D}^{00} \rangle \rangle, \\ \mathbf{S}^{00} &= \langle \langle (\mathbf{D}^{00})^2 \rangle \rangle + \frac{1}{5}\sum_{m',m''} \langle \langle \mathbf{D}^{2m'}\mathbf{D}^{2m''} \rangle \rangle \mathbf{Y}_{(ij}^{2m'}\mathbf{Y}_{kl)}^{2m''}\mathbf{Y}_{ijkl}^{00*}, \\ \mathbf{A}^{00} &= 2\langle \langle (\mathbf{D}^{00})^2 \rangle \rangle - \frac{1}{2}\sum_{m',m''} \langle \langle \mathbf{D}^{2m'}\mathbf{D}^{2m''} \rangle \rangle \mathbf{Y}_{(ij}^{2m'}\mathbf{Y}_{kl)}^{2m''}\mathbf{Y}_{ijkl}^{00*}, \\ \mathbf{D}^{2m} &= \langle \langle \mathbf{D}^{2m} \rangle \rangle, \\ \mathbf{S}^{2m} &= 2\langle \langle \mathbf{D}^{00}\mathbf{D}^{2m} \rangle \rangle + \frac{4}{7}\sum_{m',m''} \langle \langle \mathbf{D}^{2m'}\mathbf{D}^{2m''} \rangle \rangle \mathbf{Y}_{(ij}^{2m'}\mathbf{Y}_{kl)}^{2m''}\mathbf{Y}_{ijkl}^{2m*}, \\ \mathbf{A}^{2m} &= -2\langle \langle \mathbf{D}^{00}\mathbf{D}^{2m} \rangle \rangle + 2\sum_{m',m''} \langle \langle \mathbf{D}^{2m'}\mathbf{D}^{2m''} \rangle \rangle \mathbf{Y}_{(ij}^{2m'}\mathbf{Y}_{kl)}^{2m''}\mathbf{Y}_{ijkl}^{2m*}, \\ \mathbf{S}^{4m} &= \frac{8}{35}\sum_{m',m''} \langle \langle \mathbf{D}^{2m'}\mathbf{D}^{2m''} \rangle \rangle \mathbf{Y}_{(ij}^{2m'}\mathbf{Y}_{kl)}^{2m''}\mathbf{Y}_{ijkl}^{4m*}, \end{aligned} \quad (57)$$

using $\mathbf{Y}_{ij}^{2m}\mathbf{Y}_{ij}^{2m'} = \frac{3}{2}\mathbf{Y}_{(ij}^{2m}\mathbf{Y}_{kl)}^{2m'}\mathbf{Y}_{ijkl}^{00}$ and $\mathbf{Y}_{ij}^{2m'}\mathbf{Y}_{jk}^{2m''}\mathbf{Y}_{ki}^{2m*} = \frac{3}{2}\mathbf{Y}_{(ij}^{2m'}\mathbf{Y}_{kl)}^{2m''}\mathbf{Y}_{ijkl}^{2m*}$.

The connection (18) to the QT decomposition (8) is established via the relations of the triple products of spherical basis tensors to the products of Clebsch-Gordan coefficients:

$$\begin{aligned} \mathbf{Y}_{(ij}^{2m'}\mathbf{Y}_{kl)}^{2m''}\mathbf{Y}_{ijkl}^{00*} &= 5\langle 2020|00 \rangle \langle 2m'2m''|00 \rangle, \\ \mathbf{Y}_{(ij}^{2m'}\mathbf{Y}_{kl)}^{2m''}\mathbf{Y}_{ijkl}^{2m*} &= \frac{7}{4}\langle 2020|20 \rangle \langle 2m'2m''|2m \rangle, \\ \mathbf{Y}_{(ij}^{2m'}\mathbf{Y}_{kl)}^{2m''}\mathbf{Y}_{ijkl}^{4m*} &= \frac{35}{8}\langle 2020|40 \rangle \langle 2m'2m''|4m \rangle, \end{aligned} \quad (58)$$

see derivation of the Supplementary Eq. (58). We then use Eq. (8b) to express the sums in Eqs. (57) via $\mathbf{T}^{\ell m}$:

$$\begin{aligned} \sum_{m',m''} \langle \langle \mathbf{D}^{2m'}\mathbf{D}^{2m''} \rangle \rangle \mathbf{Y}_{(ij}^{2m'}\mathbf{Y}_{kl)}^{2m''}\mathbf{Y}_{ijkl}^{00*} &= 5\mathbf{T}^{00}, \\ \sum_{m',m''} \langle \langle \mathbf{D}^{2m'}\mathbf{D}^{2m''} \rangle \rangle \mathbf{Y}_{(ij}^{2m'}\mathbf{Y}_{kl)}^{2m''}\mathbf{Y}_{ijkl}^{2m*} &= \frac{7}{4}\mathbf{T}^{2m}, \\ \sum_{m',m''} \langle \langle \mathbf{D}^{2m'}\mathbf{D}^{2m''} \rangle \rangle \mathbf{Y}_{(ij}^{2m'}\mathbf{Y}_{kl)}^{2m''}\mathbf{Y}_{ijkl}^{4m*} &= \frac{35}{8}\mathbf{T}^{4m}, \end{aligned} \quad (59)$$

which after simple algebra proves the system (18).

At first glance, Clebsch-Gordan coefficients may seem a non-intuitive way to combine the components $\langle\langle D^{2m'} D^{2m''} \rangle\rangle$. However, they can yield elegant simplifications. Consider T^{00} as defined in Eq. (8b). Using $\langle 2020|00 \rangle = 1/\sqrt{5}$ and $\langle 2m2m'|00 \rangle = (-1)^m \delta_{m,-m'}/\sqrt{5}$, as well as Eq. (47), we get

$$\begin{aligned} T^{00} &= \langle 2020|00 \rangle \sum_{m,m'} \langle 2m2m'|00 \rangle \langle\langle D^{2m} D^{2m'} \rangle\rangle \\ &= \frac{1}{5} \sum_m (-1)^m \langle\langle D^{2m} D^{2-m} \rangle\rangle = \frac{1}{5} \sum_m \langle\langle D^{2m} D^{2m*} \rangle\rangle. \end{aligned} \quad (60)$$

Intrinsic invariants of $T^{(4)} = S^{(4)}$

The 3 independent invariants for a 2nd-order tensor, such as D , can be constructed from the coefficients of its characteristic polynomial $p(\lambda) = \det(D - \lambda I) = -\lambda^3 + c_2\lambda^2 + c_1\lambda + c_0$: $c_0 = \det D$, $c_1 = \frac{1}{2}(\text{tr } D^2 - \text{tr } D)$, and $c_2 = \text{tr } D$. In the main text, we mapped them onto D_0 , D_2 , and $D_{2|3}$, Eqs. (5) and (23), by first isolating the scalar and the STF-2 parts, Eq. (3).

For 4th-order tensors, the characteristic polynomial needs to be defined. Fortunately, 4th-order 3d tensors with minor symmetry, like the elasticity or covariance tensors, can be mapped to a 2nd-order 6d tensor $C \rightarrow C_{6 \times 6}$ using the Kelvin/Mandel notation^{50,65}. Explicitly⁶⁵:

$$C_{6 \times 6} = \begin{pmatrix} C_{1111} & C_{1122} & C_{1133} & \sqrt{2}C_{1112} & \sqrt{2}C_{1113} & \sqrt{2}C_{1123} \\ C_{1122} & C_{2222} & C_{2233} & \sqrt{2}C_{2212} & \sqrt{2}C_{2213} & \sqrt{2}C_{2223} \\ C_{1133} & C_{2233} & C_{3333} & \sqrt{2}C_{3312} & \sqrt{2}C_{3313} & \sqrt{2}C_{3323} \\ \sqrt{2}C_{1112} & \sqrt{2}C_{2212} & \sqrt{2}C_{3312} & 2C_{1212} & 2C_{1213} & 2C_{1223} \\ \sqrt{2}C_{1113} & \sqrt{2}C_{2213} & \sqrt{2}C_{3313} & 2C_{1312} & 2C_{1313} & 2C_{1323} \\ \sqrt{2}C_{1123} & \sqrt{2}C_{2223} & \sqrt{2}C_{3323} & 2C_{2312} & 2C_{2313} & 2C_{2323} \end{pmatrix}, \quad (61)$$

where the major symmetry of C makes $C_{6 \times 6}$ symmetric, and factors $\sqrt{2}$ and 2 account for repeated elements, such that we can define traces of the powers of 4th-order tensors as

$$\text{tr } C^n \equiv C_{i_1 j_1 i_2 j_2} \dots C_{i_n j_n i_1 j_1} = \text{tr } (C_{6 \times 6})^n. \quad (62)$$

The mapping $C \rightarrow C_{6 \times 6}$ allows one to extract 6 invariants from the characteristic polynomial of a square matrix $C_{6 \times 6}$. This approach was extended⁵⁰ by considering the coefficients of the polynomial $\tilde{p}(v, \mu) = \det(C_{6 \times 6} - I^{(4)}(v, \mu))$ with $I^{(4)}_{ijkl}(v, \mu) = \frac{v}{2}(\delta_{ik}\delta_{jl} + \delta_{il}\delta_{jk}) + \mu\delta_{ij}\delta_{kl}$. However, such invariants do not form a complete set, and besides, they mix the irreducible representations and symmetries.

The irreducible decomposition (6) allows us to keep track of symmetries, and consider a more constrained problem: find the 6 intrinsic invariants of the only component $S^{(4)} = T^{(4)}$ of C that is neither a scalar nor an STF-2 tensor. For that, we use the mapping (61) to define a 6×6 matrix $S_{6 \times 6}^{(4)}$, cf. Supplementary Eq. (S26). We consider standard characteristic polynomial $p(\lambda) = \det(S_{6 \times 6}^{(4)} - \lambda I)$ because, as it turns out, no extra invariants arise from the coefficients of $\tilde{p}(\lambda, \mu)$ for $S_{6 \times 6}^{(4)}$.

From direct inspection of $S_{6 \times 6}^{(4)}$ (Supplementary Section S4) we find that its trace and one of its eigenvalues are zero. The

polynomial $p(\lambda) = \lambda^6 + p_5\lambda^5 + \dots + p_1\lambda + p_0$ has only 4 algebraically independent coefficients:

$$\begin{aligned} p_1 &= \frac{1}{6} \text{tr}(S^{(4)})^2 \text{tr}(S^{(4)})^3 - \frac{1}{5} \text{tr}(S^{(4)})^5, \\ p_2 &= \frac{1}{8} \text{tr}(S^{(4)})^2 \text{tr}(S^{(4)})^2 - \frac{1}{4} \text{tr}(S^{(4)})^4, \\ p_3 &= -\frac{1}{3} \text{tr}(S^{(4)})^3, \\ p_4 &= -\frac{1}{2} \text{tr}(S^{(4)})^2, \end{aligned} \quad (63)$$

since $p_0 = \det S_{6 \times 6}^{(4)} = 0$ and $p_5 = -\text{tr } S^{(4)} = 0$ (traces are defined according to Eq. (62)). Thus $p(\lambda)$ has 4 nonzero independent roots (eigenvalues of $S_{6 \times 6}^{(4)}$). Since by Cayley–Hamilton theorem, each matrix satisfies its characteristic equation, $p(S_{6 \times 6}^{(4)}) = 0$, the 4 traces $\text{tr}(S^{(4)})^2$, $\text{tr}(S^{(4)})^3$, $\text{tr}(S^{(4)})^4$, and $\text{tr}(S^{(4)})^5$, are the 4 algebraically independent invariants that determine all traces of higher powers of $S^{(4)}$. The latter can be iteratively obtained from relations $\text{tr}[(S^{(4)})^n p(S^{(4)})] = 0$, $n = 0, 1, 2, \dots$, by expressing $\text{tr}(S^{(4)})^{6+n}$ via the above 4 independent traces that also define the characteristic polynomial coefficients, Eq. (63).

The remaining 2 independent intrinsic invariants of $S^{(4)}$ can be obtained from its eigentensor decomposition⁶⁵

$$S_{ijkl}^{(4)} = \sum_{a=1}^6 \lambda_a E_{ij}^{(a)} E_{kl}^{(a)}, \quad (64)$$

where λ_a and $E_{ij}^{(a)}$ are the eigenvalues and eigentensors of $S^{(4)}$ according to the mapping (61). Namely, λ_a are the eigenvalues of $S_{6 \times 6}^{(4)}$, and $\hat{v}^{(a)} = [v_{xx}^{(a)}, v_{yy}^{(a)}, v_{zz}^{(a)}, v_{xy}^{(a)}, v_{xz}^{(a)}, v_{yz}^{(a)}]^t$ are its normalized 6d eigenvectors, yielding the eigentensors

$$E_{ij}^{(a)} = \begin{pmatrix} v_{xx}^{(a)} & \frac{1}{\sqrt{2}}v_{xy}^{(a)} & \frac{1}{\sqrt{2}}v_{xz}^{(a)} \\ \frac{1}{\sqrt{2}}v_{xy}^{(a)} & v_{yy}^{(a)} & \frac{1}{\sqrt{2}}v_{yz}^{(a)} \\ \frac{1}{\sqrt{2}}v_{xz}^{(a)} & \frac{1}{\sqrt{2}}v_{yz}^{(a)} & v_{zz}^{(a)} \end{pmatrix}. \quad (65)$$

The orthogonality of $\hat{v}^{(a)}$ induces the tensor orthogonality $E_{ij}^{(a)} E_{ij}^{(b)} = \delta_{ab}$. Based on Supplementary Section S4, the eigenvector $\hat{v}^{(a_0)} = \frac{1}{\sqrt{3}}(1, 1, 1, 0, 0, 0)^t$, associated with a zero eigenvalue $\lambda_{a_0} = 0$, corresponds to the eigentensor

$$E_{ij}^{(a_0)} = \frac{1}{\sqrt{3}}\delta_{ij}; \quad \text{tr } E^{(a)} = 0, \quad a \neq a_0, \quad (66)$$

with the latter equality for all other 5 eigentensors stemming from their orthogonality to $E^{(a_0)}$. Note that, although the tensor products $E_{ij}^{(a)} E_{kl}^{(a)}$ are not fully symmetric, when combined according to Eq. (64), $S_{ijkl}^{(4)}$ becomes fully symmetric.

We now define the remaining 2 independent invariants of $S^{(4)}$ by arranging the above eigentensors into the following 2 combinations:

$$E_{ij} = \sum_{a=1}^6 \lambda_a E_{ij}^{(a)}, \quad \text{and} \quad \tilde{E}_{ij} = \sum_{a \neq a_0} E_{ij}^{(a)}. \quad (67)$$

TABLE II. Description of the four RICE protocols (rows) acquired for each volunteer. Imaging parameters were kept constant for all protocols and numbers denote the different directions sampled on each shell. All b-values are in microstructure units $\text{ms}/\mu\text{m}^2$.

Protocol	$b = 0$	$b_{\text{LTE}} = 1$	$b_{\text{LTE}} = 2$	$b_{\text{PTE}} = 1.5$	$b_{\text{STE}} = 1.5$	$t_{\text{acq}} [\text{min' sec''}]$
DKI	1	30	60	-	-	6' 43"
iRICE (MD+FA+MK)	1	6	6	-	-	1' 14"
RICE	2	30	60	30	-	11' 20"
iRICE (MD+FA+MK+μFA)	2	6	6	-	3	1' 56"

Analogously to the D-tensor example above, traces of the powers of 2nd-order tensors E and \tilde{E} are rotationally invariant; the traces of 1st, 2nd and 3rd powers of these matrices are algebraically independent. Further, by construction, $\text{tr } E = \text{tr } \tilde{E} = 0$. One can also check that $\text{tr } E^2 = \text{tr } (S^{(4)})^2$ given by one of the previously found invariants, and $\text{tr } \tilde{E}^2 = 5$ independent of $S^{(4)}$. Therefore, we identify the two remaining independent intrinsic invariants of $S^{(4)}$ with $\text{tr } E^3$ and $\text{tr } \tilde{E}^3$. To summarize, the 6 intrinsic invariants of $S^{(4)}$ are:

$$S_{4|n} = \left(\frac{8}{35} \text{tr } (S^{(4)})^n \right)^{1/n}, \quad n = 2, \dots, 5; \quad (68)$$

$$S_{4|6} = \text{tr}^{1/3} E^3, \quad S_{4|7} = \text{tr}^{1/3} \tilde{E}^3,$$

with E and \tilde{E} defined in Eq. (67). They are normalized such that $S_4 \equiv S_{4|2}$ is the 2-norm of S^{4m} , cf. Eq. (26). The independence of invariants from the same irreducible component can be checked with the Jacobian criterion for algebraic independence¹⁰⁷.

One could alternatively define $S^{(4)}$ intrinsic invariants using the general formulation for $\ell = 4$

$$\tilde{S}_{\ell|n} = \left((2\ell + 1) \int_{\mathbb{S}^2} d\hat{n} (S^{(\ell)}(\hat{n}))^n \right)^{1/n}, \quad n = 2, \dots, 2\ell - 1, \quad (69)$$

The integral over \mathbb{S}^2 acts as a projector of n -th order powers of $S^{(4)}(\hat{n})$ onto the isotropic subspace. This means that $\tilde{S}_{\ell|n}$ are obtained by coupling the spherical harmonic components $S^{4m_1} \dots S^{4m_n}$ to zero total angular momentum. For $n = 2$, one can use Eq. (45) and Supplementary Eq. (S14) to find $\tilde{S}_{4|2}^2 = 9 \sum_{m, m'} S^{4m} S^{4m'} \langle 4040|00 \rangle \langle 4m4m'|00 \rangle = \sum_m S^{4m} S^{4m*} = S_4^2$, cf. Eq. (26). Here, Clebsch–Gordan coefficients enforce $m' = -m$, and the contraction reduces to a sum over conjugate pairs, as in Eq. (60). Both definitions (68) and (69) generate complete sets of invariants, and the first four invariants (69), with $n = 2, \dots, 5$, correspond to the combinations of the traces $\text{tr } (S^{(4)})^n$, while the $n = 6, 7$ ones are independent, and therefore can serve as alternatives to $S_{4|6}$ and $S_{4|7}$. The construction (69) is similar to the definition of spherical harmonic dMRI signal invariants in Ref.³⁷, but is applied to a specific $\ell = 4$ component $S^{(4)}$, rather than to a mixture such as $S = S^{(0)} \oplus S^{(2)} \oplus S^{(4)}$. Working with the pure $\ell = 4$ component allows one to algebraically relate any $\tilde{S}_{4|n}$ to the combination of the spherical tensor components S^{4m} via Clebsch–Gordan theory.

MRI experiments

After providing informed consent, three healthy volunteers (23 yo and 25 yo females, 33 yo male) underwent MRI in a whole body 3T-system (Siemens, Prisma) using a 32-channel head coil. Maxwell-compensated free gradient diffusion waveforms¹⁰⁸ were used to yield linear, planar, and spherical B-tensor encoding using a prototype spin echo sequence with EPI readout¹⁰⁹. Four RICE dMRI datasets were acquired according to Table II. Imaging parameters: voxel size = $2 \times 2 \times 2 \text{ mm}^3$, $T_R = 4.2 \text{ s}$, $T_E = 90 \text{ ms}$, bandwidth = 1818 Hz/Px, $R_{\text{GRAPPA}} = 2$, partial Fourier = 6/8, multiband = 2. Scan time was 15 minutes per subject for all protocols (DKI was subsampled from RICE).

For the clinical validation^{47,48}, 627 subjects (aged 42.7 ± 13.6 years, 443 females) identified with a clinical diagnosis of multiple sclerosis who were referred for MRI of the head at NYU Langone Health between November 2014 and June 2020. 562 controls (aged 42.9 ± 14.1 years, 386 females) were selected from subjects with normal brain MRI and no history of neurological disorder, referred for imaging due to headache or dizziness. Groups were matched for age and sex. Subjects underwent MRI on whole body Siemens 3T-systems (Prisma: 47.1%, Skyra: 52.9%). The clinical dMRI protocol used a monopolar EPI sequence with linear B-tensor encoding as follows: 4–5 $b = 0$ images, $b_{\text{LTE}} = 1 \text{ ms}/\mu\text{m}^2$ along 20 directions and $b_{\text{LTE}} = 2 \text{ ms}/\mu\text{m}^2$ along 60 directions. Imaging parameters: voxel size = $1.7 \times 1.7 \times 3 \text{ mm}^3$, $T_R = 3.2 - 4 \text{ s}$ and $T_E = 70 - 96 \text{ ms}$ on Prisma, and $T_R = 3.5 - 4.3 \text{ s}$ and $T_E = 70 - 96 \text{ ms}$ on Skyra, $R_{\text{GRAPPA}} = 2$, partial Fourier = 6/8, multiband = 2. Scan time was 6 minutes per subject.

Image pre-processing

All four protocols in Table II were processed identically and independently for each subject. Magnitude and phase data were reconstructed. Then, a phase estimation and unwinding step preceded the denoising of the complex images¹¹⁰. Denoising was done using the Marchenko–Pastur principal component analysis method¹¹¹ on the real part of the phase-unwinded data. An advantage of denoising before taking the magnitude of the data is that Rician bias is reduced significantly⁷¹. We also processed this data using only magnitude data. Here, magnitude denoising and rician bias correction were applied, see results in Supplementary Section S7. Only magnitude denoising was applied to the clinical LTE dataset. Data was subsequently processed with the DESIGNER pipeline⁴⁸. Denoised images were corrected for Gibbs ringing artifacts accounting for the

partial Fourier acquisition¹¹², based on re-sampling images using local sub-voxel shifts. Images were then rigidly aligned and corrected for eddy current distortions and subject motion simultaneously¹¹³. A $b = 0$ image with reverse phase encoding was included for correction of EPI-induced distortions¹¹⁴. Finally, MRI voxels were locally smoothed based on spatial and intensity similarity akin to Ref.¹¹⁵.

Parameter estimation

Two variants of the cumulant expansion were fit to the RICE and clinical datasets. This depended on which parameters each protocol was sensitive to. For the full DKI, full RICE, and clinical LTE protocols, Eq. (10) was used, while for the iRICE protocols, parameters were estimated according to Eq. (35). Weighted linear least squares were used for fitting¹¹⁶ to highlight the gain achieved purely by acquisition optimization. Including positivity constraints to improve parameters robustness¹¹⁷ is straightforward for spherical tensors but is

outside of the scope of this work.

DATA AVAILABILITY

Example anonymized and processed dMRI data used for the RICE analysis are available at <https://ca12r.net/resources/rotational-invariants-of-the-cumulant-expansion-the-rice-toolbox/>. The large prospective clinical dMRI dataset contains protected health information and is therefore not publicly available; we provide access to the summary statistics computed using RICE at <https://github.com/NYU-DiffusionMRI/RICE>.

CODE AVAILABILITY

All codes for RICE parameter estimation were implemented in MATLAB (R2021a, MathWorks, Natick, Massachusetts). These are publicly available as part of the RICE toolbox at <https://github.com/NYU-DiffusionMRI/RICE>.

[1] P. T. Callaghan, *Principles of Nuclear Magnetic Resonance Microscopy*, Oxford Science Publications (Clarendon, 1991).

[2] D. K. Jones, *Diffusion MRI* (Oxford University Press, 2010).

[3] D. G. Cory, A. N. Garroway, and J. B. Miller, Applications of spin transport as a probe of local geometry, *Polymer Preprints* **31**, 149 (1990).

[4] J. Tanner, Self diffusion of water in frog muscle, *Biophysical Journal* **28**, 107 (1979).

[5] G. J. Stanisz, A. Szafer, G. A. Wright, and R. M. Henkelman, An analytical model of restricted diffusion in bovine optic nerve, *Magnetic Resonance in Medicine* **37**, 103 (1997).

[6] P. J. Basser, J. Mattiello, and D. LeBihan, Estimation of the effective self-diffusion tensor from the NMR spin echo, *Journal of Magnetic Resonance* **103**, 247 (1994).

[7] I. O. Jelescu and M. D. Budde, Design and validation of diffusion MRI models of white matter, *Frontiers in Physics* **5**, 61 (2017).

[8] D. S. Novikov, E. Fieremans, S. N. Jespersen, and V. G. Kiselev, Quantifying brain microstructure with diffusion MRI: Theory and parameter estimation, *NMR in Biomedicine* , e3998 (2019).

[9] D. C. Alexander, T. B. Dyrby, M. Nilsson, and H. Zhang, Imaging brain microstructure with diffusion MRI: practicality and applications, *NMR in Biomedicine* **32**, e3841 (2019).

[10] D. S. Novikov, The present and the future of microstructure MRI: From a paradigm shift to normal science, *Journal of Neuroscience Methods* **351**, 108947 (2021).

[11] V. G. Kiselev, Microstructure with diffusion MRI: what scale we are sensitive to?, *Journal of Neuroscience Methods* **347**, 108910 (2021).

[12] N. Weiskopf, L. J. Edwards, G. Helms, S. Mohammadi, and E. Kirilina, Quantitative magnetic resonance imaging of brain anatomy and in vivo histology, *Nature Reviews Physics* **3**, 570 (2021).

[13] B. Lampinen, F. Szczepankiewicz, J. Lätt, L. Knutsson, J. Mårtensson, I. M. Björkman-Burtscher, D. van Westen, P. C. Sundgren, F. Ståhlberg, and M. Nilsson, Probing brain tissue microstructure with mri: principles, challenges, and the role of multidimensional diffusion-relaxation encoding, *NeuroImage* **282**, 120338 (2023).

[14] Y. Assaf, Can we use diffusion MRI as a bio-marker of neurodegenerative processes?, *BioEssays* **30**, 1235 (2008).

[15] M. Nilsson, E. Englund, F. Szczepankiewicz, D. van Westen, and P. C. Sundgren, Imaging brain tumour microstructure, *NeuroImage* **182**, 232 (2018), microstructural Imaging.

[16] D. S. Novikov, J. H. Jensen, J. A. Helpern, and E. Fieremans, Revealing mesoscopic structural universality with diffusion., *Proceedings of the National Academy of Sciences of the United States of America* **111**, 5088 (2014).

[17] V. G. Kiselev, Fundamentals of diffusion MRI physics, *NMR in Biomedicine* **30**, 1 (2017).

[18] P. P. Mitra, Multiple wave-vector extensions of the NMR pulsed-field-gradient spin-echo diffusion measurement, *Physical Review B* **51**, 15074 (1995).

[19] S. Mori and P. C. M. Van Zijl, Diffusion weighting by the trace of the diffusion tensor within a single scan, *Magnetic Resonance in Medicine* **33**, 41 (1995).

[20] N. Shemesh, S. N. Jespersen, D. C. Alexander, Y. Cohen, I. Drobniac, T. B. Dyrby, J. Finterbusch, M. A. Koch, T. Kuder, F. Laun, M. Lawrenz, H. Lundell, P. P. Mitra, M. Nilsson, E. Özarslan, D. Topgaard, and C.-F. Westin, Conventions and nomenclature for Double Diffusion Encoding NMR and MRI, *Magnetic Resonance in Medicine* **75**, 82 (2015).

[21] C.-F. Westin, H. Knutsson, O. Pasternak, F. Szczepankiewicz, E. Özarslan, D. van Westen, C. Mattisson, M. Bogren, L. J. O'Donnell, M. Kubicki, D. Topgaard, and M. Nilsson, q-space trajectory imaging for multidimensional diffusion MRI of the human brain, *NeuroImage* **135**, 345 (2016).

[22] D. Topgaard, Multidimensional diffusion MRI, *Journal of Magnetic Resonance* **275**, 98 (2017).

[23] N. G. van Kampen, *Stochastic Processes in Physics and Chemistry*, 1st ed. (Elsevier, Oxford, 1981).

[24] V. G. Kiselev, The cumulant expansion: an overarching mathematical framework for understanding diffusion NMR, in *Diffusion MRI: Theory, Methods and Applications*, edited by D. K. Jones (Oxford University Press, Oxford, 2010) Chap. 10, pp. 152–168.

[25] S. N. Jespersen, H. Lundell, C. K. Sønderby, and T. B. Dyrby, Orientationally invariant metrics of apparent compartment eccentricity from double pulsed field gradient diffusion experiments, *NMR in Biomedicine* **26**, 1647 (2013).

[26] R. N. Henriques, S. N. Jespersen, and N. Shemesh, Correlation tensor magnetic resonance imaging, *NeuroImage* **211**, 116605 (2020).

[27] S. Desmond-Hellmann, Toward precision medicine: A new social contract?, *Science Translational Medicine* **4**, 129ed3 (2012).

[28] L. R. Frank, Characterization of anisotropy in high angular resolution diffusion-weighted mri, *Magnetic Resonance in Medicine* **47**, 1083 (2002).

[29] M. Kazhdan, T. Funkhouser, and S. Rusinkiewicz, Rotation invariant spherical harmonic representation of 3d shape descriptors, in *Proceedings of the 2003 Eurographics/ACM SIGGRAPH Symposium on Geometry Processing*, SGP 03 (Eurographics Association, 2003) pp. 156–164.

[30] B. Gutman, Y. Wang, L. M. Lui, T. F. Chan, and P. M. Thompson, Hippocampal surface discrimination via invariant descriptors of spherical conformals maps, in *2007 4th IEEE International Symposium on Biomedical Imaging: From Nano to Macro* (2007) pp. 1316–1319.

[31] A. Fuster, J. van de Sande, L. J. Astola, C. Poupon, J. Veltrop, and B. M. ter Haar Romeny, *Fourth-order tensor invariants in high angular resolution diffusion imaging*, CASA-report (Technische Universiteit Eindhoven, Eindhoven, The Netherlands, 2011).

[32] H. Mirzaalian, L. Ning, P. Savadjiev, O. Pasternak, S. Bouix, O. Michailovich, G. Grant, C. Marx, R. Morey, L. Flashman, M. George, T. McAllister, N. Andaluz, L. Shutter, R. Coimbra, R. Zafonte, M. Coleman, M. Kubicki, C. Westin, M. Stein, M. Shenton, and Y. Rathi, Inter-site and inter-scanner diffusion mri data harmonization, *NeuroImage* **135**, 311 (2016).

[33] M. Reisert, E. Kellner, B. Dhital, J. Hennig, and V. G. Kiselev, Disentangling micro from mesostructure by diffusion MRI: A Bayesian approach, *NeuroImage* **147**, 964 (2017).

[34] H. Skibbe and M. Reisert, Spherical Tensor Algebra: A Toolkit for 3D Image Processing, *Journal of Mathematical Imaging and Vision* **58**, 349 (2017).

[35] D. S. Novikov, J. Veraart, I. O. Jelescu, and E. Fieremans, Rotationally-invariant mapping of scalar and orientational metrics of neuronal microstructure with diffusion MRI, *NeuroImage* **174**, 518 (2018).

[36] M. Reisert, V. A. Coenen, C. Kaller, K. Egger, and H. Skibbe, HAMLET: Hierarchical harmonic filters for learning tracts from diffusion mri (2018), [arXiv:1807.01068 \[cs.CV\]](https://arxiv.org/abs/1807.01068).

[37] M. Zucchelli, S. Deslauriers-Gauthier, and R. Deriche, A computational framework for generating rotation invariant features and its application in diffusion mri, *Medical Image Analysis* **60**, 101597 (2020).

[38] M. Herberthson, E. Özarslan, and C.-F. Westin, Variance measures for symmetric positive (semi-) definite tensors in two dimensions, in *Anisotropy Across Fields and Scales*, edited by E. Özarslan, T. Schultz, E. Zhang, and A. Fuster (Springer International Publishing, Cham, 2021) pp. 3–22.

[39] H. G. Moss, T. Feiwei, A. Benitez, and J. H. Jensen, Linear rotationally invariant kurtosis measures from double diffusion encoding mri, *Magnetic Resonance Imaging* **120**, 110399 (2025).

[40] S. M. Smith, G. Douaud, W. Chen, T. Hanayik, F. Alfaro-Almagro, K. Sharp, and L. T. Elliott, An expanded set of genome-wide association studies of brain imaging phenotypes in UK Biobank, *Nature Neuroscience* **24**, 737 (2021).

[41] C. R. Jack Jr., M. A. Bernstein, N. C. Fox, P. Thompson, G. Alexander, D. Harvey, B. Borowski, P. J. Britson, J. L. Whitwell, C. Ward, A. M. Dale, J. P. Felmlee, J. L. Gunter, D. L. Hill, R. Killiany, N. Schuff, S. Fox-Bosetti, C. Lin, C. Studholme, C. S. DeCarli, G. Krueger, H. A. Ward, G. J. Metzger, K. T. Scott, R. Mallozzi, D. Blezek, J. Levy, J. P. Debbins, A. S. Fleisher, M. Albert, R. Green, G. Bartzikis, G. Glover, J. Mugler, and M. W. Weiner, The alzheimer’s disease neuroimaging initiative (adni): Mri methods, *Journal of Magnetic Resonance Imaging* **27**, 685 (2008).

[42] N. Jahanshad, P. V. Kochunov, E. Sprooten, R. C. Mandl, T. E. Nichols, L. Almasy, J. Blangero, R. M. Brouwer, J. E. Curran, G. I. de Zubicaray, R. Duggirala, P. T. Fox, L. E. Hong, B. A. Landman, N. G. Martin, K. L. McMahon, S. E. Medland, B. D. Mitchell, R. L. Olvera, C. P. Peterson, J. M. Starr, J. E. Sussmann, A. W. Toga, J. M. Wardlaw, M. J. Wright, H. E. Hulshoff Pol, M. E. Bastin, A. M. McIntosh, I. J. Deary, P. M. Thompson, and D. C. Glahn, Multi-site genetic analysis of diffusion images and voxelwise heritability analysis: A pilot project of the enigma-dti working group, *NeuroImage* **81**, 455 (2013).

[43] M. F. Glasser, S. M. Smith, D. S. Marcus, J. L. R. Andersson, E. J. Auerbach, T. E. J. Behrens, T. S. Coalson, M. P. Harms, M. Jenkinson, S. Moeller, E. C. Robinson, S. N. Sotiroopoulos, J. Xu, E. Yacoub, K. Ugurbil, and D. C. Van Essen, The human connectome project’s neuroimaging approach, *Nature Neuroscience* **19**, 1175 (2016).

[44] K. L. Miller, F. Alfaro-Almagro, N. K. Bangerter, D. L. Thomas, E. Yacoub, J. Xu, A. J. Bartsch, S. Jbabdi, S. N. Sotiroopoulos, J. L. R. Andersson, L. Griffanti, G. Douaud, T. W. Okell, P. Weale, I. Dragouni, S. Garratt, S. Hudson, R. Collins, M. Jenkinson, P. M. Matthews, and S. M. Smith, Multimodal population brain imaging in the UK Biobank prospective epidemiological study, *Nature Neuroscience* **19**, 1523 (2016).

[45] N. D. Volkow, G. F. Koob, R. T. Croyle, D. W. Bianchi, J. A. Gordon, W. J. Koroshetz, E. J. Perez-Stable, W. T. Riley, M. H. Bloch, K. Conway, B. G. Deeds, G. J. Dowling, S. Grant, K. D. Howlett, J. A. Matochik, G. D. Morgan, M. M. Murray, A. Noronha, C. Y. Spong, E. M. Wargo, K. R. Warren, and S. R. Weiss, The conception of the abcd study: From substance use to a broad nih collaboration, *Developmental Cognitive Neuroscience* **32**, 4 (2018).

[46] J. R. Taylor, N. Williams, R. Cusack, T. Auer, M. A. Shafit, M. Dixon, L. K. Tyler, Cam-CAN, and R. N. Henson, The cambridge centre for ageing and neuroscience (Cam-CAN) data repository: Structural and functional mri, meg, and cognitive data from a cross-sectional adult lifespan sample, *NeuroImage* **144**, 262 (2017), data Sharing Part II.

[47] Y. Liao, S. Coelho, J. Chen, B. Ades-Aron, M. Pang, V. Stepanov, R. Osorio, T. Shepherd, Y. W. Lui, D. S. Novikov, and E. Fieremans, Mapping tissue microstructure of brain white matter in vivo in health and disease using diffusion MRI, *Imaging Neuroscience* **2**, 1 (2024).

[48] J. Chen, B. Ades-Aron, H.-H. Lee, S. Mehrin, M. Pang, D. S. Novikov, J. Veraart, and E. Fieremans, Optimization and validation of the designer preprocessing pipeline for clinical diffusion mri in white matter aging, *Imaging Neuroscience* **2**, 1 (2024).

[49] G. Backus, A geometrical picture of anisotropic elastic tensors, *Reviews of Geophysics* **8**, 633 (1970).

[50] J. Betten, Irreducible invariants of fourth-order tensors, *Mathematical Modelling* **8**, 29 (1987).

[51] A. Bóna, I. Bucataru, and M. Slawinski, Characterization of elasticity-tensor symmetries using $su(2)$, *Journal of Elasticity* **75**, 267 (2004).

[52] M. Moakher, Fourth-order cartesian tensors: old and new facts, notions and applications, *The Quarterly Journal of Mechanics and Applied Mathematics* **61**, 181 (2008).

[53] K. S. Thorne, Multipole expansions of gravitational radiation, *Rev. Mod. Phys.* **52**, 299 (1980).

[54] M. Tinkham, *Group Theory and Quantum Mechanics (Dover Books on Chemistry)* (Dover Publications, 2003).

[55] B. C. Hall, *Lie Groups, Lie Algebras, and Representations* (Springer, 2015).

[56] S. Eriksson, S. Lasic, M. Nilsson, C.-F. Westin, and D. Topgaard, NMR diffusion-encoding with axial symmetry and variable anisotropy: Distinguishing between prolate and oblate microscopic diffusion tensors with unknown orientation distribution, *The Journal of Chemical Physics* **142**, 104201 (2015).

[57] E. O. Stejskal and T. E. Tanner, Spin diffusion measurements: spin echoes in the presence of a time-dependent field gradient, *The Journal of Chemical Physics* **42**, 288 (1965).

[58] H. Hopf, Über die Abbildungen der dreidimensionalen Sphäre auf die Kugelflächen, *Mathematische Annalen* **104** (1931).

[59] S. Lasić, F. Szczepankiewicz, S. Eriksson, M. Nilsson, and D. Topgaard, Microanisotropy imaging: quantification of microscopic diffusion anisotropy and orientational order parameter by diffusion MRI with magic-angle spinning of the q-vector, *Frontiers in Physics* **2**, 11 (2014).

[60] C. Liu, R. Bammer, and M. E. Moseley, Generalized diffusion tensor imaging (gdti): A method for characterizing and imaging diffusion anisotropy caused by non-gaussian diffusion, *Israel Journal of Chemistry* **43**, 145 (2003), <https://onlinelibrary.wiley.com/doi/pdf/10.1560/HB5H-6XBR-1AW1-LNX9>.

[61] J. H. Jensen, J. A. Helpern, A. Ramani, H. Lu, and K. Kaczkynski, Diffusional Kurtosis Imaging: The quantification of non-gaussian water diffusion by means of magnetic resonance imaging, *Magnetic Resonance in Medicine* **53**, 1432 (2005).

[62] Y. Itin and F. W. Hehl, The constitutive tensor of linear elasticity: Its decompositions, cauchy relations, null lagrangians, and wave propagation, *Journal of Mathematical Physics* **54**, 042903 (2013).

[63] Y. Itin and F. W. Hehl, Irreducible decompositions of the elasticity tensor under the linear and orthogonal groups and their physical consequences, in *Journal of Physics: Conference Series*, Vol. 597 (IOP Publishing, 2015) p. 012046.

[64] A. Ghosh, T. Papadopoulos, and R. Deriche, Biomarkers for HARDI: 2nd & 4th order tensor invariants, in *2012 9th IEEE International Symposium on Biomedical Imaging (ISBI)* (2012) pp. 26–29.

[65] P. J. Basser and S. Pajevic, Spectral decomposition of a 4th-order covariance tensor: Applications to diffusion tensor MRI, *Signal Processing* **87**, 220 (2007).

[66] L. Qi, D. Han, and E. X. Wu, Principal invariants and inherent parameters of diffusion kurtosis tensors, *Journal of Mathematical Analysis and Applications* **349**, 165 (2009).

[67] T. Papadopoulos, A. Ghosh, and R. Deriche, Complete set of invariants of a 4thorder tensor: The 12 tasks of hardi from ternary quartics, in *Medical Image Computing and Computer Assisted Intervention – MICCAI 2014* (Springer International Publishing, Cham, 2014) pp. 233–240.

[68] H. Lu, J. Jensen, A. Ramani, and J. Helpern, Three-dimensional characterization of non-gaussian water diffusion in humans using diffusion kurtosis imaging, *NMR in Biomedicine* **19**, 236 (2006).

[69] B. Hansen, T. E. Lund, R. Sangill, and S. N. Jespersen, Experimentally and computationally fast method for estimation of a mean kurtosis, *Magnetic Resonance in Medicine* **69**, 1754 (2013).

[70] B. Hansen, N. Shemesh, and S. N. Jespersen, Fast imaging of mean, axial and radial diffusion kurtosis, *NeuroImage* **142**, 381 (2016).

[71] B. Ades-Aron, S. Coelho, G. Lemberskiy, J. Veraart, S. Baete, T. M. Shepherd, D. S. Novikov, and E. Fieremans, *De-noising improves cross-scanner and cross-protocol test-retest reproducibility of higher-order diffusion metrics* (2024), [arXiv:2407.18253 \[physics.med-ph\]](https://arxiv.org/abs/2407.18253).

[72] F. Szczepankiewicz, D. van Westen, E. Englund, C.-F. Westin, F. Ståhlberg, J. Lätt, P. C. Sundgren, and M. Nilsson, The link between diffusion MRI and tumor heterogeneity: Mapping cell eccentricity and density by diffusional variance decomposition (DIVIDE), *NeuroImage* **142**, 522 (2016).

[73] R. N. Henriques, S. N. Jespersen, and N. Shemesh, Microscopic anisotropy misestimation in spherical-mean single diffusion encoding MRI, *Magnetic Resonance in Medicine* **81**, 3245 (2019).

[74] G. R. Glenn, J. A. Helpern, A. Tabesh, and J. H. Jensen, Quantitative assessment of diffusional kurtosis anisotropy, *NMR in Biomedicine* **28**, 448 (2015).

[75] E. S. Hui, M. M. Cheung, L. Qi, and E. X. Wu, Towards better mr characterization of neural tissues using directional diffusion kurtosis analysis, *NeuroImage* **42**, 122 (2008).

[76] J. H. Jensen and J. A. Helpern, Mri quantification of non-gaussian water diffusion by kurtosis analysis, *NMR in Biomedicine* **23**, 698 (2010).

[77] F. Szczepankiewicz, S. Hoge, and C.-F. Westin, Linear, planar and spherical tensor-valued diffusion mri data by free waveform encoding in healthy brain, water, oil and liquid crystals, *Data in Brief* **25**, 104208 (2019).

[78] S. Mori, S. Wakana, L. M. Nagae-Poetscher, and P. C. M. van Zijl, Mri atlas of human white matter, *American Journal of Neuroradiology* **27**, 1384 (2006).

[79] B. Hansen, T. E. Lund, R. Sangill, E. Stubbe, J. Finsterbusch, and S. N. Jespersen, Experimental considerations for fast kurtosis imaging, *Magnetic resonance in medicine* **76**, 1455 (2016).

[80] M. Nilsson, F. Szczepankiewicz, J. Brabec, M. Taylor, C.-F. Westin, A. Golby, D. van Westen, and P. C. Sundgren, Tensor-valued diffusion MRI in under 3 minutes: an initial survey of microscopic anisotropy and tissue heterogeneity in intracranial tumors, *Magnetic Resonance in Medicine* **83**, 608 (2020).

[81] P. Seymour and T. Zaslavsky, Averaging sets: A generalization of mean values and spherical designs, *Advances in Mathematics* **52**, 213 (1984).

[82] S. N. Jespersen, Isotropic sampling of tensor-encoded diffusion mri, *Magnetic Resonance in Medicine* **93**, 2040 (2025), <https://onlinelibrary.wiley.com/doi/pdf/10.1002/mrm.30404>.

[83] N. Shemesh and Y. Cohen, Microscopic and compartment shape anisotropies in gray and white matter revealed by angular bipolar double-pfg mr, *Magnetic Resonance in Medicine* **65**, 1216 (2011), <https://onlinelibrary.wiley.com/doi/pdf/10.1002/mrm.22738>.

[84] S. Coelho, E. Fieremans, and D. S. Novikov, Microscopic kurtosis tensor invariants and dde 4-fold angular modulation in human brain diffusion mri, in *Proceedings of the International Society of Magnetic Resonance in Medicine*, Vol. 3884 (Wiley,

2025).

[85] D. S. Novikov and V. G. Kiselev, Effective medium theory of a diffusion-weighted signal, *NMR in Biomedicine* **23**, 682 (2010), <https://analyticalsciencejournals.onlinelibrary.wiley.com/doi/pdf/10.1002/nbm.5824>.

[86] A. Chakwizira, F. Szczepankiewicz, and M. Nilsson, Diffusion MRI with double diffusion encoding and variable mixing times disentangles water exchange from transient kurtosis, *Scientific Reports* **15** (2025).

[87] L. Ning, F. Szczepankiewicz, M. Nilsson, Y. Rathi, and C.-F. Westin, Probing tissue microstructure by diffusion skewness tensor imaging, *Scientific Reports* **13** (2021).

[88] V. G. Kiselev and K. A. Il'yasov, Is the “biexponential diffusion” biexponential?, *Magnetic Resonance in Medicine* **57**, 464 (2007).

[89] A. F. Frohlich, L. Ostergaard, and V. G. Kiselev, Effect of impermeable boundaries on diffusion-attenuated mr signal, *Journal of Magnetic Resonance* **179**, 223 (2006).

[90] N. Moutal and D. S. Grebenkov, Spectral branch points of the bloch–torrey operator, *Journal of Physics A: Mathematical and Theoretical* **55**, 455201 (2022).

[91] J. a. P. de Almeida Martins and D. Topgaard, Two-dimensional correlation of isotropic and directional diffusion using nmr, *Phys. Rev. Lett.* **116**, 087601 (2016).

[92] K. N. Magdoom, S. Pajevic, G. Dario, and P. J. Basser, A new framework for mr diffusion tensor distribution, *Scientific Reports* **11**, 2766 (2021).

[93] M. Hurlimann, K. Helmer, T. Deswiet, and P. Sen, Spin echoes in a constant gradient and in the presence of simple restriction, *Journal of Magnetic Resonance, Series A* **113**, 260 (1995).

[94] D. S. Grebenkov, Multiple correlation function approach to study restricted diffusion under arbitrary magnetic field, *Magnetic Resonance Imaging* **25**, 559 (2007).

[95] P. Basser and S. Pajevic, A normal distribution for tensor-valued random variables: applications to diffusion tensor MRI, *IEEE Transactions on Medical Imaging* **22**, 785 (2003).

[96] B. Jian, B. C. Vemuri, E. Özarslan, P. R. Carney, and T. H. Mareci, A novel tensor distribution model for the diffusion-weighted mr signal, *NeuroImage* **37**, 164 (2007).

[97] G. R. Glenn, J. A. Helpern, A. Tabesh, and J. H. Jensen, Quantitative assessment of diffusional kurtosis anisotropy, *NMR in Biomedicine* **28**, 448 (2015).

[98] S. N. Jespersen, C. D. Kroenke, L. Ostergaard, J. J. H. Ackerman, and D. A. Yablonskiy, Modeling dendrite density from magnetic resonance diffusion measurements, *NeuroImage* **34**, 1473 (2007).

[99] S. N. Jespersen, C. R. Bjarkam, J. R. Nyengaard, M. M. Chakravarty, B. Hansen, T. Vosgaard, L. Ostergaard, D. Yablonskiy, N. C. Nielsen, and P. Vestergaard-Poulsen, Neurite density from magnetic resonance diffusion measurements at ultrahigh field: Comparison with light microscopy and electron microscopy, *NeuroImage* **49**, 205 (2010).

[100] E. Fieremans, J. H. Jensen, and J. A. Helpern, White matter characterization with diffusional kurtosis imaging, *NeuroImage* **58**, 177 (2011).

[101] H. Zhang, T. Schneider, C. A. Wheeler-Kingshott, and D. C. Alexander, NODDI: Practical in vivo neurite orientation dispersion and density imaging of the human brain, *NeuroImage* **61**, 1000 (2012).

[102] S. N. Sotropoulos, T. E. Behrens, and S. Jbabdi, Ball and rackets: Inferring fiber fanning from diffusion-weighted MRI, *NeuroImage* **60**, 1412 (2012).

[103] J. H. Jensen, G. Russell Glenn, and J. A. Helpern, Fiber ball imaging, *NeuroImage* **124**, 824 (2016).

[104] G. Racah, Theory of complex spectra. ii, *Phys. Rev.* **62**, 438 (1942).

[105] E. U. Condon and G. H. Shortley, *The theory of atomic spectra* (The Cambridge University Press., Cambridge, 1964.).

[106] J. M. P. Coelho, S. Coelho, and A. F. Frangi, Tensorial formulation allowing to verify or falsify the microstructural standard model from multidimensional diffusion MRI, in *Proceedings of the International Society of Magnetic Resonance in Medicine*, Vol. 3560 (Wiley, 2019).

[107] E. Caruyer and R. Verma, On facilitating the use of hardi in population studies by creating rotation-invariant markers, *Medical Image Analysis* **20**, 87 (2015).

[108] F. Szczepankiewicz, C.-F. Westin, and M. Nilsson, Maxwell-compensated design of asymmetric gradient waveforms for tensor-valued diffusion encoding, *Magnetic Resonance in Medicine* **82**, 1424 (2019).

[109] F. Szczepankiewicz, J. Sjölund, F. Ståhlberg, J. Lätt, and M. Nilsson, Tensor-valued diffusion encoding for diffusional variance decomposition (divide): Technical feasibility in clinical mri systems, *PLOS ONE* **14**, 1 (2019).

[110] G. Lemberskiy, S. Baete, J. Veraart, T. Shepherd, E. Fieremans, and D. S. Novikov, Achieving sub-mm clinical diffusion MRI resolution by removing noise during reconstruction using random matrix theory, In *Proceedings 27th Scientific Meeting, 0770, International Society for Magnetic Resonance in Medicine, Montreal, Canada, 2019* (2019).

[111] J. Veraart, E. Fieremans, and D. S. Novikov, Diffusion MRI noise mapping using random matrix theory, *Magnetic Resonance in Medicine* **76**, 1582 (2016).

[112] H.-H. Lee, D. S. Novikov, and E. Fieremans, Removal of partial fourier-induced gibbs (rpg) ringing artifacts in MRI, *Magnetic Resonance in Medicine* **86**, 2733 (2021).

[113] S. M. Smith, M. Jenkinson, M. W. Woolrich, C. F Beckmann, T. E J Behrens, H. Johansen-Berg, P. Bannister, M. Luca, I. Drobniak, D. Flitney, R. Niazy, J. Saunders, J. Vickers, Y. Zhang, N. De Stefano, M. Brady, and P. Matthews, Advances in functional and structural mr image analysis and implementation as fsl, *NeuroImage* **23 Suppl 1**, S208 (2004).

[114] J. L. Andersson, S. Skare, and J. Ashburner, How to correct susceptibility distortions in spin-echo echo-planar images: application to diffusion tensor imaging, *NeuroImage* **20**, 870 (2003).

[115] N. Wiest-Daesslé, S. Prima, P. Coupé, S. P. Morrissey, and C. Barillot, Non-local means variants for denoising of diffusion-weighted and diffusion tensor MRI, in *Medical Image Computing and Computer-Assisted Intervention (MICCAI)*, Vol. 10 (Springer, 2007) pp. 344—351.

[116] J. Veraart, J. Sijbers, S. Sunaert, A. Leemans, and B. Jeurissen, Weighted linear least squares estimation of diffusion MRI parameters: Strengths, limitations, and pitfalls, *NeuroImage* **81**, 335 (2013).

[117] M. Herberthson, D. Boito, T. D. Haije, A. Feragen, C.-F. Westin, and E. Özarslan, Q-space trajectory imaging with positivity constraints (QTI+), *NeuroImage* **238**, 118198 (2021).

[118] Particle Data Group, Review of Particle Physics, *Progress of Theoretical and Experimental Physics* **2022**, 083C01 (2022).

[119] D. A. Varshalovich, A. N. Moskalev, and V. K. Khersonskii, *Quantum Theory of Angular Momentum* (1988).

ACKNOWLEDGMENTS

This work was performed under the rubric of the Center for Advanced Imaging Innovation and Research (CAI²R,

<https://www.cai2r.net>), an NIBIB Biomedical Technology Resource Center NIH P41-EB017183 (DN, EF). This work has been supported by NIH under NINDS R01 NS088040 (DN, EF) and NIBIB R01 EB027075 (DN, EF) and K99 EB036080 (SC) awards, as well as by the Swedish Research Council 2021-04844 (FS) and the Swedish Cancer Society 22 0592 JIA (FS). Authors are grateful to Sune Jespersen, Valerij Kiselev and Jelle Veraart for fruitful discussions.

AUTHOR CONTRIBUTIONS STATEMENT

SC and DSN developed theory and wrote the manuscript. SC performed data analysis. JC and EF curated, and JC pre-processed MRI data for multiple sclerosis classification. FS provided multidimensional dMRI sequence. SC, EF and DSN conceived and designed the study. EF and DSN supervised the project. All authors reviewed the manuscript and provided feedback.

COMPETING INTERESTS STATEMENT

SC, EF, DSN are co-inventors in technology related to this research; a PCT patent application has been filed and is pending. EF, DSN, and NYU School of Medicine are stock holders of Microstructure Imaging, Inc. — post-processing tools for advanced MRI methods. FS is an inventor of technology related to this research and has financial interest in related patents. The remaining authors declare no competing interests.

SUPPLEMENTARY INFORMATION

Santiago Coelho, Jenny Chen, Filip Szczepankiewicz, Els Fieremans, and Dmitry S. Novikov
 Corresponding authors: Santiago.Coelho@nyulangone.org (SC) and Dmitry.Novikov@nyulangone.org (DSN)

S1. IRREDUCIBLE DECOMPOSITION INTO A SUM OF TENSORS WITH THE SAME ORDER, EQS. (50)–(54)

To find all the spherical tensor components (55) of the decomposition (50) used in this work we need to project on the generalized basis (51). The normalization coefficients (53) can be found straightforwardly:

$$\begin{aligned} \mathcal{Y}_{ij}^{00} &= \delta_{ij}, \quad \zeta(2, 0) = \mathcal{Y}_{ij}^{00*} \mathcal{Y}_{ij}^{00} = \delta_{ij} \delta_{ij} = 3; \\ \mathcal{Y}_{ijkl}^{00} &= \delta_{(ij} \delta_{kl)}, \quad \zeta(4, 0) = \mathcal{Y}_{ijkl}^{00} \delta_{ij} \delta_{kl} = \frac{1}{3} (\delta_{ij} \delta_{kl} + \delta_{ik} \delta_{jl} + \delta_{il} \delta_{jk}) \delta_{ij} \delta_{kl} = \frac{1}{3} (3 \cdot 3 + 3 + 3) = 5; \\ \mathcal{Y}_{ijkl}^{2m} \delta_{kl} &= \mathcal{Y}_{(ij}^{2m} \delta_{kl)} \delta_{kl} = \frac{1}{6} (\mathcal{Y}_{ij}^{2m} \delta_{kl} + \mathcal{Y}_{il}^{2m} \delta_{jk} + \mathcal{Y}_{ik}^{2m} \delta_{lj} + \mathcal{Y}_{kl}^{2m} \delta_{ij} + \mathcal{Y}_{jk}^{2m} \delta_{il} + \mathcal{Y}_{lj}^{2m} \delta_{ik}) \delta_{kl} = \frac{7}{6} \mathcal{Y}_{ij}^{2m}; \\ \mathcal{Y}_{ijkl}^{2m*} \mathcal{Y}_{ijkl}^{2m'} &= \mathcal{Y}_{(ij}^{2m*} \delta_{kl)} \delta_{kl} \mathcal{Y}_{ij}^{2m'} = \frac{7}{6} \mathcal{Y}_{ij}^{2m*} \mathcal{Y}_{ij}^{2m'} = \frac{7}{6} \cdot \frac{3}{2} \delta_{mm'} \equiv \zeta(4, 2) \delta_{mm'}, \quad \zeta(4, 2) = \frac{7}{4}. \end{aligned} \quad (S1)$$

In the last equation we used the normalization $\zeta(\ell, \ell)$ (48) for $\ell = 2$.

For completeness, in the remainder of this Section we motivate a general normalization formula (53) for all L and ℓ . Equation (53) relies on the following identity to be derived below:

$$\mathcal{Y}_{i_1 \dots i_L}^{\ell m} \delta_{i_{L-1} i_L} = \frac{(L + \ell + 1)(L - \ell)}{L(L - 1)} \mathcal{Y}_{i_1 \dots i_{L-2}}^{\ell m} \quad \text{for } L \geq \ell + 2; \quad \text{and} \quad 0 \quad \text{for } L = \ell. \quad (S2)$$

Assuming Eq. (S2) holds, we apply it recursively

$$\mathcal{Y}_{i_1 \dots i_L}^{\ell m} \delta_{i_{\ell+1} i_{\ell+2}} \dots \delta_{i_{L-1} i_L} = \frac{(L + \ell + 1)(L + \ell - 1) \dots (2\ell + 3)(L - \ell)(L - \ell - 2) \dots 2}{L(L - 1)(L - 2) \dots (\ell + 1)} \mathcal{Y}_{i_1 \dots i_\ell}^{\ell m}. \quad (S3)$$

Combining Eqs. (S3) and (48) allows us to obtain Eq. (53):

$$\zeta(L, \ell) = \mathcal{Y}_{i_1 \dots i_L}^{\ell m*} \mathcal{Y}_{i_1 \dots i_\ell}^{\ell m} \delta_{i_{\ell+1} i_{\ell+2}} \dots \delta_{i_{L-1} i_L} = \frac{(L + \ell + 1)!!(L - \ell)!!}{L!(2\ell + 1)}. \quad (S3)$$

To derive Eq. (S2), consider as an example the case for $L = \ell + 2$:

$$\begin{aligned} \mathcal{Y}_{i_1 \dots i_L}^{\ell m} \delta_{i_{L-1} i_L} &= \mathcal{Y}_{(i_1 \dots i_\ell}^{\ell m} \delta_{i_{L-1} i_L)} \delta_{i_{L-1} i_L} \\ &= \frac{\ell! 2!}{(\ell + 2)!} \left(\mathcal{Y}_{i_1 \dots i_\ell}^{\ell m} \delta_{i_{L-1} i_L} + \mathcal{Y}_{i_{L-1} i_2 \dots i_\ell}^{\ell m} \delta_{i_1 i_L} + \mathcal{Y}_{i_1 i_{L-1} i_3 \dots i_\ell}^{\ell m} \delta_{i_2 i_L} + \dots + \mathcal{Y}_{i_1 \dots i_{\ell-1} i_{L-1}}^{\ell m} \delta_{i_\ell i_L} \right. \\ &\quad \left. + \mathcal{Y}_{i_L i_2 \dots i_\ell}^{\ell m} \delta_{i_{L-1} i_1} + \mathcal{Y}_{i_1 i_L i_3 \dots i_\ell}^{\ell m} \delta_{i_{L-1} i_2} + \dots + \mathcal{Y}_{i_1 \dots i_{\ell-1} i_L}^{\ell m} \delta_{i_{L-1} i_\ell} \right. \\ &\quad \left. + \mathcal{Y}_{i_{L-1} i_L i_3 \dots i_\ell}^{\ell m} \delta_{i_1 i_2} + \mathcal{Y}_{i_{L-1} i_2 i_L i_4 \dots i_\ell}^{\ell m} \delta_{i_1 i_3} + \dots + \mathcal{Y}_{i_1 \dots i_{\ell-2} i_{L-1} i_L}^{\ell m} \delta_{i_{\ell-1} i_\ell} \right) \delta_{i_{L-1} i_L} \\ &= \frac{\ell! 2!}{(\ell + 2)!} \left(3 \mathcal{Y}_{i_1 \dots i_\ell}^{\ell m} + 2\ell \mathcal{Y}_{i_1 \dots i_\ell}^{\ell m} + \binom{\ell}{2} \times 0 \right) = \frac{2(2\ell + 3)}{(\ell + 1)(\ell + 2)} \mathcal{Y}_{i_1 \dots i_\ell}^{\ell m}, \end{aligned} \quad (S4)$$

which can be generalized for arbitrary $L > \ell$ to derive Eq. (S2). The rationale behind the derivation in Eq. (S4) is that one must expand the symmetrized $\mathcal{Y}_{i_1 \dots i_L}^{\ell m}$ into a sum of all permutations of subindices where i_{L-1}, i_L are either part of $\mathcal{Y}_{i_1 \dots i_\ell}^{\ell m}$ or part of a product of $(L - \ell)/2$ Kronecker deltas (in this case, a single one). Then, we have to contract indices i_{L-1}, i_L on each term and add the contributions. Contracting any two indices of $\mathcal{Y}_{i_1 \dots i_\ell}^{\ell m}$ yields 0 due to STF property, while all combinations of contractions of the products of the Kronecker symbols can be computed using

$$\delta_{(i_1 i_2 \dots \delta_{i_{L-1} i_L})} \delta_{(i_{\ell+1} i_{\ell+2} \dots \delta_{i_{L-1} i_L})} = \frac{L + 1}{\ell + 1} \delta_{(i_1 i_2 \dots \delta_{i_{L-3} i_{L-2}})}. \quad (S5)$$

S2. IRREDUCIBLE DECOMPOSITION OF SPHERICAL TENSOR PRODUCTS

A. Addition of angular momenta, Wigner rotation matrices, Clebsch-Gordan coefficients and spherical harmonics

A d -dimensional unitary representation \mathcal{D} of $\text{SO}(3)$ maps each group element $\mathcal{R} \in \text{SO}(3)$ onto a $d \times d$ unitary matrix $\mathcal{D}(\mathcal{R})$ realizing the rotation \mathcal{R} . All irreducible representations $\mathcal{D}^\ell(\mathcal{R})$ of $\text{SO}(3)$ are labeled by non-negative integers $\ell = 0, 1, 2, \dots$ and

have dimensions $2\ell+1$.^{54,55} From the representation theory standpoint, the addition of angular momenta $\vec{\ell}_1$ and $\vec{\ell}_2$ corresponds to the tensor product of two irreducible representations \mathcal{D}^{ℓ_1} and \mathcal{D}^{ℓ_2} of $\text{SO}(3)$ with dimensions $2\ell_1+1$ and $2\ell_2+1$. This tensor product of dimension $(2\ell_1+1)(2\ell_2+1)$ is reducible, and splits into a sum of irreducible representations with $L = |\ell_1 - \ell_2|, \dots, \ell_1 + \ell_2$, each one entering exactly once^{54,55}:

$$\mathcal{D}^{\ell_1} \otimes \mathcal{D}^{\ell_2} = \bigoplus_{L=-|\ell_1-\ell_2|}^{\ell_1+\ell_2} \mathcal{D}^L. \quad (\text{S6})$$

The orthonormal basis elements

$$|LM\rangle = \sum_{m_1+m_2=M} |\ell_1 m_1 \ell_2 m_2\rangle \langle \ell_1 m_1 \ell_2 m_2 | LM \rangle, \quad M = -L \dots L \quad (\text{S7})$$

of each such irreducible representation labeled by L , are expanded in terms of the basis elements of $|\ell_1 m_1 \ell_2 m_2\rangle = |\ell_1 m_1\rangle \otimes |\ell_2 m_2\rangle$ of the tensor product, where $m_1 = -\ell_1 \dots \ell_1$, $m_2 = -\ell_2 \dots \ell_2$, and $\langle \ell_1 m_1 \ell_2 m_2 | LM \rangle$ are the Clebsch–Gordan coefficients. In this work, we use complex spherical harmonics and spherical tensors, with the Condon–Shortley phase convention^{53,105}, for which the Clebsch–Gordan coefficients are purely real. Taking the matrix elements of the tensor product (S6), we obtain

$$\mathcal{D}_{m_1 n_1}^{l_1}(\mathcal{R}) \mathcal{D}_{m_2 n_2}^{l_2}(\mathcal{R}) = \sum_{L,M,N} \langle \ell_1 m_1 \ell_2 m_2 | LM \rangle \langle \ell_1 n_1 \ell_2 n_2 | LN \rangle \mathcal{D}_{MN}^L(\mathcal{R}). \quad (\text{S8})$$

By the Peter–Weyl theorem, elements of all unitary *Wigner matrices* $\mathcal{D}_{mm'}^{\ell}(\mathcal{R})$ are dense in $\text{SO}(3)$ and form an orthogonal basis,

$$\int_{\text{SO}(3)} d\mathcal{R} \mathcal{D}_{mn}^{\ell}(\mathcal{R}) \mathcal{D}_{m'n'}^{\ell'*}(\mathcal{R}) = \frac{1}{2\ell+1} \delta_{\ell\ell'} \delta_{mm'} \delta_{nn'}, \quad \mathcal{D}_{mn}^{\ell}(\mathcal{R}^{-1}) = \mathcal{D}_{nm}^{\ell*}(\mathcal{R}), \quad (\text{S9})$$

under the normalized Haar measure $\int_{\text{SO}(3)} d\mathcal{R} = 1$ on the group manifold. Following Eq. (S8), the integral of the triple product

$$\int_{\text{SO}(3)} d\mathcal{R} \mathcal{D}_{m_1 n_1}^{l_1}(\mathcal{R}) \mathcal{D}_{m_2 n_2}^{l_2}(\mathcal{R}) \mathcal{D}_{MN}^{L*}(\mathcal{R}) = \frac{1}{2L+1} \langle \ell_1 m_1 \ell_2 m_2 | LM \rangle \langle \ell_1 n_1 \ell_2 n_2 | LN \rangle. \quad (\text{S10})$$

Spherical harmonics $Y^{\ell m}(\hat{\mathbf{n}})$ realize the $(2\ell+1)$ -dimensional representations of $\text{SO}(3)$, and transform *covariantly* (as basis elements) via the corresponding Wigner matrices $\mathcal{D}_{m'm}^{\ell}(\mathcal{R})$:

$$\mathcal{R} Y^{\ell m}(\hat{\mathbf{n}}) = Y^{\ell m}(\mathcal{R}^{-1} \hat{\mathbf{n}}) = \sum_{m'=-\ell}^{\ell} Y^{\ell m'}(\hat{\mathbf{n}}) \mathcal{D}_{m'm}^{\ell}(\mathcal{R}). \quad (\text{S11})$$

Importantly, $Y^{\ell m}(\hat{\mathbf{n}})$ can also be viewed as a subset of Wigner matrix elements defined on a 2-sphere \mathbb{S}^2 formed by the tips of all unit vectors $\hat{\mathbf{n}}$, and viewed as a coset space $\mathbb{S}^2 = \text{SO}(3)/\text{SO}(2)$ of the original 3-dimensional $\text{SO}(3)$ manifold $\mathbb{S}^3/\mathbb{Z}_2$ over the $\text{SO}(2)$ rotations around $\hat{\mathbf{z}}$. For that, consider rotating the North pole $\hat{\mathbf{z}}$ of \mathbb{S}^2 by an $\text{SO}(3)$ matrix $\mathcal{R}_{\hat{\mathbf{n}}}$ that turns $\hat{\mathbf{z}}$ into $\hat{\mathbf{n}} \equiv \mathcal{R}_{\hat{\mathbf{n}}} \hat{\mathbf{z}}$. There is in fact a 1-dimensional family of such matrices $\mathcal{R}_{\hat{\mathbf{n}}}$ that yield the same $\hat{\mathbf{n}} \in \mathbb{S}^2$, with the same polar and azimuthal Euler angles, and an arbitrary third Euler angle of the $\text{SO}(2)$ rotation leaving $\hat{\mathbf{z}}$ unchanged (in the standard ZYZ convention⁵⁴). Using Eq. (S11) and $Y^{\ell m}(\hat{\mathbf{z}}) = \delta^{\ell 0}$ in the Racah normalization (46), $Y^{\ell m}(\hat{\mathbf{n}})$ are the \mathcal{D} -matrix elements independent of the third Euler angle (and up to complex conjugation):

$$Y^{\ell m}(\hat{\mathbf{n}}) = Y^{\ell m}(\mathcal{R}_{\hat{\mathbf{n}}} \hat{\mathbf{z}}) = \sum_{m'=-\ell}^{\ell} Y^{\ell m'}(\hat{\mathbf{z}}) \mathcal{D}_{m'm}^{\ell}(\mathcal{R}_{\hat{\mathbf{n}}}^{-1}) = \mathcal{D}_{0m}^{\ell}(\mathcal{R}_{\hat{\mathbf{n}}}^{-1}) \equiv \mathcal{D}_{m0}^{\ell*}(\mathcal{R}_{\hat{\mathbf{n}}}). \quad (\text{S12})$$

Using Eq. (S12) in the product (S8) and taking the $\langle \ell_1 m_1 \ell_2 m_2 | \dots | \ell_1 0 \ell_2 0 \rangle$ matrix element yields

$$Y^{\ell_1 m_1}(\hat{\mathbf{n}}) Y^{\ell_2 m_2}(\hat{\mathbf{n}}) = \sum_{L,M} \langle \ell_1 0 \ell_2 0 | L 0 \rangle \langle \ell_1 m_1 \ell_2 m_2 | LM \rangle Y^{LM}(\hat{\mathbf{n}}), \quad (\text{S13})$$

equivalent to the well-known spherical harmonics identity in Racah normalization (assuming $\int_{\mathbb{S}^2} d\hat{\mathbf{n}} = \int d\Omega_{\hat{\mathbf{n}}} / 4\pi \equiv 1$)

$$\int_{\mathbb{S}^2} d\hat{\mathbf{n}} Y^{\ell_1 m_1}(\hat{\mathbf{n}}) Y^{\ell_2 m_2}(\hat{\mathbf{n}}) Y^{LM*}(\hat{\mathbf{n}}) = \frac{1}{2L+1} \langle \ell_1 0 \ell_2 0 | L 0 \rangle \langle \ell_1 m_1 \ell_2 m_2 | LM \rangle. \quad (\text{S14})$$

B. Derivation of Eq. (58)

The derivation will be based on the analog of Eq. (S14) for the basis STF tensors, with the orthogonality over the unit sphere substituted by taking full trace. For that, we make use of the fully symmetric product of Kronecker symbols $I_{i_1 \dots i_\ell}$ and Eq. (2.3) from Thorne⁵³:

$$I_{i_1 \dots i_\ell} \equiv \delta_{(i_1 i_2 \dots i_{\ell-1} i_\ell)} = (\ell + 1) \int_{\mathbb{S}^2} d\hat{\mathbf{n}} n_{i_1} \dots n_{i_\ell}, \quad d\hat{\mathbf{n}} \equiv \frac{d\Omega_{\hat{\mathbf{n}}}}{4\pi}. \quad (\text{S15})$$

A useful relation then comes from combining the orthogonality (46) of spherical harmonics, and Eq. (S15):

$$\mathcal{Y}_{i_1 \dots i_\ell}^{\ell m} \mathcal{Y}_{j_1 \dots j_{\ell'}}^{\ell' m'} I_{i_1 \dots i_\ell j_1 \dots j_{\ell'}} = \delta_{\ell \ell'} \delta_{mm'}, \quad (\text{S16})$$

which can be extended to a more general scenario applying Eq. (52):

$$\mathcal{Y}_{i_1 \dots i_L}^{\ell m} \mathcal{Y}_{j_1 \dots j_{L'}}^{\ell' m'} I_{i_1 \dots i_L j_1 \dots j_{L'}} = \frac{L + L' + 1}{2\ell + 1} \delta_{\ell \ell'} \delta_{mm'} \quad \text{for the case where } L \geq \ell, L' \geq \ell'. \quad (\text{S17})$$

Likewise, we now can rewrite Eq. (S14) by replacing the integrals over $n_{i_1} n_{i_2} \dots n_{i_k}$ with Eq. (S15):

$$\mathcal{Y}_{(i_1 \dots i_{\ell_1})}^{\ell_1 m_1} \mathcal{Y}_{(j_1 \dots j_{\ell_2})}^{\ell_2 m_2} \mathcal{Y}_{k_1 \dots k_{\ell_1 + \ell_2}}^{LM*} I_{i_1 \dots i_{\ell_1} j_1 \dots j_{\ell_2} k_1 \dots k_{\ell_1 + \ell_2}} = \frac{2\ell_1 + 2\ell_2 + 1}{2L + 1} \langle \ell_1 0 \ell_2 0 | L 0 \rangle \langle \ell_1 m_1 \ell_2 m_2 | LM \rangle. \quad (\text{S18})$$

The term $\mathcal{Y}_{(i_1 \dots i_{\ell_1})}^{\ell_1 m_1} \mathcal{Y}_{(j_1 \dots j_{\ell_2})}^{\ell_2 m_2}$ is a symmetric tensor of order $\ell_1 + \ell_2$. Thus, we can expand it as a linear combination of basis tensors $\mathcal{Y}_{i_1 \dots i_{\ell_1} j_1 \dots j_{\ell_2}}^{\ell' m'}$, Eq. (51), with degrees $\ell' = 0, 2, \dots, \ell_1 + \ell_2$. When computing the tensor products on the left side of Eq. (S18), only the basis term $\ell' = L$ of the expansion of $\mathcal{Y}_{(i_1 \dots i_{\ell_1})}^{\ell_1 m_1} \mathcal{Y}_{(j_1 \dots j_{\ell_2})}^{\ell_2 m_2}$ returns a nonzero value. If we call ξ the coefficient accompanying the $\ell' = L$ term of the expansion, then Eq. (S18) can be written as

$$\mathcal{Y}_{(i_1 \dots i_{\ell_1})}^{\ell_1 m_1} \mathcal{Y}_{(j_1 \dots j_{\ell_2})}^{\ell_2 m_2} \mathcal{Y}_{k_1 \dots k_{\ell_1 + \ell_2}}^{LM*} I_{i_1 \dots i_{\ell_1} j_1 \dots j_{\ell_2} k_1 \dots k_{\ell_1 + \ell_2}} = \xi \mathcal{Y}_{i_1 \dots i_{\ell_1} j_1 \dots j_{\ell_2}}^{LM} \mathcal{Y}_{k_1 \dots k_{\ell_1 + \ell_2}}^{LM*} I_{i_1 \dots i_{\ell_1} j_1 \dots j_{\ell_2} k_1 \dots k_{\ell_1 + \ell_2}}, \quad (\text{S19})$$

which combined with Eq. (S17) provides the value $\xi = \langle \ell_1 0 \ell_2 0 | L 0 \rangle \langle \ell_1 m_1 \ell_2 m_2 | LM \rangle$. Using Eq. (53), we can write the product

$$\mathcal{Y}_{(i_1 \dots i_{\ell_1})}^{\ell_1 m_1} \mathcal{Y}_{(j_1 \dots j_{\ell_2})}^{\ell_2 m_2} \mathcal{Y}_{i_1 \dots i_{\ell_1} j_1 \dots j_{\ell_2}}^{LM*} = \xi \cdot \zeta(\ell_1 + \ell_2, L) = \zeta(\ell_1 + \ell_2, L) \langle \ell_1 0 \ell_2 0 | L 0 \rangle \langle \ell_1 m_1 \ell_2 m_2 | LM \rangle, \quad \ell_1 + \ell_2 \geq L, \quad (\text{S20})$$

since only the basis term $\ell' = L$ of the expansion of $\mathcal{Y}_{(i_1 \dots i_{\ell_1})}^{\ell_1 m_1} \mathcal{Y}_{(j_1 \dots j_{\ell_2})}^{\ell_2 m_2}$ returns a nonzero value, and $\zeta(\ell_1 + \ell_2, L)$ is the projection of the basis tensor onto itself, Eq. (53). Substituting $\ell_1 = \ell_2 = 2$ in Eq. (S20) yields Eq. (58).

C. Relation between Q and T tensors and compartmental spherical tensor covariances

Clebsch–Gordan coefficients are sparse since only those satisfying $m_1 + m_2 = M$ are nonzero (19 out of 125 for $\ell_1 = \ell_2 = L = 2$ and 25 out of 225 for $\ell_1 = \ell_2 = 2, L = 4$). We can substitute these in Eq. (8b), or equivalently Eq. (59), and combine it with

Eq. (8a) to get the system:

$$\begin{aligned}
Q^{00} &= \langle\langle (D^{00})^2 \rangle\rangle, \\
Q^{2m} &= 2 \langle\langle D^{00} D^{2m} \rangle\rangle \quad \text{for } m = -2, -1, \dots, 2; \\
T^{00} &= \frac{1}{\sqrt{5}} \left(2 \frac{1}{\sqrt{5}} \langle\langle D^{2-2} D^{22} \rangle\rangle - 2 \frac{1}{\sqrt{5}} \langle\langle D^{2-1} D^{21} \rangle\rangle + \frac{1}{\sqrt{5}} \langle\langle (D^{20})^2 \rangle\rangle \right), \\
T^{2-2} &= -\sqrt{\frac{2}{7}} \left(2 \sqrt{\frac{2}{7}} \langle\langle D^{2-2} D^{20} \rangle\rangle - \sqrt{\frac{3}{7}} \langle\langle (D^{2-1})^2 \rangle\rangle \right), \\
T^{2-1} &= -\sqrt{\frac{2}{7}} \left(2 \sqrt{\frac{3}{7}} \langle\langle D^{2-2} D^{21} \rangle\rangle - 2 \sqrt{\frac{1}{14}} \langle\langle D^{2-1} D^{20} \rangle\rangle \right), \\
T^{20} &= -\sqrt{\frac{2}{7}} \left(2 \sqrt{\frac{2}{7}} \langle\langle D^{2-2} D^{22} \rangle\rangle + 2 \sqrt{\frac{1}{14}} \langle\langle D^{2-1} D^{21} \rangle\rangle - \sqrt{\frac{2}{7}} \langle\langle (D^{20})^2 \rangle\rangle \right), \\
T^{21} &= -\sqrt{\frac{2}{7}} \left(2 \sqrt{\frac{3}{7}} \langle\langle D^{2-1} D^{22} \rangle\rangle - 2 \sqrt{\frac{1}{14}} \langle\langle D^{20} D^{21} \rangle\rangle \right), \\
T^{22} &= -\sqrt{\frac{2}{7}} \left(2 \sqrt{\frac{2}{7}} \langle\langle D^{20} D^{22} \rangle\rangle - \sqrt{\frac{3}{7}} \langle\langle (D^{21})^2 \rangle\rangle \right), \\
T^{4-4} &= \sqrt{\frac{18}{35}} \langle\langle (D^{2-2})^2 \rangle\rangle, \\
T^{4-3} &= \sqrt{\frac{18}{35}} 2 \frac{1}{\sqrt{2}} \langle\langle D^{2-2} D^{2-1} \rangle\rangle, \\
T^{4-2} &= \sqrt{\frac{18}{35}} \left(2 \sqrt{\frac{3}{14}} \langle\langle D^{2-2} D^{20} \rangle\rangle + \sqrt{\frac{4}{7}} \langle\langle (D^{2-1})^2 \rangle\rangle \right), \\
T^{4-1} &= \sqrt{\frac{18}{35}} \left(2 \sqrt{\frac{1}{14}} \langle\langle D^{2-2} D^{21} \rangle\rangle + 2 \sqrt{\frac{3}{7}} \langle\langle D^{2-1} D^{20} \rangle\rangle \right), \\
T^{40} &= \sqrt{\frac{18}{35}} \left(2 \sqrt{\frac{1}{70}} \langle\langle D^{2-2} D^{22} \rangle\rangle + 2 \sqrt{\frac{8}{35}} \langle\langle D^{2-1} D^{21} \rangle\rangle + \sqrt{\frac{18}{35}} \langle\langle (D^{20})^2 \rangle\rangle \right), \\
T^{41} &= \sqrt{\frac{18}{35}} \left(2 \sqrt{\frac{1}{14}} \langle\langle D^{2-1} D^{22} \rangle\rangle + 2 \sqrt{\frac{3}{7}} \langle\langle D^{20} D^{21} \rangle\rangle \right), \\
T^{42} &= \sqrt{\frac{18}{35}} \left(2 \sqrt{\frac{3}{14}} \langle\langle D^{20} D^{22} \rangle\rangle + \sqrt{\frac{4}{7}} \langle\langle (D^{21})^2 \rangle\rangle \right), \\
T^{43} &= \sqrt{\frac{18}{35}} 2 \frac{1}{\sqrt{2}} \langle\langle D^{21} D^{22} \rangle\rangle, \\
T^{44} &= \sqrt{\frac{18}{35}} \langle\langle (D^{22})^2 \rangle\rangle,
\end{aligned} \tag{S21}$$

where Clebsch-Gordan coefficients are written explicitly for the reader (see page 737 in Ref.¹¹⁸ for a complete table). This shows how all covariances contribute to T and Q irreducible components. Solving for all the covariances gives

$$\begin{aligned}
\langle\langle (D^{00})^2 \rangle\rangle &= Q^{00}, & \langle\langle D^{00} D^{2m} \rangle\rangle &= \frac{1}{2} Q^{2m} \quad \text{for } m = -2, \dots, 2; \\
\langle\langle (D^{2-2})^2 \rangle\rangle &= \frac{\sqrt{70}}{6} T^{4-4}, & \langle\langle D^{2-2} D^{2-1} \rangle\rangle &= \frac{\sqrt{35}}{6} T^{4-3}, \\
\langle\langle D^{2-2} D^{20} \rangle\rangle &= \frac{\sqrt{15}}{6} T^{4-2} - T^{2-2}, & \langle\langle D^{2-2} D^{21} \rangle\rangle &= \frac{\sqrt{5}}{6} T^{4-1} - \frac{\sqrt{6}}{2} T^{2-1}, \\
\langle\langle D^{2-2} D^{22} \rangle\rangle &= \frac{1}{6} T^{40} - T^{20} + T^{00}, & \langle\langle (D^{2-1})^2 \rangle\rangle &= \frac{\sqrt{10}}{3} T^{4-2} + \frac{\sqrt{150}}{10} T^{2-2}, \\
\langle\langle D^{2-1} D^{20} \rangle\rangle &= \frac{\sqrt{30}}{6} T^{4-1} + \frac{1}{2} T^{2-1}, & \langle\langle D^{2-1} D^{21} \rangle\rangle &= \frac{2}{3} T^{40} - \frac{1}{2} T^{20} - T^{00}, \\
\langle\langle D^{2-1} D^{22} \rangle\rangle &= \frac{\sqrt{5}}{6} T^{41} - \frac{\sqrt{6}}{2} T^{21}, & \langle\langle (D^{20})^2 \rangle\rangle &= T^{40} + T^{20} + T^{00}, \\
\langle\langle D^{20} D^{21} \rangle\rangle &= \frac{\sqrt{30}}{6} T^{41} + \frac{1}{2} T^{21}, & \langle\langle D^{20} D^{22} \rangle\rangle &= \frac{\sqrt{15}}{6} T^{42} - T^{22}, \\
\langle\langle (D^{21})^2 \rangle\rangle &= \frac{\sqrt{10}}{3} T^{42} + \frac{\sqrt{150}}{10} T^{22}, & \langle\langle D^{21} D^{22} \rangle\rangle &= \frac{\sqrt{35}}{6} T^{43}, \\
\langle\langle (D^{22})^2 \rangle\rangle &= \frac{\sqrt{70}}{6} T^{44}.
\end{aligned} \tag{S22}$$

The sparsity of the QT decomposition is seen in all covariances depending on few T and Q elements. The simplicity of Eq. (S22) relies on the usage of the canonical, complex-valued spherical tensor basis. As the C tensor is real-valued, we can go back and forth from complex to real spherical tensor representations. Specifically, to obtain real spherical harmonics covariances $\langle\langle D^{\ell m} D^{\ell' m'} \rangle\rangle$, one can take $T^{\ell m}$ and $Q^{\ell m}$ in the complex spherical tensor basis, compute $\langle\langle D^{\ell m} D^{\ell' m'} \rangle\rangle$ using Eqs. (S22), and then convert the latter to the real spherical tensor basis, as spelled out in the following Supplementary Section S3.

S3. RELATIONS BETWEEN REAL AND COMPLEX SPHERICAL TENSORS/HARMONICS

Since C is real-valued one may want to work with the real spherical tensor basis and, thus, write the solution (S22) for it. This is cumbersome because in the real basis Eq. (58) includes multiple combinations of Clebsch-Gordan coefficients $\langle 2 \pm m_1 2 \pm m_2 | 2 \pm M \rangle$. An alternative is to compute complex-valued $\langle\langle D^{\ell m} D^{\ell' m'} \rangle\rangle$ using Eq. (S22) and then transform these to real-valued ones. This can be done using the relation between complex and real spherical basis tensors:

$$\mathcal{Y}_{\mathbb{C}}^{\ell m} = \begin{cases} \frac{1}{\sqrt{2}} (\mathcal{Y}_{\mathbb{R}}^{\ell-m} - i \mathcal{Y}_{\mathbb{R}}^{\ell m}) & \text{if } m < 0 \\ \mathcal{Y}_{\mathbb{R}}^{\ell 0} & \text{if } m = 0, \\ \frac{(-1)^m}{\sqrt{2}} (\mathcal{Y}_{\mathbb{R}}^{\ell m} + i \mathcal{Y}_{\mathbb{R}}^{\ell-m}) & \text{if } m > 0 \end{cases} \quad \mathcal{Y}_{\mathbb{R}}^{\ell m} = \begin{cases} (-1)^m \sqrt{2} \operatorname{Im}(\mathcal{Y}_{\mathbb{C}}^{\ell-m}) & \text{if } m < 0 \\ \mathcal{Y}_{\mathbb{C}}^{\ell 0} & \text{if } m = 0, \\ (-1)^m \sqrt{2} \operatorname{Re}(\mathcal{Y}_{\mathbb{C}}^{\ell m}) & \text{if } m > 0 \end{cases} \quad (\text{S23})$$

where $\mathcal{Y}_{\mathbb{C}}^{\ell m}$ and $\mathcal{Y}_{\mathbb{R}}^{\ell m}$ are the complex and real STF basis tensors (identical relations apply to the spherical harmonics basis). Note that, unlike the complex spherical tensors, the real spherical tensor basis (following conventions) does *not* include the Condon-Shortley phase. Since compartmental diffusion tensors D_{ij} are real-valued, we can map complex-valued $D^{\ell m}$ into real-valued ones using the following relations:

$$D_{\mathbb{R}}^{\ell m} = \begin{cases} (-1)^{m+1} \sqrt{2} \operatorname{Im}(D_{\mathbb{C}}^{\ell-m}) & \text{if } m < 0 \\ D_{\mathbb{C}}^{\ell 0} & \text{if } m = 0, \\ (-1)^m \sqrt{2} \operatorname{Re}(D_{\mathbb{C}}^{\ell m}) & \text{if } m > 0 \end{cases} \quad \text{and} \quad D_{\mathbb{C}}^{\ell m*} = (-1)^m D_{\mathbb{C}}^{\ell-m}, \quad (\text{S24})$$

where $D_{\mathbb{R}}^{\ell m}$ and $D_{\mathbb{C}}^{\ell m}$ are spherical tensor coefficients using either real or complex basis. Thus, the mapping $\langle\langle D_{\mathbb{C}}^{\ell m} D_{\mathbb{C}}^{\ell' m'} \rangle\rangle \rightarrow \langle\langle D_{\mathbb{R}}^{\ell m} D_{\mathbb{R}}^{\ell' m'} \rangle\rangle$ becomes:

$$\langle\langle D_{\mathbb{R}}^{\ell m} D_{\mathbb{R}}^{\ell' m'} \rangle\rangle = \begin{cases} \langle\langle D_{\mathbb{C}}^{00} D_{\mathbb{C}}^{00} \rangle\rangle & \text{if } \ell = 0, m = 0, \ell' = 0, m' = 0, \\ \sqrt{2} \operatorname{Im} (\langle\langle D_{\mathbb{C}}^{00} D_{\mathbb{C}}^{2m'} \rangle\rangle) & \text{if } \ell = 0, m = 0, \ell' = 2, m' < 0, \\ \langle\langle D_{\mathbb{C}}^{00} D_{\mathbb{C}}^{20} \rangle\rangle & \text{if } \ell = 0, m = 0, \ell' = 2, m' = 0, \\ (-1)^{m'} \sqrt{2} \operatorname{Re} (\langle\langle D_{\mathbb{C}}^{00} D_{\mathbb{C}}^{2m'} \rangle\rangle) & \text{if } \ell = 0, m = 0, \ell' = 2, m' > 0, \\ -\operatorname{Re} (\langle\langle D_{\mathbb{C}}^{2m} D_{\mathbb{C}}^{2m'} \rangle\rangle) + (-1)^{m'} \operatorname{Re} (\langle\langle D_{\mathbb{C}}^{2m} D_{\mathbb{C}}^{2-m'} \rangle\rangle) & \text{if } \ell = 2, m < 0, \ell' = 2, m' < 0, \\ \sqrt{2} \operatorname{Im} (\langle\langle D_{\mathbb{C}}^{2m} D_{\mathbb{C}}^{20} \rangle\rangle) & \text{if } \ell = 2, m < 0, \ell' = 2, m' = 0, \\ (-1)^{m'} \operatorname{Im} (\langle\langle D_{\mathbb{C}}^{2m} D_{\mathbb{C}}^{2m'} \rangle\rangle) + \operatorname{Im} (\langle\langle D_{\mathbb{C}}^{2m} D_{\mathbb{C}}^{2-m'} \rangle\rangle) & \text{if } \ell = 2, m < 0, \ell' = 2, m' > 0, \\ \langle\langle D_{\mathbb{C}}^{20} D_{\mathbb{C}}^{20} \rangle\rangle & \text{if } \ell = 2, m = 0, \ell' = 2, m' = 0, \\ (-1)^{m'} \sqrt{2} \operatorname{Re} (\langle\langle D_{\mathbb{C}}^{20} D_{\mathbb{C}}^{2m'} \rangle\rangle) & \text{if } \ell = 2, m = 0, \ell' = 2, m' > 0, \\ (-1)^{m+m'} \operatorname{Re} (\langle\langle D_{\mathbb{C}}^{2m} D_{\mathbb{C}}^{2m'} \rangle\rangle) + (-1)^m \operatorname{Re} (\langle\langle D_{\mathbb{C}}^{2m} D_{\mathbb{C}}^{2-m'} \rangle\rangle) & \text{if } \ell = 2, m > 0, \ell' = 2, m' > 0. \end{cases} \quad (\text{S25})$$

S4. SECOND-ORDER 6D REPRESENTATION FOR FULLY SYMMETRIC FOURTH-ORDER 3D TENSORS

$$\mathbf{S}_{6 \times 6}^{(4)} = \begin{pmatrix} \frac{\sqrt{35}}{8} \mathbf{S}^{44} - \frac{\sqrt{5}}{4} \mathbf{S}^{42} + \frac{3}{8} \mathbf{S}^{40} & -\frac{\sqrt{35}}{8} \mathbf{S}^{44} + \frac{1}{8} \mathbf{S}^{40} & \frac{\sqrt{5}}{4} \mathbf{S}^{42} - \frac{1}{2} \mathbf{S}^{40} & \frac{\sqrt{70}}{8} \mathbf{S}^{4-4} - \frac{\sqrt{10}}{8} \mathbf{S}^{4-2} & \frac{\sqrt{35}}{8} \mathbf{S}^{43} - \frac{3\sqrt{5}}{8} \mathbf{S}^{41} & \frac{\sqrt{35}}{8} \mathbf{S}^{4-3} - \frac{\sqrt{5}}{8} \mathbf{S}^{4-1} \\ -\frac{\sqrt{35}}{8} \mathbf{S}^{44} + \frac{1}{8} \mathbf{S}^{40} & \frac{\sqrt{35}}{8} \mathbf{S}^{44} + \frac{\sqrt{5}}{4} \mathbf{S}^{42} + \frac{3}{8} \mathbf{S}^{40} & -\frac{\sqrt{5}}{4} \mathbf{S}^{42} - \frac{1}{2} \mathbf{S}^{40} & -\frac{\sqrt{70}}{8} \mathbf{S}^{4-4} - \frac{\sqrt{10}}{8} \mathbf{S}^{4-2} & -\frac{\sqrt{35}}{8} \mathbf{S}^{43} - \frac{\sqrt{5}}{8} \mathbf{S}^{41} & -\frac{\sqrt{35}}{8} \mathbf{S}^{4-3} - \frac{3\sqrt{5}}{8} \mathbf{S}^{4-1} \\ \frac{\sqrt{5}}{4} \mathbf{S}^{42} - \frac{1}{2} \mathbf{S}^{40} & -\frac{\sqrt{5}}{4} \mathbf{S}^{42} - \frac{1}{2} \mathbf{S}^{40} & \mathbf{S}^{40} & \frac{\sqrt{10}}{4} \mathbf{S}^{4-2} & \frac{\sqrt{5}}{2} \mathbf{S}^{41} & \frac{\sqrt{5}}{2} \mathbf{S}^{4-1} \\ \frac{\sqrt{70}}{8} \mathbf{S}^{4-4} - \frac{\sqrt{10}}{8} \mathbf{S}^{4-2} & -\frac{\sqrt{70}}{8} \mathbf{S}^{4-4} - \frac{\sqrt{10}}{8} \mathbf{S}^{4-2} & \frac{\sqrt{10}}{4} \mathbf{S}^{4-2} & -\frac{\sqrt{35}}{4} \mathbf{S}^{44} + \frac{1}{4} \mathbf{S}^{40} & \frac{\sqrt{70}}{8} \mathbf{S}^{4-3} - \frac{\sqrt{10}}{8} \mathbf{S}^{4-1} & -\frac{\sqrt{70}}{8} \mathbf{S}^{43} - \frac{\sqrt{10}}{8} \mathbf{S}^{41} \\ \frac{\sqrt{35}}{8} \mathbf{S}^{43} - \frac{3\sqrt{5}}{8} \mathbf{S}^{41} & -\frac{\sqrt{35}}{8} \mathbf{S}^{43} - \frac{\sqrt{5}}{8} \mathbf{S}^{41} & \frac{\sqrt{5}}{2} \mathbf{S}^{41} & \frac{\sqrt{70}}{8} \mathbf{S}^{4-3} - \frac{\sqrt{10}}{8} \mathbf{S}^{4-1} & \frac{\sqrt{5}}{2} \mathbf{S}^{62} - \mathbf{S}^{40} & \frac{\sqrt{5}}{2} \mathbf{S}^{4-2} \\ \frac{\sqrt{35}}{8} \mathbf{S}^{4-3} - \frac{\sqrt{5}}{8} \mathbf{S}^{4-1} & -\frac{\sqrt{35}}{8} \mathbf{S}^{4-3} - \frac{3\sqrt{5}}{8} \mathbf{S}^{4-1} & \frac{\sqrt{5}}{2} \mathbf{S}^{4-1} & -\frac{\sqrt{70}}{8} \mathbf{S}^{43} - \frac{\sqrt{10}}{8} \mathbf{S}^{41} & \frac{\sqrt{5}}{2} \mathbf{S}^{4-2} & -\frac{\sqrt{5}}{2} \mathbf{S}^{42} - \mathbf{S}^{40} \end{pmatrix}. \quad (\text{S26})$$

Direct inspection of Eq. (S26) makes it evident that: (i) $\operatorname{tr} \mathbf{S}_{6 \times 6}^{(4)} = 0$; (ii) one of the eigenvalues is zero ($\lambda_{a_0} = 0$); and (iii) its associated eigenvector is $\hat{\mathbf{v}}^{(a_0)} = \frac{1}{\sqrt{3}} (1, 1, 1, 0, 0, 0)^t$.

55. MINIMAL SPHERICAL DESIGNS FOR $L = 2$ AND $L = 4$ WITH ANTIPODAL SYMMETRY

Spherical designs are sets of unit vectors that fulfill Eq. (34). One can check that for any degree-2 function $f^{(2)}(\hat{\mathbf{n}})$ with antipodal symmetry (i.e., involving $\ell = 0$ and $\ell = 2$ spherical harmonics), the 2-design

$$\{\hat{\mathbf{n}}^\alpha\} = \{\hat{\mathbf{e}}_1, \hat{\mathbf{e}}_2, \hat{\mathbf{e}}_3\} = \{(1, 0, 0), (0, 1, 0), (0, 0, 1)\}$$

yields

$$\begin{aligned} \frac{1}{3} \sum_{\alpha=1}^3 f^{(2)}(\hat{\mathbf{n}}^\alpha) &= \frac{1}{3} \sum_{\ell=0,2} \sum_{m=-\ell}^{\ell} f^{\ell m} \mathcal{Y}_{ij}^{\ell m} (n_i^1 n_j^1 + n_i^2 n_j^2 + n_i^3 n_j^3) = \frac{1}{3} \sum_{\ell=0,2} \sum_{m=-\ell}^{\ell} f^{\ell m} \mathcal{Y}_{ij}^{\ell m} (\hat{\mathbf{e}}_1^{\otimes 2} + \hat{\mathbf{e}}_2^{\otimes 2} + \hat{\mathbf{e}}_3^{\otimes 2})_{ij} \\ &= \frac{1}{3} \sum_{\ell=0,2} \sum_{m=-\ell}^{\ell} f^{\ell m} (\mathcal{Y}_{11}^{\ell m} + \mathcal{Y}_{22}^{\ell m} + \mathcal{Y}_{33}^{\ell m}) = \frac{1}{3} \sum_{\ell=0,2} \sum_{m=-\ell}^{\ell} f^{\ell m} \mathcal{Y}_{ij}^{\ell m} \delta_{ij} = f^{00}, \end{aligned}$$

fulfilling Eq. (34). Here we used $\mathcal{Y}_{ij}^{00} = \delta_{ij}$ that follows from Eq. (51).

Likewise, for any degree-4 function $f^{(4)}(\hat{\mathbf{n}})$ with antipodal symmetry (involving $\ell = 0, 2$ and 4 spherical harmonics), the 4-design

$$\begin{aligned} \{\hat{\mathbf{n}}^\alpha\} &= \frac{1}{\sqrt{1+\varphi^2}} \{\hat{\mathbf{e}}_1 + \varphi \hat{\mathbf{e}}_2, \hat{\mathbf{e}}_2 + \varphi \hat{\mathbf{e}}_3, \hat{\mathbf{e}}_3 + \varphi \hat{\mathbf{e}}_1, \hat{\mathbf{e}}_1 - \varphi \hat{\mathbf{e}}_2, \hat{\mathbf{e}}_2 - \varphi \hat{\mathbf{e}}_3, \hat{\mathbf{e}}_3 - \varphi \hat{\mathbf{e}}_1\} \\ &= \frac{1}{\sqrt{1+\varphi^2}} \{(1, \varphi, 0), (0, 1, \varphi), (\varphi, 0, 1), (1, -\varphi, 0), (0, 1, -\varphi), (-\varphi, 0, 1)\} \end{aligned}$$

where $\varphi = (1 + \sqrt{5})/2$, yields

$$\begin{aligned} \frac{1}{6} \sum_{\alpha=1}^6 f^{(4)}(\hat{\mathbf{n}}^\alpha) &= \frac{1}{6} \sum_{\ell,m} f^{\ell m} \mathcal{Y}_{ijkl}^{\ell m} (n_i^1 n_j^1 n_k^1 n_l^1 + n_i^2 n_j^2 n_k^2 n_l^2 + n_i^3 n_j^3 n_k^3 n_l^3 + n_i^4 n_j^4 n_k^4 n_l^4 + n_i^5 n_j^5 n_k^5 n_l^5 + n_i^6 n_j^6 n_k^6 n_l^6) \\ &= \frac{1}{6} \sum_{\ell,m} f^{\ell m} \mathcal{Y}_{ijkl}^{\ell m} \frac{1}{(1+\varphi^2)^2} \left((\hat{\mathbf{e}}_1 + \varphi \hat{\mathbf{e}}_2)^{\otimes 4} + (\hat{\mathbf{e}}_2 + \varphi \hat{\mathbf{e}}_3)^{\otimes 4} + \dots + (\hat{\mathbf{e}}_3 - \varphi \hat{\mathbf{e}}_1)^{\otimes 4} \right)_{ijkl} \\ &= \frac{1}{6} \sum_{\ell,m} f^{\ell m} \mathcal{Y}_{ijkl}^{\ell m} \frac{6\varphi^2}{(1+\varphi^2)^2} \left(\hat{\mathbf{e}}_1^{\otimes 4} + \hat{\mathbf{e}}_2^{\otimes 4} + \hat{\mathbf{e}}_3^{\otimes 4} + 2 \hat{\mathbf{e}}_1^{\otimes 2} \hat{\mathbf{e}}_2^{\otimes 2} + 2 \hat{\mathbf{e}}_2^{\otimes 2} \hat{\mathbf{e}}_3^{\otimes 2} + 2 \hat{\mathbf{e}}_3^{\otimes 2} \hat{\mathbf{e}}_1^{\otimes 2} \right)_{ijkl} \\ &= \frac{1}{6} \sum_{\ell,m} f^{\ell m} \frac{6}{5} \left(\mathcal{Y}_{1111}^{\ell m} + \mathcal{Y}_{2222}^{\ell m} + \mathcal{Y}_{3333}^{\ell m} + 2 (\mathcal{Y}_{1122}^{\ell m} + \mathcal{Y}_{1133}^{\ell m} + \mathcal{Y}_{2233}^{\ell m}) \right) \\ &= \frac{1}{5} \sum_{\ell,m} f^{\ell m} \mathcal{Y}_{ijkl}^{\ell m} \delta_{ij} \delta_{kl} = \frac{1}{5} \sum_{\ell,m} f^{\ell m} \mathcal{Y}_{ijkl}^{\ell m} \delta_{(ij} \delta_{kl)} = f^{00}, \end{aligned}$$

fulfilling Eq. (34). Here we used $\varphi^2 = 1 + \varphi$, $1 + \varphi^2 = \sqrt{5} \varphi$, $1 + \varphi^4 = 3\varphi^2$, as well as $\mathcal{Y}_{ijkl}^{00} = \delta_{(ij} \delta_{kl)}$ that follows from Eq. (51), with $\zeta(4, 0) = 5$ in Eq. (53), cf. Eqs. (S1).

S6. SA IRREDUCIBLE DECOMPOSITION: ALL ROTATIONAL INVARIANTS

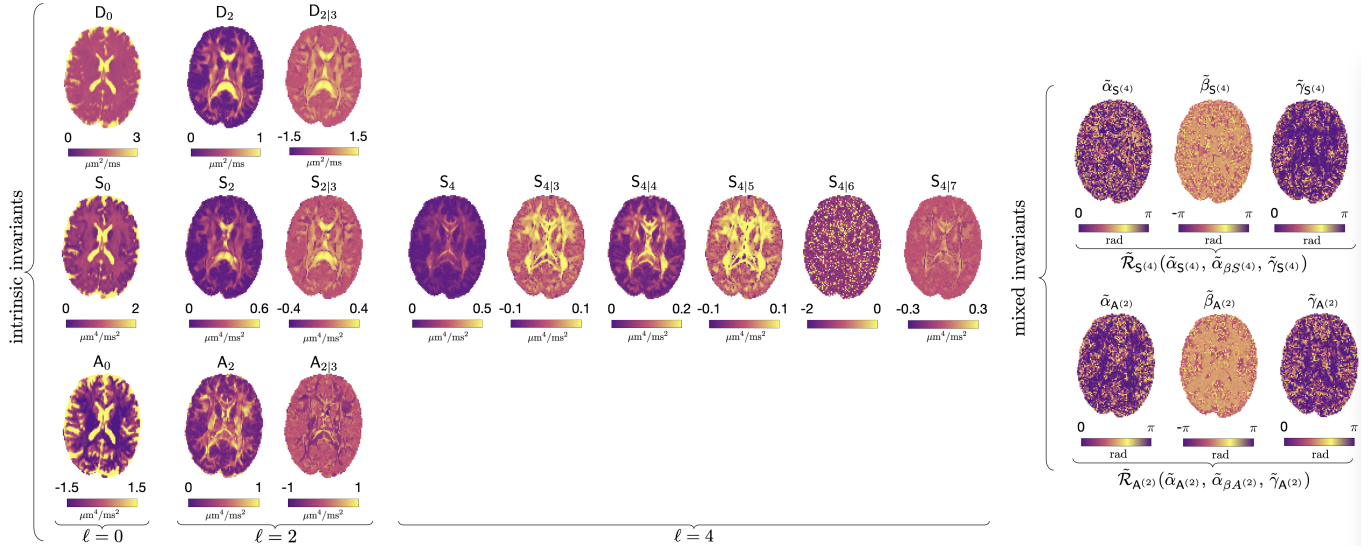


FIG. S1. RICE maps for a normal brain (33 y.o. male). Intrinsic invariants for each irreducible decomposition of D , S and A are shown as powers of corresponding traces, to match units of D and C tensors. Combinations of just 6 intrinsic invariants (out of $3 + 12$) generate all previously used model-independent dMRI contrasts, Eqs. (27)-(32). The 6 mixed invariants correspond to Euler angles of eigenframes of $S^{(4)}$ and $A^{(2)}$ relative to that of $S^{(2)}$ (see text). The underlying tissue microstructure introduces correlations between invariants. For example, small relative angles $\tilde{\beta}$ in white matter tracts exemplify the alignment of eigenframes of different representations of $SO(3)$ with the tract.

S7. MINIMAL PROTOCOLS VALIDATION WITH MAGNITUDE DENOISING PREPROCESSED DWI

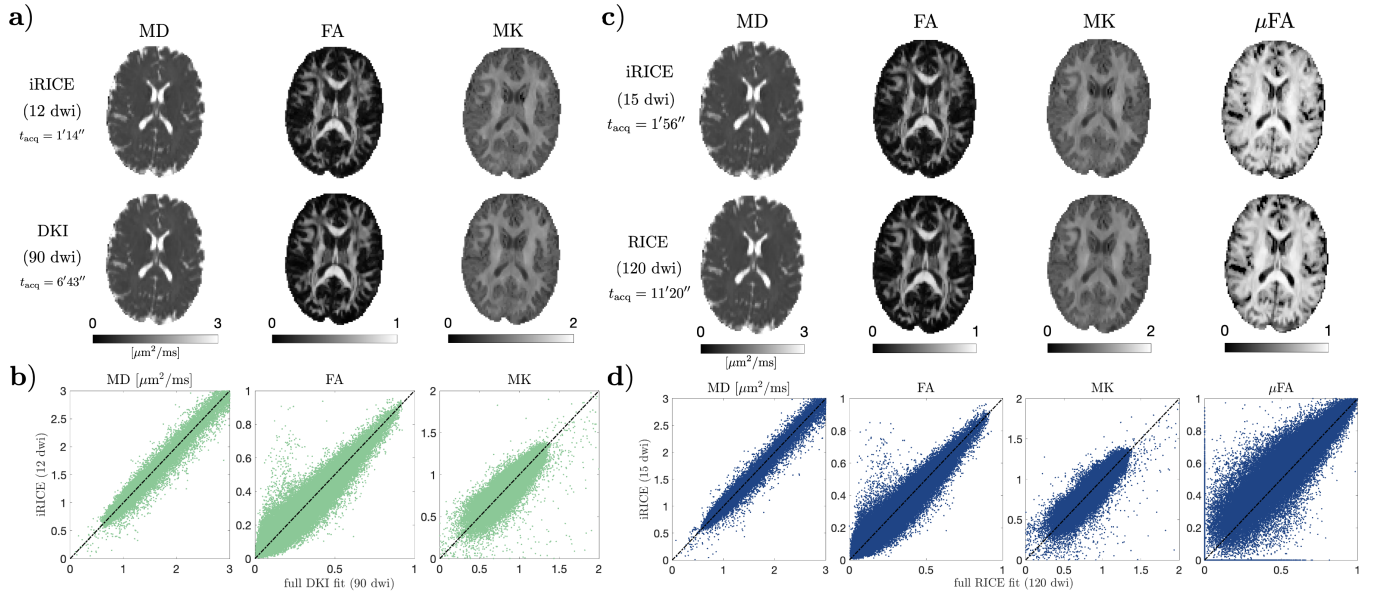


FIG. S2. Comparison of iRICE (1-2 minutes) with fully sampled acquisitions (6-11 minutes) for magnitude-denoised data. (a,c): iRICE maps (top) vs fully sampled DKI maps (bottom) for a healthy volunteer. Panels (b) and (d) show scatter plots for all brain voxels in a normal volunteer.

S8. DERIVATION OF TIME-DEPENDENT CUMULANTS (38) VIA DDE

Consider the logarithm $\mathcal{L}_{\text{DDE}}(\hat{\mathbf{g}}_1, \hat{\mathbf{g}}_2)$ of the DDE signal, that depends on the two unit gradient directions $\hat{\mathbf{g}}_1$ and $\hat{\mathbf{g}}_2$. A shell of DDE measurements (for a given set of scalar parameters, such as b -values and timings) is obtained by applying a sufficient number of $\text{SO}(3)$ rotations \mathcal{R} to a gradient pair $\hat{\mathbf{g}}_1$ and $\hat{\mathbf{g}}_2$, keeping angle $\psi = \arccos(\hat{\mathbf{g}}_1 \cdot \hat{\mathbf{g}}_2)$ between them fixed. On a shell, \mathcal{L}_{DDE} can be viewed as a scalar function $\mathcal{F}(\mathcal{R}) \equiv \mathcal{L}_{\text{DDE}}(\mathcal{R}\hat{\mathbf{g}}_1, \mathcal{R}\hat{\mathbf{g}}_2)$ on the $\text{SO}(3)$ group manifold $\mathbb{S}^3/\mathbb{Z}_2$, with the pair $\hat{\mathbf{g}}_1$ and $\hat{\mathbf{g}}_2$ setting the shell's “origin” (initial orientation).

The rationale behind Eq. (37) comes from the fact that for any function on a 2-dimensional sphere,

$$F(\hat{\mathbf{g}}) = \sum_{\ell=0}^{\infty} \sum_{m=-\ell}^{\ell} F^{\ell m} Y^{\ell m}(\hat{\mathbf{g}}), \quad \hat{\mathbf{g}} \in \mathbb{S}^2, \quad (\text{S27})$$

its spherical harmonics coefficients $F^{\ell m}$ can be found by lifting the integration from \mathbb{S}^2 to the $\text{SO}(3)$ manifold:

$$F^{\ell m} = (2\ell + 1) \int_{\mathbb{S}^2} d\hat{\mathbf{g}} Y^{\ell m*}(\hat{\mathbf{g}}) F(\hat{\mathbf{g}}) \equiv (2\ell + 1) \int_{\text{SO}(3)} d\mathcal{R} Y^{\ell m*}(\mathcal{R}\hat{\mathbf{g}}) F(\mathcal{R}\hat{\mathbf{g}}). \quad (\text{S28})$$

To prove, we expand $F(\mathcal{R}\hat{\mathbf{g}})$, use Eqs. (S9) and (S11), and Unsöld theorem $\sum_{m_1=-\ell}^{\ell} Y^{\ell m_1*}(\hat{\mathbf{g}}) Y^{\ell m_1}(\hat{\mathbf{g}}) \equiv 1$ [cf. Eq. (S38) below]:

$$(2\ell + 1) \int d\mathcal{R} Y^{\ell m*}(\mathcal{R}\hat{\mathbf{g}}) Y^{\ell m'}(\mathcal{R}\hat{\mathbf{g}}) = \sum_{m_1, m_2} Y^{\ell m_1*}(\hat{\mathbf{g}}) Y^{\ell m_2}(\hat{\mathbf{g}}) (2\ell + 1) \int d\mathcal{R} \mathcal{D}_{m_1 m}^{\ell*}(\mathcal{R}^{-1}) \mathcal{D}_{m_2 m'}^{\ell}(\mathcal{R}^{-1}) = \delta_{mm'}.$$

The spherical harmonics (38) can be derived directly by a projection (37) in the spirit of Eq. (S28), while averaging over all $\text{SO}(2)$ rotations of $\hat{\mathbf{g}}_2$ around every $\hat{\mathbf{g}}_1 \in \mathbb{S}^2$, exemplifying the Hopf mapping $\mathbb{S}^2 = \text{SO}(3)/\text{SO}(2)$.⁵⁸ Here, we find it instructive to come to the solution by remaining on the $\text{SO}(3)$ group manifold, developing the harmonic analysis there by employing the complete Fourier basis (S9) of Wigner matrices, and then “descending” onto \mathbb{S}^2 [cf. Eq. (S39) below].

For any $\mathcal{F}(\mathcal{R})$ on $\text{SO}(3)$, define the forward and inverse Fourier transforms as

$$\mathcal{F}(\mathcal{R}) = \sum_{\ell=0}^{\infty} \sum_{m, m'=-\ell}^{\ell} \mathcal{F}_{mm'}^{\ell} \mathcal{D}_{mm'}^{\ell*}(\mathcal{R}) \quad \Leftrightarrow \quad \mathcal{F}_{mm'}^{\ell} = (2\ell + 1) \int_{\text{SO}(3)} d\mathcal{R} \mathcal{D}_{mm'}^{\ell}(\mathcal{R}) \mathcal{F}(\mathcal{R}). \quad (\text{S29})$$

We adopt the convention that uses $\mathcal{D}_{mm'}^{\ell*}$ for the $\text{SO}(3)$ basis, and $\mathcal{D}_{mm'}^{\ell}$ for the forward transform, given the correspondence with the spherical harmonics expansion (S27) that involves the complex-conjugates (S12) of Wigner matrix elements. This convention is analogous to $e^{-i\omega t}$ for the temporal Fourier expansion on \mathbb{R} , and is opposite to the phase e^{+ikx} of the plane wave expansion.

Consider the forward $\text{SO}(3)$ Fourier transform, with the “shell origin” DDE pair $\hat{\mathbf{g}}_1$ and $\hat{\mathbf{g}}_2$ setting the “initial phase”:

$$\mathcal{L}_{\text{DDE}mm'}^{\ell} = (2\ell + 1) \int_{\text{SO}(3)} d\mathcal{R} \mathcal{D}_{mm'}^{\ell}(\mathcal{R}) \mathcal{L}_{\text{DDE}}(\mathcal{R}\hat{\mathbf{g}}_1, \mathcal{R}\hat{\mathbf{g}}_2). \quad (\text{S30})$$

The terms of Eq. (36) of the form (S27) involving a single $\hat{\mathbf{g}} = \hat{\mathbf{g}}_1$ or $\hat{\mathbf{g}}_2$, are straightforward: on a shell,

$$F(\mathcal{R}\hat{\mathbf{g}}) = \sum_{\ell, m} F^{\ell m} Y^{\ell m}(\mathcal{R}\hat{\mathbf{g}}) = \sum_{\ell, m, m'} F^{\ell m} Y^{\ell m'}(\hat{\mathbf{g}}) \mathcal{D}_{m' m}^{\ell}(\mathcal{R}^{-1}) = \sum_{\ell, m, m'} F^{\ell m} Y^{\ell m'}(\hat{\mathbf{g}}) \mathcal{D}_{mm'}^{\ell*}(\mathcal{R}) \Rightarrow F_{mm'}^{\ell} = F^{\ell m} Y^{\ell m'}(\hat{\mathbf{g}}), \quad (\text{S31})$$

where we used Eq. (S11) and Eq. (S29). Here and below the sums over m run between the corresponding $-\ell$ and ℓ .

The terms $\langle\langle D(\mathcal{R}\hat{\mathbf{g}}_1) D(\mathcal{R}\hat{\mathbf{g}}_2) \rangle\rangle = \sum \langle\langle D^{\ell_1 m_1} D^{\ell_2 m_2} \rangle\rangle Y^{\ell_1 m_1}(\mathcal{R}\hat{\mathbf{g}}_1) Y^{\ell_2 m_2}(\mathcal{R}\hat{\mathbf{g}}_2)$ depending on both DDE vectors involve

$$\begin{aligned} [Y^{\ell_1 m_1}(\mathcal{R}\hat{\mathbf{g}}_1) Y^{\ell_2 m_2}(\mathcal{R}\hat{\mathbf{g}}_2)]_{mm'}^{\ell} &= (2\ell + 1) \int_{\text{SO}(3)} d\mathcal{R} \mathcal{D}_{mm'}^{\ell}(\mathcal{R}) Y^{\ell_1 m_1}(\mathcal{R}\hat{\mathbf{g}}_1) Y^{\ell_2 m_2}(\mathcal{R}\hat{\mathbf{g}}_2) \\ &= (2\ell + 1) \int_{\text{SO}(3)} d\mathcal{R} \mathcal{D}_{mm'}^{\ell}(\mathcal{R}) \sum_{m'_1, m'_2} \mathcal{D}_{m'_1 m'_1}^{\ell_1}(\mathcal{R}^{-1}) \mathcal{D}_{m'_2 m'_2}^{\ell_2}(\mathcal{R}^{-1}) Y^{\ell_1 m'_1}(\hat{\mathbf{g}}_1) Y^{\ell_2 m'_2}(\hat{\mathbf{g}}_2) \\ &= (2\ell + 1) \int_{\text{SO}(3)} d\mathcal{R} \mathcal{D}_{mm'}^{\ell}(\mathcal{R}) \sum_{m'_1, m'_2} \mathcal{D}_{m'_1 m'_1}^{\ell_1*}(\mathcal{R}) \mathcal{D}_{m'_2 m'_2}^{\ell_2*}(\mathcal{R}) Y^{\ell_1 m'_1}(\hat{\mathbf{g}}_1) Y^{\ell_2 m'_2}(\hat{\mathbf{g}}_2) \\ &= \langle \ell_1 m_1 \ell_2 m_2 | \ell m \rangle \mathbb{Y}_{\ell_1 \ell_2}^{\ell m'}(\hat{\mathbf{g}}_1, \hat{\mathbf{g}}_2), \end{aligned} \quad (\text{S32})$$

where we used Eq. (S10) for a triple product of Wigner matrices and the fact that Clebsch-Gordan coefficients are real, and introduced the *bipolar spherical harmonics*¹¹⁹, the states with definite ℓ and m' that depend on two unit vectors:

$$\mathbb{Y}_{\ell_1 \ell_2}^{\ell m'}(\hat{\mathbf{g}}_1, \hat{\mathbf{g}}_2) \equiv \sum_{m'_1 + m'_2 = m'} \langle \ell_1 m'_1 \ell_2 m'_2 | \ell m' \rangle Y^{\ell_1 m'_1}(\hat{\mathbf{g}}_1) Y^{\ell_2 m'_2}(\hat{\mathbf{g}}_2). \quad (\text{S33})$$

Note that for the coinciding arguments $\hat{\mathbf{g}}_2 = \hat{\mathbf{g}}_1$, using Eq. (S13),

$$\mathbb{Y}_{\ell_1 \ell_2}^{\ell m'}(\hat{\mathbf{g}}, \hat{\mathbf{g}}) = \sum_{L, M} \langle \ell_1 0 \ell_2 0 | L 0 \rangle \sum_{m'_1, m'_2} \langle \ell_1 m'_1 \ell_2 m'_2 | \ell m' \rangle \langle \ell_1 m'_1 \ell_2 m'_2 | L M \rangle Y^{L M}(\hat{\mathbf{g}}) = \langle \ell_1 0 \ell_2 0 | \ell 0 \rangle Y^{\ell m'}(\hat{\mathbf{g}})$$

since the sum over m'_1, m'_2 spans all orthogonal states, yielding $\sum_{m'_1, m'_2} \langle \ell_1 m'_1 \ell_2 m'_2 | \ell m' \rangle \langle \ell_1 m'_1 \ell_2 m'_2 | L M \rangle = \delta_{L \ell} \delta_{M m'}$. Therefore, Eq. (S32) for the coinciding arguments equals

$$[Y^{\ell_1 m_1}(\mathcal{R}\hat{\mathbf{g}}) Y^{\ell_2 m_2}(\mathcal{R}\hat{\mathbf{g}})]_{mm'}^{\ell} = \langle \ell_1 0 \ell_2 0 | \ell 0 \rangle \langle \ell_1 m_1 \ell_2 m_2 | \ell m \rangle Y^{\ell m'}(\hat{\mathbf{g}}). \quad (\text{S34})$$

We can now use Eqs. (S31)–(S34) to compute the Wigner coefficients (S30):

$$\begin{aligned} \mathcal{L}_{\text{DDE}mm'}^{\ell} &= -b_1 \mathsf{D}^{\ell m}(t) Y^{\ell m'}(\hat{\mathbf{g}}_1) - b_2 \mathsf{D}^{\ell m}(t) Y^{\ell m'}(\hat{\mathbf{g}}_2) + \frac{1}{2} b_1^2 \mathsf{S}_{\mu}^{\ell m}(t) Y^{\ell m'}(\hat{\mathbf{g}}_1) + \frac{1}{2} b_2^2 \mathsf{S}_{\mu}^{\ell m}(t) Y^{\ell m'}(\hat{\mathbf{g}}_2) \\ &+ \frac{1}{2} \sum_{\ell_1, \ell_2, m_1, m_2} \langle\langle D^{\ell_1 m_1}(t) D^{\ell_2 m_2}(t) \rangle\rangle \langle \ell_1 m_1 \ell_2 m_2 | \ell m \rangle \left[\langle \ell_1 0 \ell_2 0 | \ell 0 \rangle \left(b_1^2 Y^{\ell m'}(\hat{\mathbf{g}}_1) + b_2^2 Y^{\ell m'}(\hat{\mathbf{g}}_2) \right) + 2b_1 b_2 \mathbb{Y}_{\ell_1 \ell_2}^{\ell m'}(\hat{\mathbf{g}}_1, \hat{\mathbf{g}}_2) \right]. \end{aligned} \quad (\text{S35})$$

Generalizing the QT-decomposition (8) onto t -dependent $\langle\langle D^{\ell_1 m_1}(t) D^{\ell_2 m_2}(t) \rangle\rangle$, Eq. (S35) yields the SO(3) Fourier components:

$$\begin{aligned} \mathcal{L}_{\text{DDE}000}^0 &= -(b_1 + b_2) \mathsf{D}^{00}(t) + \frac{1}{2} (b_1 + b_2)^2 \mathsf{Q}^{00}(t) + \frac{1}{2} (b_1^2 + b_2^2 + 2p_2 b_1 b_2) \mathsf{T}^{00}(t) + \frac{1}{2} (b_1^2 + b_2^2) \mathsf{S}_{\mu}^{00}(t), \\ \mathcal{L}_{\text{DDE}mm'}^2 &= -\mathsf{D}^{2m}(t) \left(b_1 Y^{2m'}(\hat{\mathbf{g}}_1) + b_2 Y^{2m'}(\hat{\mathbf{g}}_2) \right) + \frac{1}{2} \mathsf{Q}^{2m}(t) \left[b_1^2 Y^{2m'}(\hat{\mathbf{g}}_1) + b_2^2 Y^{2m'}(\hat{\mathbf{g}}_2) + b_1 b_2 \left(Y^{2m'}(\hat{\mathbf{g}}_1) + Y^{2m'}(\hat{\mathbf{g}}_2) \right) \right] \\ &+ \frac{1}{2} \mathsf{T}^{2m}(t) \left(b_1^2 Y^{2m'}(\hat{\mathbf{g}}_1) + b_2^2 Y^{2m'}(\hat{\mathbf{g}}_2) + 2b_1 b_2 \frac{\mathbb{Y}_{22}^{2m'}(\hat{\mathbf{g}}_1, \hat{\mathbf{g}}_2)}{\langle 2020 | 20 \rangle} \right) + \frac{1}{2} \mathsf{S}_{\mu}^{2m}(t) \left(b_1^2 Y^{2m'}(\hat{\mathbf{g}}_1) + b_2^2 Y^{2m'}(\hat{\mathbf{g}}_2) \right), \\ \mathcal{L}_{\text{DDE}mm'}^4 &= \frac{1}{2} \mathsf{T}^{4m}(t) \left(b_1^2 Y^{4m'}(\hat{\mathbf{g}}_1) + b_2^2 Y^{4m'}(\hat{\mathbf{g}}_2) + 2b_1 b_2 \frac{\mathbb{Y}_{22}^{4m'}(\hat{\mathbf{g}}_1, \hat{\mathbf{g}}_2)}{\langle 2020 | 40 \rangle} \right) + \frac{1}{2} \mathsf{S}_{\mu}^{4m}(t) \left(b_1^2 Y^{4m'}(\hat{\mathbf{g}}_1) + b_2^2 Y^{4m'}(\hat{\mathbf{g}}_2) \right). \end{aligned} \quad (\text{S36})$$

Here, for $\ell = 0$, we used $\mathbb{Y}_{00}^{00}(\hat{\mathbf{g}}_1, \hat{\mathbf{g}}_2) = \langle 0000 | 00 \rangle = 1$, as well as (setting $\ell' = 2$ in the $\sim b_1 b_2$ term)

$$\mathbb{Y}_{\ell' \ell'}^{00}(\hat{\mathbf{g}}_1, \hat{\mathbf{g}}_2) = \sum_m \langle \ell' m \ell'(-m) | 00 \rangle Y^{\ell' m}(\hat{\mathbf{g}}_1) Y^{\ell', -m}(\hat{\mathbf{g}}_2) = \langle \ell' 0 \ell' 0 | 00 \rangle \sum_m (-1)^m Y^{\ell' m}(\hat{\mathbf{g}}_1) Y^{\ell', -m}(\hat{\mathbf{g}}_2) = \langle \ell' 0 \ell' 0 | 00 \rangle p_{\ell'}, \quad (\text{S37})$$

coming from $\langle \ell m \ell(-m) | 00 \rangle = (-1)^m \langle \ell 0 \ell 0 | 00 \rangle$, cf. Ref.¹¹⁹, Eqs. (47) and (60), and the *addition theorem* in Racah normalization:

$$\sum_m Y^{\ell m *}(\hat{\mathbf{g}}_1) Y^{\ell m}(\hat{\mathbf{g}}_2) = P_{\ell}(\hat{\mathbf{g}}_1 \cdot \hat{\mathbf{g}}_2) \equiv p_{\ell}(\psi). \quad (\text{S38})$$

For $\ell = 2$, in the $\mathsf{Q}^{2m}(t)$ part we used $\mathbb{Y}_{\ell 0}^{\ell m'}(\hat{\mathbf{g}}_1, \hat{\mathbf{g}}_2) = Y^{\ell m'}(\hat{\mathbf{g}}_1)$ and $\mathbb{Y}_{0 \ell}^{\ell m'}(\hat{\mathbf{g}}_1, \hat{\mathbf{g}}_2) = Y^{\ell m'}(\hat{\mathbf{g}}_2)$.

The SO(3) Fourier coefficients (S36) are general yet *redundant*. All tensor components are contained in harmonics (38) on \mathbb{S}^2 :

$$\mathcal{L}_{\text{DDE}}^{\ell m}(\hat{\mathbf{g}}_1, \hat{\mathbf{g}}_2) = (2\ell + 1) \int_{\text{SO}(3)} d\mathcal{R} Y^{\ell m *}(\mathcal{R}\hat{\mathbf{g}}_1) \sum_{m_1, m_2} \mathcal{L}_{\text{DDE}m_1 m_2}^{\ell} \mathcal{D}_{m_1 m_2}^{\ell *}(\mathcal{R}) = \sum_{m'} \mathcal{L}_{\text{DDE}mm'}^{\ell}(\hat{\mathbf{g}}_1, \hat{\mathbf{g}}_2) Y^{\ell m' *}(\hat{\mathbf{g}}_1), \quad (\text{S39})$$

where we rotated $Y^{\ell m *}(\mathcal{R}\hat{\mathbf{g}}_1) = \sum_{m'} Y^{\ell m' *}(\hat{\mathbf{g}}_1) \mathcal{D}_{mm'}^{\ell}(\mathcal{R})$ via Eq. (S11) and used the unitarity of \mathcal{D} . The sums in (S39) with single $Y^{\ell m'}$ in Eq. (S36) are evaluated via the addition theorem (S38). The sums involving bipolar harmonics can be found by noting that both $Y^{\ell m'}(\hat{\mathbf{g}}_1)$ and $\mathbb{Y}_{\ell_1 \ell_2}^{\ell m'}(\hat{\mathbf{g}}_1, \hat{\mathbf{g}}_2)$ transform according to the same ℓ -irreducible representation of SO(3)¹¹⁹. Hence, their contraction (S39) is a Hermitian inner product in the unitary representation space, invariant under global rotations \mathcal{R} . Thus, $\sum_{m'} \mathbb{Y}_{\ell_1 \ell_2}^{\ell m'}(\mathcal{R}\hat{\mathbf{g}}_1, \mathcal{R}\hat{\mathbf{g}}_2) Y^{\ell m' *}(\mathcal{R}\hat{\mathbf{g}}_1) = \sum_{m'} \mathbb{Y}_{\ell_1 \ell_2}^{\ell m'}(\hat{\mathbf{g}}_1, \hat{\mathbf{g}}_2) Y^{\ell m' *}(\hat{\mathbf{g}}_1)$ is independent of the global rotation \mathcal{R} . Therefore, we select the frame where $\hat{\mathbf{g}}_1 = \hat{\mathbf{z}}$ and $\hat{\mathbf{g}}_2 = \mathcal{R}_{21}(\psi) \hat{\mathbf{z}}$, such that $Y^{\ell m'}(\hat{\mathbf{g}}_1) = \delta_{m' 0}, Y^{\ell 0}(\hat{\mathbf{g}}_2) = p_{\ell},$ and the only relevant bipolar harmonics

$$\sum_{m'} \mathbb{Y}_{\ell_1 \ell_2}^{\ell m'}(\hat{\mathbf{g}}_1, \hat{\mathbf{g}}_2) Y^{\ell m' *}(\hat{\mathbf{g}}_1) = \mathbb{Y}_{\ell_1 \ell_2}^{L0}(\hat{\mathbf{g}}_1, \hat{\mathbf{g}}_2) = \sum_m \langle \ell_1 m \ell_2(-m) | L 0 \rangle \delta_{m 0} Y^{\ell_2, -m}(\hat{\mathbf{g}}_2) = \langle \ell_1 0 \ell_2 0 | L 0 \rangle Y^{\ell_2 0}(\hat{\mathbf{g}}_2) = \langle \ell_1 0 \ell_2 0 | L 0 \rangle p_{\ell_2}(\psi). \quad (\text{S40})$$

In other words, the result of summation (S39) is equivalent to $\mathcal{L}_{\text{DDE}}^{\ell m} = \mathcal{L}_{\text{DDE}m 0}^{\ell}$ when $\hat{\mathbf{g}}_1 = \hat{\mathbf{z}}$, which yields Eq. (38). Alternatively, Eq. (S40) can be derived introducing an auxiliary rotation \mathcal{R}_1 , such that $\hat{\mathbf{g}}_1 = \mathcal{R}_1 \hat{\mathbf{z}}$, without fixing a particular reference frame. Using Eqs. (S11)–(S12), the product YY can be reduced to $YY \rightarrow \mathcal{D}\mathcal{D} \rightarrow \mathcal{D}$. For brevity, this derivation is omitted.